

Tagging ultra-boosted jets at FCC-hh using machine learning techniques

Biplob Bhattacharjee,^a Sanchari Bhattacharyya,^a Camellia Bose,^a Debtosh Chowdhury,^b Swagata Mukherjee^b

^a*Centre for High Energy Physics, Indian Institute of Science, Bangalore 560012, India*

^b*Department of Physics, Indian Institute of Technology, Kanpur 208016, India*

E-mail: biplob@iisc.ac.in, sancharibhat@iisc.ac.in,
camelliabose@iisc.ac.in, debtoshc@iitk.ac.in, swagata@iitk.ac.in

ABSTRACT: The Future Circular Hadron Collider (FCC-hh) will probe unprecedented energy regimes, enabling direct searches for new elementary particles at a scale of tens of TeV. FCC-hh is currently in the planning stage, and one of its primary physics goals is to search for physics beyond the Standard Model by exploring a previously inaccessible kinematic domain. While venturing into uncharted high-energy territories promises excitement, reconstructing objects with enormous transverse momenta will require overcoming major experimental challenges. This work investigates the identification of boosted W bosons and boosted top quarks in the context of three beyond the Standard Model scenarios: heavy vector-like quark (B'), heavy neutral gauge boson (Z'), and heavy neutral Higgs boson (H). We employ machine learning techniques, including eXtreme Gradient Boosting (XGBoost) and convolutional neural networks (CNN), to identify these ultra-boosted objects in the collider from their SM background counterpart. We evaluate the performance of these techniques in distinguishing W jets and top jets from QCD jets at extremely high transverse momenta (p_T) values, demonstrating their potential for future FCC-hh analyses.

Contents

1	Introduction	1
2	Theoretical Scenarios	4
3	CERN FCC facility	8
4	Simulation of events	9
5	Challenges and mitigation strategies for jets at $\sqrt{s} = 100$ TeV	11
5.1	Migration of jet transverse momentum	12
5.2	Effect of fixed jet radius on top and QCD jet mass	13
5.2.1	Jet radius estimation at the parton level	14
5.3	Effects of finite detector resolution on top and QCD jet mass	16
5.3.1	Calorimeters	16
5.3.2	Tracking system	19
5.4	Effects of finite detector resolution on N-Subjettiness observables	19
5.5	Boosted W jets at $\sqrt{s} = 100$ TeV	22
5.6	Jet grooming techniques	24
6	Machine learning techniques for jet tagging	25
6.1	Extreme Gradient Boosted Decision Trees	26
6.2	Convolutional Neural Networks (CNN)	28
6.2.1	Pre-processing of the images	29
6.2.2	The network architecture and results	29
7	Analysis of BSM processes with top and W jets in the final state	33
7.1	Analysis of Z' boson decaying to boosted top jets	33
7.1.1	Effect of b tagging	36
7.2	Analysis of neutral heavy Higgs boson decaying to boosted W jets	37

7.3	Analysis of vector-like, heavy B' quark decaying to boosted top jet and W jet	41
8	Conclusion	44
9	Acknowledgments	46
Appendix A Jet after soft drop		46

1 Introduction

Experiments at the Large Hadron Collider (LHC) have contributed significantly to our understanding of the Standard Model (SM) of particle physics, including the discovery of the Higgs boson and precision measurements of its properties [1–7]. While the SM has been rigorously tested with great precision, unanswered puzzles remain, such as the hierarchy problem, the observed phenomena of dark matter, neutrino masses, and matter-antimatter asymmetry in the universe. Although these gaps in our understanding of the universe suggest the existence of Beyond the Standard Model (BSM) physics, there is no consensus about the typical scale at which the new physics should appear.

The lack of conclusive evidence for new physics at the LHC suggests that BSM phenomena may occur at energy scales inaccessible to current collider experiments. Various BSM scenarios predict new particles with large masses. For example, a simple $U(1)$ extension of the SM in the gauge sector predicts the existence of a new gauge boson Z' [8–10]. Similarly, BSM extensions of the Higgs sector in theories such as the Two Higgs Doublet Model [11–18] contain charged and neutral heavy Higgs bosons. Future collider initiatives are essential for exploring such BSM phenomena at energy scales beyond the LHC’s capabilities. The production of such heavy BSM particles at future colliders results in highly energetic and heavily boosted decay products, complicating event reconstruction and object identification. This study focuses on efficiently identifying these heavy states, common to many prominent BSM physics models, at the FCC-hh collider.

The FCC-hh [19, 20] program at CERN, Geneva, boasts an exceptionally broad physics program, spanning Standard Model precision studies to direct searches for BSM. It will explore uncharted territories in high-energy physics, enabling searches for new physics at unprecedented mass scales. However, this endeavor also poses unique challenges in object reconstruction, particularly for objects with extremely large transverse momenta (p_T) [21–23].

High-energy particle colliders rely on sophisticated detectors to measure the signatures of particles produced in collisions. A typical detector consists of multiple concentric layers. The innermost layer usually consists of a tracking detector, which tracks the trajectories of charged particles in the presence of a strong magnetic field. Surrounding this is the calorimeter, which is divided into electromagnetic and hadronic components to measure the energy of electrons, photons, and hadrons. The outermost layer contains the muon detector, designed to identify and measure the momentum of muons, which penetrate through the calorimeter. In the case of FCC-hh, the large p_T of objects resulting from the decay of a highly massive particle leads to highly collimated decay products. Accurate reconstruction of these events depends on high-resolution detectors to resolve the individual signatures within these ultra-boosted objects [24].

In BSM physics analyses featuring final states that contain the W boson or the top quark, high selection efficiencies can generally be attained by leveraging hadronic decay channels. At sufficiently large Lorentz boost (typically $p_T > 200$ GeV or so), the final-state hadrons from the decay of W bosons or top quarks merge into a single large-radius (i.e., fat) jet. In such cases, jet substructure techniques are normally used to identify the jets arising from decays of W bosons or top quarks, exploiting the multiple, experimentally separable subjets within the fat jet [25–30]. However, in FCC-hh, where p_T of top quark or W boson can be in the multi-TeV range, the subjets will overlap and may not be experimentally separable anymore. Then, a key question that arises is how robust or useful the jet substructure observables (like N-Subjettiness) will remain at such high energy scales. The highly collimated nature of jets at FCC-hh will make it very challenging to identify their subjet information in the same way as it is still possible at the LHC. The proposed solution in this direction has been to use observables constructed on track jets, as the tracking devices have the best resolution, much better than the calorimeters. Track-based observables offer improved discrimination properties of jet substructure variables compared to calorimeter-based methods, owing to the better resolution of the tracking system at FCC-hh [21, 22]. In this context, we have studied the robustness of the improved discriminating power under various conditions of energy resolution of calorimeters as well as the granularity of calorimeters and trackers. Moreover, previous studies have highlighted the importance of choosing an optimum jet radius to avoid contamination from excess radiation [21]. In this work, we focus on optimizing the jet radius from parton-level information of the top quark and W boson decay.

Furthermore, the performance of jet tagging at the LHC has steadily been improving and heavily relies on various Machine Learning (ML) techniques [31–83], which also inspires jet tagging algorithms for the proposed FCC-hh detectors. The focus of this work is mainly on the identification of boosted top jets and W jets in FCC-hh detectors using modern ML techniques such as Extreme Gradient Boosting (XGBoost) [84] and convolutional neural networks (CNN)

[85–87]. We investigate the feasibility of efficiently distinguishing multi-prong W jets and top quark jets from single-prong QCD jets, where these objects have extremely high p_T , far exceeding those encountered at the LHC. The models are trained as multi-class classifiers. We use the score from the classifiers to tag the final state top and W jets, thus allowing us to reconstruct the massive BSM particle. The study is based on the fast simulation of the reference FCC-hh detector.

Earlier works have studied the discovery potential of the FCC-hh for heavy resonances using Boosted Decision Trees (BDTs) [88, 89]. In our study, we explore the variation of jet kinematics with p_T and make use of the information to build jet identification strategies spanning a broad range of transverse momenta. The reason is that any heavy resonance decays to jets with p_T ranging from, say, $\mathcal{O}(1)$ TeV to as high as half of its mass. The capability of FCC-hh to directly produce such heavy resonances necessitates the development of p_T -specific taggers, as demonstrated in our study. We perform the detailed analysis of three benchmark BSM scenarios: a high-mass Z' boson decaying to boosted top jets, a heavy neutral CP-even Higgs boson decaying to boosted W jets, and a high-mass vector-like quark (B') decaying to boosted top quark jet and boosted W jet.

This paper explores the feasibility of efficiently distinguishing between boosted top jets, W jets, and QCD jets at extremely high transverse momenta (multi-TeV range). We focus on developing and validating machine learning-based top and W taggers rather than optimizing the analysis flow for setting cross-section limits on BSM scenarios. The example analyses presented in this paper are illustrative, and the analysis strategy can be refined further to improve the cross-section limits presented here. Our goal is to lay the groundwork for future studies rather than striving for the most stringent limits.

The outline of this paper is as follows: In Section 2, the physics models we consider are described. A brief description of the proposed FCC facility is provided in Section 3. Details of event simulation are discussed in Section 4. The challenges that occur while reconstructing boosted jets at the $\sqrt{s} = 100$ TeV collider are highlighted in Section 5. It discusses the difference between the p_T of generated jets and reconstructed jets, followed by a detailed discussion about jet radius, jet substructure observables, and boosted W boson jets that may appear in the final states of various BSM scenarios, including those above mentioned BSM scenarios. The section also addresses the effect of finite calorimeter and tracker resolution on the jet observables, along with the impact of jet grooming. Details of the ML models used in this study are provided in Section 6. Finally, the analyses of the three benchmark BSM scenarios are presented: a heavy neutral Z' boson in Section 7.1, a heavy neutral CP-even Higgs boson in Section 7.2, and a high-mass vector-like bottom-partner (B') in Section 7.3. The conclusions and outlook are summarised in Section 8.

2 Theoretical Scenarios

At the LHC, the top quarks and W bosons are produced via the electroweak or strong interaction. They can also originate from some BSM physics interactions, such as the decay of some heavy new particles predicted by BSM theories. There are several BSM scenarios where heavy resonances are produced, which then decay to top quarks. The top quark will eventually decay to Wb in its final state, and depending on the hadronic or leptonic decay of the W boson, different signatures may emerge at the hadron collider. Similarly, heavy BSM particles may also act as a source of SM gauge bosons like W . After being produced, W can decay to leptons and neutrinos or light jets. In this analysis, we take into account three such BSM scenarios, which act as an additional source of top quarks and W bosons in addition to the SM.

To begin with, we consider a BSM scenario that involves a heavy neutral gauge boson, Z' , in addition to the SM spectrum. Such a heavy gauge boson is generic to many BSM scenarios, e.g., in the $U(1)$ extended models [9, 10], Left-Right symmetric models (LRSM) [90–92], 3-3-1 model [93], Vector-leptoquark model [94], top-phillic Z' model [95, 96], etc. Z' may have a kinetic mixing with the SM Z boson, and depending on the symmetries of corresponding models, it can decay into SM fermions. If the mass of Z' is quite high, it makes its decay products very boosted [97–100]. The searches for a neutral heavy gauge boson by the ATLAS and CMS collaboration have put an exclusion limit on the mass of such particles. For example, the recent results from the ATLAS collaboration, where they have searched for a Z' boson decaying into a pair of top quarks at the 13 TeV run of LHC with 139 fb^{-1} integrated luminosity [100], have placed the strongest exclusion limit on the mass of the Z' to be 2.5 TeV in the context of boosted top topology.

If kinematically allowed, a Z' can decay into a pair of top quarks. In the context of FCC-hh where the center of mass energy is 100 TeV, the FCC-hh can directly produce such a gauge boson with a very high mass (\sim tens of TeV). In this analysis, we have generated a multi-TeV scale Z' boson, and depending on its mass we consider four benchmark points where $m_{Z'} = 5, 10, 15$ and 20 TeV. We generate Z' via the process $pp \rightarrow Z' \rightarrow t\bar{t}$ at 100 TeV run of FCC-hh using PYTHIA 8 (see the Feynman diagram in figure 5a). The top quarks decaying from such a heavy Z' will be highly boosted. Figure 1 represents the transverse momenta of such boosted top quarks for four different masses of the Z' . Similar final states ($t\bar{t}$) also arise in the SM due to QCD interactions, e.g., $pp \rightarrow t\bar{t}$ production, which is an important background for $Z' \rightarrow t\bar{t}$ search. The SM dijet production ($pp \rightarrow jj$) also acts as a major background process in the search for Z' . In section 7.1, we have discussed the signal-background analysis for Z' in detail.

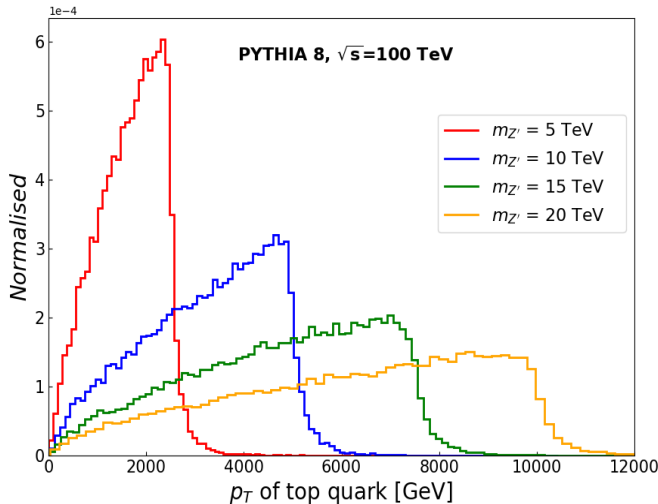


Figure 1: Transverse momentum distribution of top quark coming from the decay of a Z' boson produced at the FCC-hh.

Next, we consider another BSM scenario that involves a heavy CP-even Higgs boson. Theories involving one or more heavy neutral and charged scalars have been extensively studied in the literature. One popular example is the Two Higgs Doublet Model (THDM) [12–18]. In addition to that, many of the well-studied BSM theories like Minimal Supersymmetric Standard Models (MSSM) [101–107], Left-Right Symmetric Models (LRSM) [90–92, 108], Extra-Dimensional models [109, 110], Grand Unified Theories (GUTs) [111, 112], multi-Higgs Doublet models [113–118], Georgi-Machacek model (GM) [119–125] have at least one heavy CP-even scalar other than the SM-like light Higgs boson in its mass spectrum. Both ATLAS and CMS collaborations have searched for such heavy scalars, neutral as well as charged [126–135]. Such a scalar particle may decay to a pair of SM fermions or SM gauge bosons. It may also have a decay mode to SM like Higgs bosons or any BSM particles, depending on the theoretical model. The CMS collaboration has set an upper limit the production cross-section times branching ratio of a heavy neutral Higgs boson produced via gluon-gluon fusion (ggF) and followed by a leptonic decay of the W boson [126]. This analysis has excluded the mass of the heavy Higgs boson till 1060 GeV.

The FCC-hh shall be able to produce a much heavier Higgs boson. Just as in the case of Z' , here too we choose four benchmark points by varying the mass of H , i.e., $m_H = 5, 10, 15, 20$ TeV. In the case of Z' , we discussed a scenario where we were interested in the topology of boosted tops. Here, we present a different scenario where our focus will be to tag boosted W

jets originating from the decay of H . Using PYTHIA 8, we generate the heavy neutral Higgs boson via ggF process at the FCC-hh which then decays into a pair of W bosons that decay hadronically to jets (see the Feynman diagram figure 5b).

The decay of such massive Higgs bosons results in ultra-boosted W bosons. Figure 2 depicts the transverse momentum (p_T) of the boosted W s considering four different heavy Higgs boson masses. As observed from the figure, W bosons from the decay of the massive Higgses are extremely boosted (very large p_T). In this case, the major SM background processes include W^+W^- pair production, $t\bar{t}$ production, and dijet production, the analysis of which is presented in detail in Section 7.2.

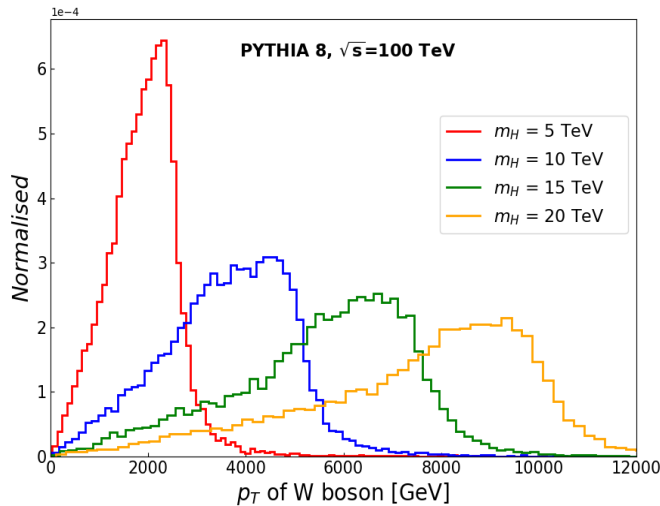


Figure 2: Transverse momentum distribution of W boson produced from the decay of the heavy Higgs at the FCC-hh.

The last model that we consider in our current analysis is a BSM scenario involving a vector-like quark (VLQ). A vector-like fermion is a Dirac fermion whose left and right-chiral components have similar transformations under the SM gauge group. Thus, their representations are free from chiral anomaly. The minimal model for a VLQ analysis could be a VLQ singlet or doublet added to the SM Lagrangian. Theories with one or more VLQs have been considered in the literature where different multiplets of VLQs have been added to the SM Lagrangian and their exotic decay modes, and related phenomenology were studied [136–143].

A generic VLQ model may be categorised into models having bottom-like (B') or top-

like (T') partners, or models where the VLQ has fractional charges other than $-1/3$ or $2/3$ [136, 141, 142]. ATLAS and CMS collaboration have extensively searched for B' and T' quarks in the 13 TeV run of LHC [144–152] via its various decay modes. In many BSM theories, B' or T' quarks mainly interact with third-generation SM quarks. Such a VLQ may have several decay patterns. Depending on the charge of the VLQ, it can decay to a top (or bottom) quark and a W boson (or SM/BSM particle, for example, SM Higgs/Heavy Higgs/ Z boson, etc.) [153–155]. If the mass of the VLQ is quite heavy, then the decayed top quark shall be highly boosted. In such a case, the decay products of the top become highly collimated, and separating them from the usual background of jets becomes challenging. The search for VLQs with boosted top signatures has been performed in multiple studies [156–161]. The ATLAS collaboration has searched for a vector-like T' quark at 13 TeV LHC run where T' decays to a top quark and a Z boson. The top quark further decays to the Wb final state, followed by a hadronic decay of the W boson, and the Z boson decays to a pair of neutrinos. They have carried out the analysis with boosted top topology and have quoted the lower mass limit of the VLQ to be 1.8 TeV [161]. CMS collaboration has also searched for vector-like B' quark decaying to a W boson and a top quark at 13 TeV run with 138 fb^{-1} integrated luminosity. This analysis excludes the mass of B' quark up to 1.56 TeV [156].

At FCC-hh, VLQs can be produced with masses of tens of TeV. We consider a BSM scenario where we have added one $SU(2)$ singlet bottom-like VLQ, $B' \sim (3, 1, -1/3)$, to the SM Lagrangian which interacts with the first and third generation SM quarks [153–155]. The interactions relevant for our study reads as [155],

$$\mathcal{L} \supset \frac{g\tilde{g}}{2} \left[\sqrt{\frac{R_L}{1+R_L}} \bar{B}'_L W_\mu^- \gamma^\mu u_L + \sqrt{\frac{1}{1+R_L}} \bar{B}'_L W_\mu^- \gamma^\mu t_L \right] + \text{h.c.} \quad (2.1)$$

where, g stands for $SU(2)_L$ gauge coupling constant of SM, \tilde{g} and R_L are real parameters. This B' can be singly or pair-produced at the LHC via the electro-weak or the strong processes. We use the model file described in Ref. [153] and set the coupling parameter values fixed at $\tilde{g} = 0.1$ and $R_L = 0.5$. A 5 TeV and a 10 TeV B' are produced in association with a light jet using the UFO file in [162] and the event generator Madgraph v2.9.18 [163]. The B' decays to tW with maximum branching ratio (BR) compared to its other decay modes [153, 154]. The top quark then further decays to Wb with almost a 100% branching ratio (see the Feynman diagram figure 5c). A heavy B' quark will cause the top quark and W boson to be highly boosted. In Figure 3, we present the transverse momenta (p_T) of the boosted top quark and the boosted W boson produced in the B' decay for two different masses of B' at the FCC-hh using PYTHIA 8. We observe that the p_T of the light jet produced in association with B' is very small compared to the p_T of the top quark or W boson. The top quark and the W boson have almost similar p_T distributions. Therein arises an issue where a W jet

can be mistagged as a top jet or a QCD jet. Similar SM processes as discussed earlier will act as major backgrounds for this signal. The signal-background analysis considering this benchmark model has been described in section 7.3.

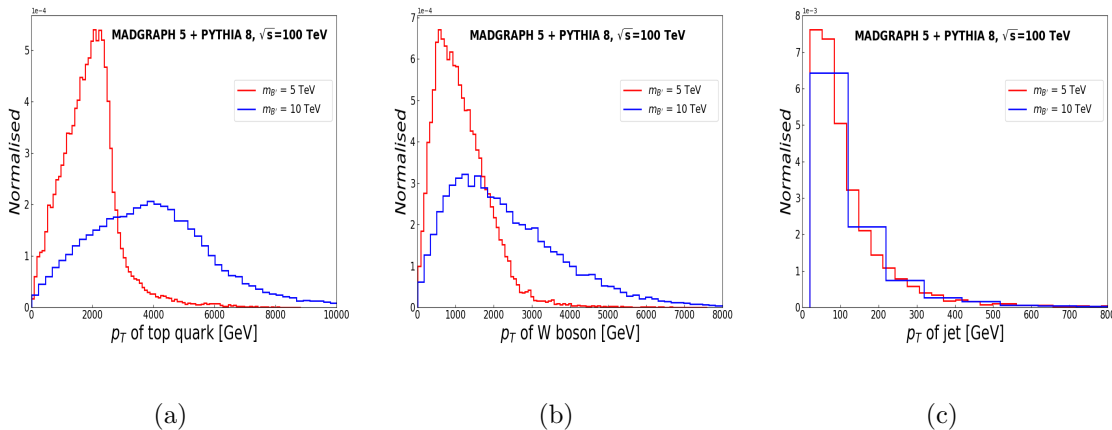


Figure 3: Distribution of transverse momentum of (a) top quark coming from the decay of B' , (b) W boson coming from the decay of B' and (c) the light jet, for two different mass values of singlet B' produced at the FCC-hh.

In the following sections, we first discuss the FCC detector and the event simulation elaborately, followed by the challenges and possible solutions while dealing with boosted top quark and boosted W bosons. Then, we present our results in detail, considering the above-mentioned theoretical scenarios.

3 CERN FCC facility

The Future Circular Collider (FCC) [19] is a proposed particle accelerator designed to push the boundaries of the energy frontier and significantly surpass the center-of-mass energies of previous colliders like the LHC. The FCC project includes three main planned scenarios: FCC-ee for electron-positron collisions, FCC-eh for electron-hadron collisions, and FCC-hh for hadron-hadron collisions. The FCC-hh aims for a center-of-mass collision energy of 100 TeV, which is nearly seven times higher than the LHC. It will offer a very exciting opportunity to explore physics at the multi-TeV scale. The collider will be housed in a 100 km tunnel, making it the largest particle accelerator ever built. The main motivation for FCC-hh is the exploration of the energy frontier as best as possible. With an unprecedented center-of-mass energy of 100 TeV, it will significantly extend the mass reach for discovering new BSM particles. The collider will enable precision measurements of the Higgs boson, top quark,

and electroweak symmetry-breaking properties, surpassing the capabilities of the LHC. The high energy and luminosity of FCC-hh will allow for detailed studies of rare processes and interactions, providing insights into the fundamental forces of nature.

One of the key technological challenges is the development of high-field superconducting magnets, which are essential for bending the proton beams along the collider’s circular path. The FCC-hh will also require advancements in cryogenics and vacuum systems to maintain the necessary conditions for particle collisions. The magnetic dipole system shall offer a field of up to 16 Tesla using Nb₃Sn superconducting magnets. The FCC-hh is planned to have two high luminosity and two low luminosity interaction points. The detectors for the FCC-hh are designed to handle extreme conditions and highly energetic particles originating from 100 TeV proton-proton collisions. One of the significant challenges is managing the high radiation levels and particle fluxes, which require robust radiation-hard materials and advanced cooling systems. The detectors must also handle high levels of pile-up, where multiple proton-proton collisions occur in the same bunch crossing, complicating data analysis. The detectors of FCC-hh will feature highly granular tracking and calorimetry systems. Over 25 years of operation, it is expected to collect 30 ab⁻¹ of data.

In the following section, we provide an overview of the simulation details employed for generating signal and background events.

4 Simulation of events

We generated the following standard model (SM) processes: QCD dijet production ($pp \rightarrow jj$), pair-production of top and anti-top quarks ($pp \rightarrow t\bar{t}$), pair production of W boson ($pp \rightarrow W^+W^-$), as the source of boosted QCD jets, top jets, and W jets, respectively. These samples are generated using PYTHIA 8 [164] with NNPDF 2.3 LO PDF [165]. We generate the samples in five bins according to p_T of the boosted jet that we wish to tag. The p_T bins considered in this study are 2–4 TeV, 4–6 TeV, 6–8 TeV, 8–10 TeV, 10–12 TeV, 12–14 TeV, and 14–16 TeV. Figure 4 shows the cross-section of the processes as calculated by PYTHIA 8.

Additionally, we have considered BSM processes where we have top quark in the final state. For the Z' production, we have used the $f\bar{f} \rightarrow Z' \rightarrow t\bar{t}$ process in PYTHIA 8. We also generate a neutral heavy Higgs boson (H) that decays to two W jets using the $pp \rightarrow H \rightarrow W^+W^-$ process in PYTHIA 8. We have used four benchmarks of Z' and H , which are $m_{Z'/H} = 5, 10, 15, \text{ and } 20$ TeV, using 10% of mass as their width.

We have used the Singlet B' model UFO [162] for the $pp \rightarrow jB'$ production via MADGRAPH 5 [163], with B' decaying to a t and a W . The width used for our analysis was calculated by

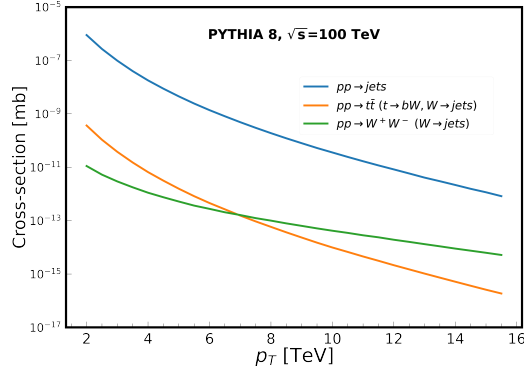


Figure 4: Cross-section as a function of p_T at FCC-hh for the three SM processes considered in this study: $pp \rightarrow jj$, $pp \rightarrow t\bar{t}$, $pp \rightarrow W^+W^-$.

MADGRAPH 5: $\Gamma = 1$ TeV for $m_{B'}$ = 5 TeV and $\Gamma = 9$ TeV for $m_{B'}$ = 10 TeV. To study the effect of width, we also generate events with width half and one-fourth of the original width.

For the PYTHIA 8 was used for showering and hadronisation as in the case of their SM backgrounds. In all the cases, we only consider the hadronic decay of the W boson. Figures 5a, 5b, and 5c show the Feynman diagrams of each of the processes.

All the above-mentioned samples are passed through DELPHES [166] simulation of a typical FCC-hh detector, using the default FCC-hh card [167]. Table 1 shows the resolution of the tracking system and the $\eta - \phi$ segmentation of the Electromagnetic Calorimeter (ECAL) and Hadronic Calorimeter (HCAL) of FCC-hh as parametrised in [167].

Tracker		
$ \eta < 6.0$	$\sigma_\theta = 0.001$	
Calorimeters		
	ECAL	HCAL
$ \eta < 2.5$	$\Delta\eta = 0.01, \Delta\phi = 0.012$	$\Delta\eta = \Delta\phi = 0.025$
$2.5 < \eta < 6.0$	$\Delta\eta = \Delta\phi = 0.025$	$\Delta\eta = \Delta\phi = 0.05$

Table 1: Angular resolution of the tracking system and segmentation in the Electromagnetic and Hadronic calorimeters of FCC-hh as parametrised in [167].

We relied on the particle-flow (PF) event reconstruction in DELPHES, which is based on a simplified approach that combines information from the tracking systems as well as calorimeter towers for event reconstruction. FASTJET [168, 169] is used on the PF candidates to construct jets of radius $R = 0.8$. We choose $R = 0.8$ because it is a typical choice

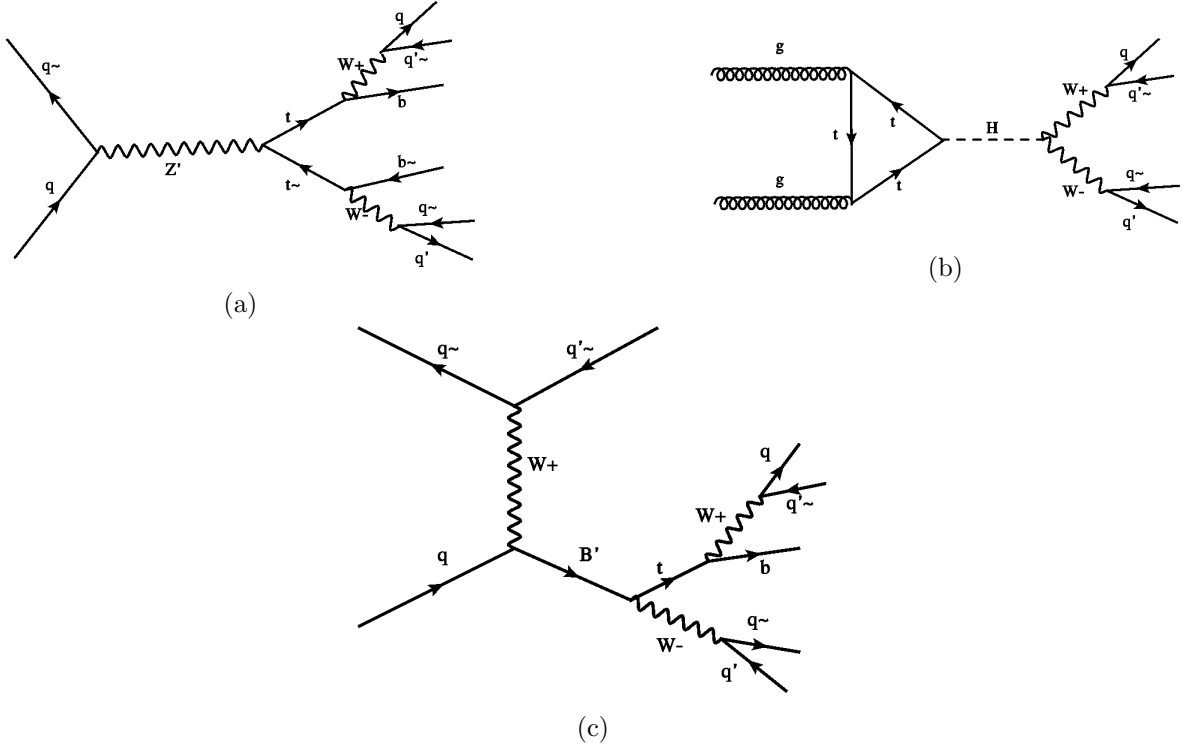


Figure 5: Feynman diagrams of the signal processes: (a) s -channel production of Z' , with the $Z' \rightarrow t\bar{t}$ decay where t and \bar{t} decays hadronically. (b) Gluon-gluon fusion production of H decaying via $H \rightarrow W^+W^-$ where the W s decay hadronically. (c) t -channel production of B' with an associated jet and W exchange, where B' decays as $B' \rightarrow tW$ followed by hadronic decay of W .

of jet radius for large-radius jets in the LHC experiments. We select jets that satisfy the pseudorapidity cut of $|\eta| < 2.5$. These jets are then passed through the default flavour tagger modules of DELPHES. In this paper, we have not considered pile-up, which is left as an open topic for future studies.

5 Challenges and mitigation strategies for jets at $\sqrt{s} = 100$ TeV

At the 100 TeV collider, the high center-of-mass energy of pp collision produces heavy BSM particles with mass up to tens of TeVs. When such particles decay into jets, the jets are highly boosted and thus highly collimated. In our study, we consider top and W jets with p_T ranging from 2 TeV to 16 TeV. Reconstructing such particles from their final state requires addressing the unique challenges posed by these extreme energies. This section explores these challenges and discusses potential techniques to overcome them.

5.1 Migration of jet transverse momentum

As stated earlier, the top jets and the QCD have been generated in fixed p_T bins with bin-width of 2 TeV. However, high- p_T boosted objects can suffer from energy loss due to radiative effects and detector resolution, shifting them to lower p_T bins. On the other hand, calorimeters and tracking systems introduce smearing effects that can slightly alter the reconstructed p_T of the jet compared to the original p_T , causing the reconstructed jet p_T to acquire higher values than the generated jet p_T .

Generally, a typical general-purpose detector cannot measure the energy (and p_T) of jets perfectly. The measured energy of a jet is usually corrected to match it with the true energy of its parent parton. The correction factors are generally functions of momentum and pseudorapidity, and they help to bring the p_T of the reconstructed jet in line with the generated jet. We study the extent to which the p_T of the reconstructed jets ($p_T^{(jet)}$) differ from the p_T of the generated jets ($p_T^{(gen)}$) at FCC-hh.

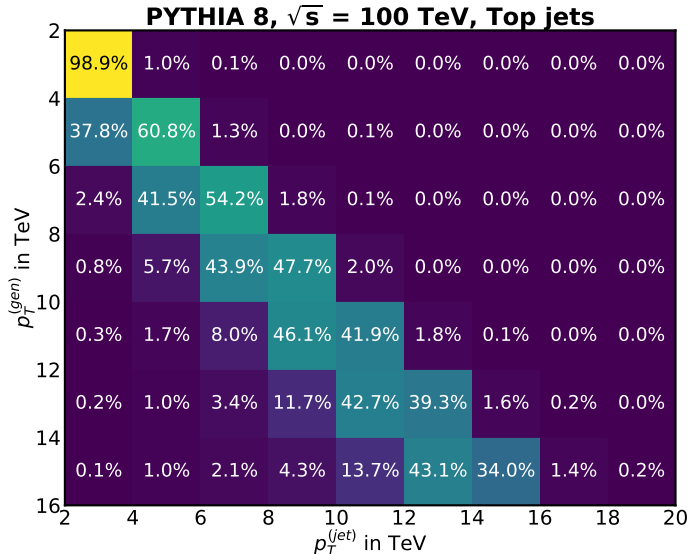


Figure 6: Migration matrix showing percentage of jets with p_T of generated jet ($p_T^{(gen)}$) losing energy to acquire reconstructed jet p_T ($p_T^{(jet)}$).

Figure 6 shows the phenomenon of p_T bin migration in top jets. We see that as the $p_T^{(gen)}$ increases, so does the spread of the jets to lower p_T bins. This phenomenon is also true for QCD and W jets. A few percent of the jets are smeared to higher p_T though the upward p_T migration, but the extent of upward p_T migration is much smaller compared to the downward migration. We saw in Section 2 that a heavy BSM particle produced in the

$\sqrt{s} = 100$ TeV collider can decay to top quarks with p_T in the multi-TeV range. Considering the phenomenon of bin migration, we need to construct a tagger that caters to multiple p_T ranges because the characteristics of top jets must vary widely across the entire p_T range.

5.2 Effect of fixed jet radius on top and QCD jet mass

At sufficiently large boosts, the final-state hadrons from decays of resonances (like W boson or top quark) merge into a single jet. The jet mass is a potent discriminator between resonance jets and background QCD jets (i.e., jets originating from the light-flavour quarks or gluons). The distribution of jet mass (m_{jet}) for the top and QCD jets constructed with the radius of the jet, $R = 0.8$, are shown in Figure 7. The jets carry p_T in the range of 2–4 TeV, 6–8 TeV, 10–12 TeV, and 14–16 TeV.

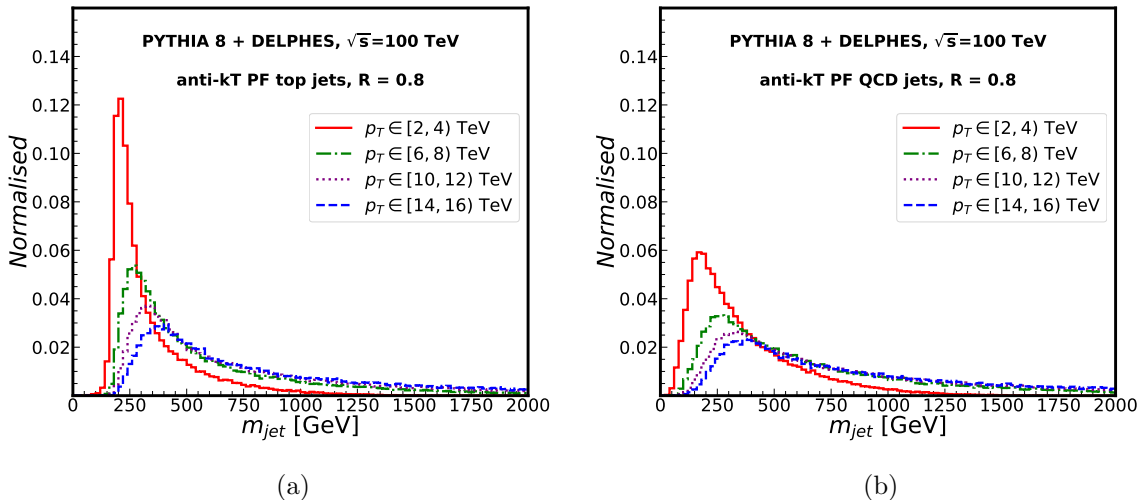


Figure 7: Normalised m_{jet} distribution of (a) top jets and (b) QCD jets with transverse momenta (p_T) of 2–4 TeV, 6–8 TeV, 8–10 TeV, and 14–16 TeV. Jets have been constructed with a fixed jet radius $R = 0.8$.

The mean squared invariant mass of a QCD jet in the collinear approximation is given by [170–172],

$$\langle m^2 \rangle \simeq C \cdot \frac{\alpha_S}{\pi} p_T^2 R^2 \quad (5.1)$$

where C is a coefficient that depends on the jet algorithm. At high p_T and with a fixed jet radius R , the mass increases, as shown in Figure 7. In addition, the jet captures contamination from the initial-state radiation (ISR), final-state radiation (FSR), and underlying events (UE).

As described in [172], in the case of highly boosted top jets, the FSR from the top quark is not dead-cone suppressed any more, as the dead cone radius shrinks as $\simeq m_{\text{top}}/p_T$ for very high p_T . On the other hand, a single emission at the jet boundary with transverse momenta $p_{T,ISR}$ can substantially change the jet mass, as

$$m^2 \simeq m_{\text{top}}^2 + p_T \cdot p_{T,ISR} \cdot R^2 \quad (5.2)$$

The authors in [172] showed that an ISR jet with transverse momenta $p_{T,ISR} \sim m_{\text{top}}^2/p_T R^2$ can change the jet mass by $\mathcal{O}(1)$. At the FCC, where p_T can reach tens of TeV, radiative emissions of a few GeV can alter and increase the jet mass. The large tail in the jet mass distribution manifests in QCD jets, too, as seen in Figure 7b. To mitigate the above issues and reduce the contamination, we make use of a dynamic jet radius [173, 174]. The choice of the jet radius R is crucial because not only should the jet algorithm reconstruct the top quark well, but it also should be able to mitigate the contamination from underlying events.

5.2.1 Jet radius estimation at the parton level

To choose the radius that captures the correct jet substructure, we go back to the parton level information of top jets. We generate $pp \rightarrow t\bar{t}$ process at $\sqrt{s} = 100$ TeV using PYTHIA 8. We use PYTHIA 8 for parton shower, hadronisation, and decay. The top quark (t) decays to a b quark and a W boson, which in turn decays hadronically to a light quark and an anti-quark, which we shall refer to as u and d . We generate the $t\bar{t}$ events in seven different p_T bins: 2–4 TeV, 4–6 TeV, 6–8 TeV, 8–10 TeV, 10–12 TeV, 12–14 TeV, and 14–16 TeV.

The top decay products lie within a cone, whose size depends on the initial p_T . For events in each bin, we calculate the distance ΔR between the parent top quark t and its three daughter quarks, b , u , and d . We then find out the maximum of the three distances, $\Delta R^{\text{max}} = \text{max}(\Delta R_{tb}, \Delta R_{tu}, \Delta R_{td})$. ΔR^{max} serves as an approximate measurement of the cone size. We expect that this number decreases with increasing p_T . Figure 8a displays a two-dimensional matrix of the p_T ranges and the ΔR^{max} values. Each square shows the percentage of top jets with p_T in the i^{th} bin and j^{th} ΔR^{max} .

From Figure 8a, we see that as we move on to higher p_T , the top jets have smaller decay cone size, as denoted by the smaller ΔR^{max} . Only 13.4% of tops generated with p_T of 2–4 TeV have the b , u , and d contained fully within $\Delta R = 0.1$, while in the case of 14–16 TeV tops, the number is 95.5%. Using this information, we can estimate the cone radius that should be used so that a reconstructed jet contains the full information of the top.

We determine the ΔR^{max} value such that the top quark decay products, b , u , and d , are fully contained within a cone of this radius 95% of the time. We assign this ΔR^{max} value to the lower value of the corresponding p_T bin. For instance, if the top quarks in the 2–4 TeV

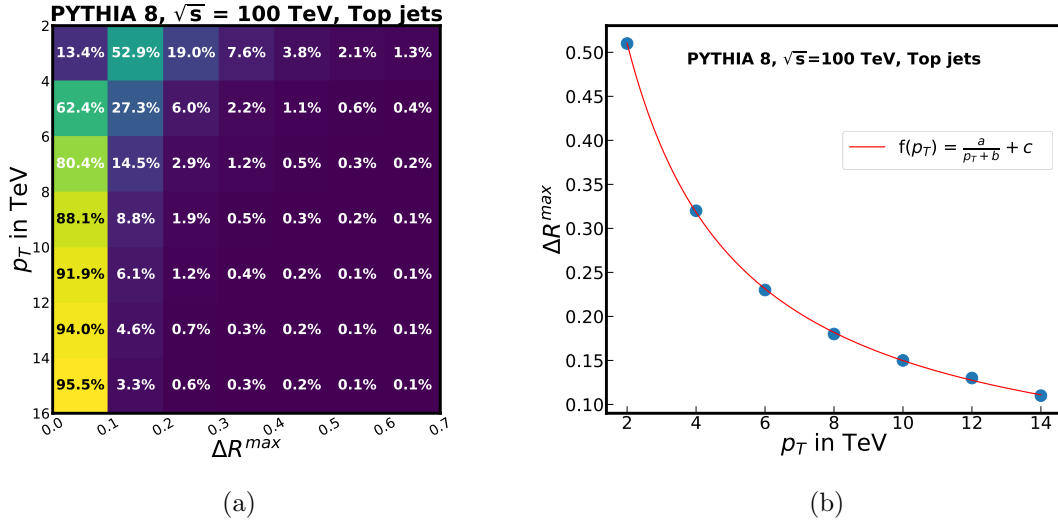


Figure 8: (a) A two-dimensional matrix showing the percentage of $t \rightarrow bW(W \rightarrow ud)$ events that have all the three daughter partons within radius ΔR^{max} from the mother top quark. (b) The variation of the ΔR^{max} value with 95% success rate of containing the full top decay, as a function of the p_T of the top quark. Here, $f(p_T)$ is the fitting function.

have a ΔR^{max} of 0.5, we use 0.5 for 2 TeV. Similarly, if the 4–6 TeV bin has a ΔR^{max} of 0.3, we use 0.3 for 4 TeV, and we follow this for all the remaining bins. In Figure 8b, we have plotted the ΔR^{max} corresponding to each p_T bin. We fit the data points using a function of the form,

$$f(p_T) = \frac{a}{p_T + b} + c \quad (5.3)$$

where a , b , and c are fitting parameters, which are set to 1.64, 1.3, and 0.001, respectively. The dependence of R on the inverse p_T is inspired by the approach in [172]. As the p_T reaches ≈ 15.7 TeV, ΔR^{max} goes below 0.1.

In the later part of our work, we use the function to calculate the jet radius dynamically instead of using a fixed radius.

As stated earlier, we construct anti- k_T jets using FASTJET on particle-flow (PF) objects, using a fixed radius of 0.8. Now we recluster the jet constituents using the p_T dependent function in Equation 5.3. Figure 9 shows the distributions of jet mass for top jets and QCD jets after reclustering.

As seen in Fig 31a and 31b, using a dynamic jet radius that is a function of the jet's p_T corrects the jet mass. The jet mass falls off faster in this case. However, the peak of the jet mass and the width of the distribution still increase with increasing p_T . This indicates that

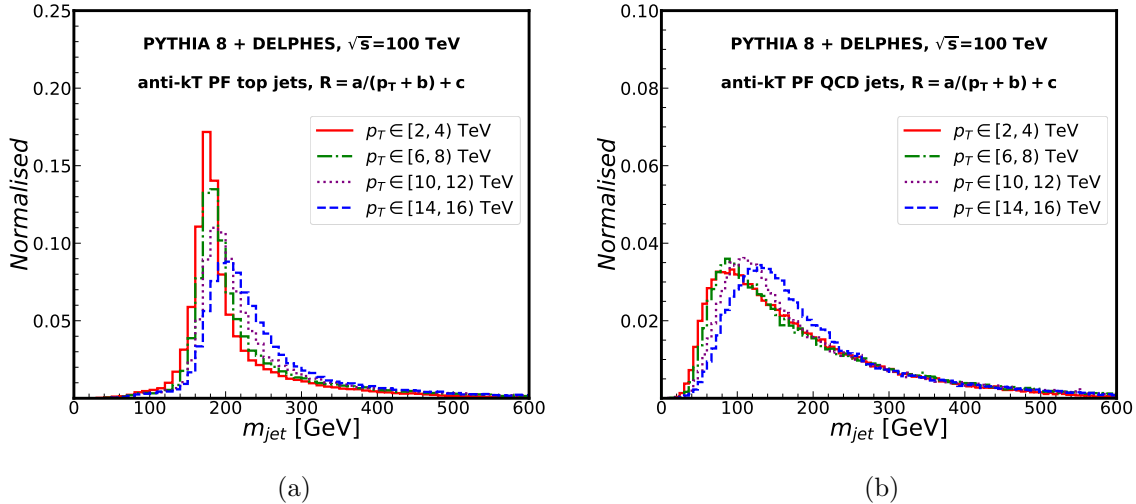


Figure 9: Normalised m_{jet} distribution of top jets and QCD jets with transverse momenta (p_T) of 2–4 TeV, 6–8 TeV, 8–10 TeV, and 14–16 TeV. The jet constituents have been reclustered using radius $R(p_T) = a/(p_T + b) + c$.

even with the new dynamic radius, the contamination could not be completely eliminated.

5.3 Effects of finite detector resolution on top and QCD jet mass

To further investigate the source of the high jet mass, we look into the detector parametrisation of the 100 TeV collider because the energy-momenta of the jet constituents depends to a large extent on the resolution of the detector elements. As stated in Section 4, we use the DELPHES modelling of the FCC-hh detector for simulation. The resolution used in the calorimeters and the tracking system are listed in Table 1. Since we are using particle-flow (PF) objects, consisting of tracks and calorimeter towers, we focus on the resolution effects of these two detector elements.

5.3.1 Calorimeters

The proposal for the electromagnetic calorimeter (ECAL) and the hadron calorimeter (HCAL) of the FCC-hh collider assumes a $(\Delta\eta, \Delta\phi)$ segmentation of (0.01, 0.012) and (0.025, 0.025) respectively in the central region. The energy deposits of the particles in a tower are termed *hits*. The energy deposits are smeared by a log normal distribution with a standard deviation $\sigma(\eta, E)$, which is also the resolution, given by:

$$\left(\frac{\sigma}{E}\right)^2 = \left(\frac{S(\eta)}{\sqrt{E}}\right)^2 + C(\eta)^2 \quad (5.4)$$

where E is the energy of the particle, η is the pseudorapidity, S and C are the *stochastic* term and the *constant* term respectively. We have neglected the *noise* term: $(N(\eta)/E)^2$, as it does not contribute much at high energies. In fact, for highly energetic particles, $C(\eta)$ contributes dominantly to the energy resolution of the calorimeters. For FCC-hh, the terms are listed in Table 2.

	$ \eta < 1.7$	$1.7 < \eta < 4.0$	$4.0 < \eta < 6.0$
S_{ECAL}	10%	10%	30%
C_{ECAL}	0.7%	0.7%	3.5%
S_{HCAL}	50%	60%	100%
C_{HCAL}	3%	3%	10%

Table 2: The stochastic and constant terms of the energy resolution of ECAL and HCAL as a function of pseudorapidity in the conceptual detector design of FCC-hh.

The DELPHES algorithm iterates over a collection of tower hits and processes them to fill a tower by adding the total energy deposited in the tower. The tower’s $\eta - \phi$ is then calculated as the $\eta - \phi$ of the cell’s geometric centre, smeared by a Gaussian distribution. The four-momentum of the tower is recalculated from the η, ϕ, E information.

We construct two hypothetical scenarios to study the effects of the finite energy resolution and segmentation of calorimeter cells. First, we set the stochastic and constant terms in the ECAL and HCAL resolution parameter σ to a very low value of 0.1%, i.e., $S = C = 0.1\%$. This reduces the extent to which the energy can be smeared. Then, we use a more granular segmentation of the HCAL by setting the cell size of HCAL towers to that of the ECAL towers. Reducing the HCAL cell size increases the number of cells within the jet clustering radius. Figure 10 shows the jet mass distribution for 2–4 TeV jets (Figures 10a, 10b) and for 14–16 TeV jets (Figures 10c, 10d).

Improving the energy resolution did not affect the jet mass reconstruction. On the other hand, increasing the $\eta - \phi$ segmentation of the HCAL towers by a factor of two changes the reconstructed jet mass substantially for the 14–16 TeV jets, although it does not affect the 2–4 TeV jets. The 14–16 TeV top jets have a sharper peak, and the overlap between the top and the QCD jets increases as the QCD distribution peaks at lower values. The improved angular resolution of the HCAL allows the highly collimated decay products of the 14–16 TeV to deposit energy in an increased number of highly granular tower cells, causing the PF reconstruction to be more efficient when matching the charged tracks to towers. For 2–4 TeV jets, the default segmentation already offers sufficient granularity to resolve the particles, hence increasing the segmentation does not provide much improvement.

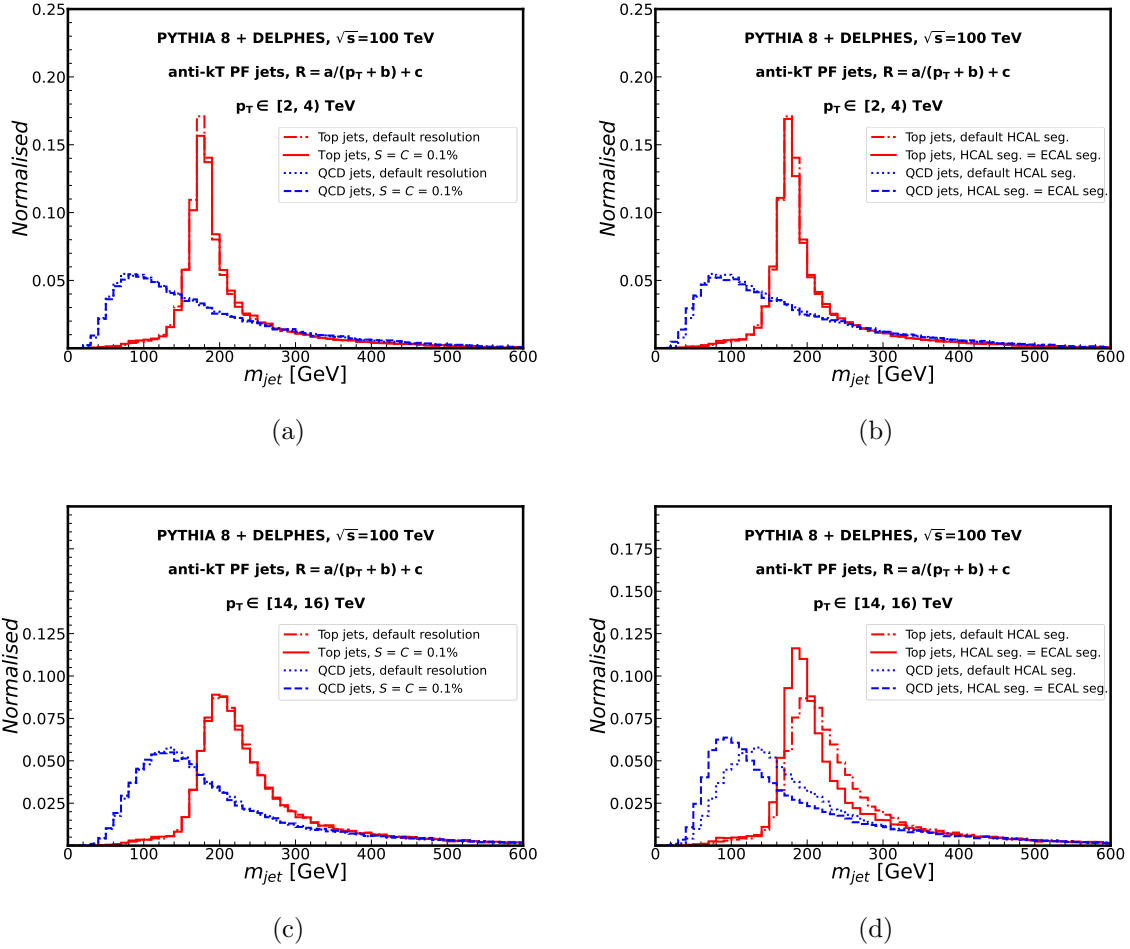


Figure 10: Normalised m_{jet} distribution of 2–4 TeV ((a), (b)) and 14–16 TeV ((c), (d)) top jets and QCD jets using different calorimeter configurations. Subfigures (a), (c) show the change in m_{jet} when the energy resolution is varied. Subfigures (b), (d) show the change in m_{jet} when the angular resolution is varied.

To conclude, we find that in the study of ultra-boosted objects, granularity plays a more important role than energy resolution, as seen in Figure 10d. If such a fine granularity, where HCAL and ECAL cell sizes were of the same size, is indeed feasible to construct at the FCC-hh experiment, it will improve the mass reconstruction of highly boosted objects. However, we continue our study with the currently proposed granularity of ECAL and HCAL. We can also obtain a high angular resolution by using charged particle tracks, which we study in the next section.

5.3.2 Tracking system

The proposed angular resolution for tracking in the FCC detector design is $\sigma_\theta = 0.001$, which is an order of magnitude less than that of the ECAL. When two or more tracks are separated with a distance less than σ_θ , the one with the maximum p_T is considered by the dense track filtering algorithm in DELPHES. We calculate the mass on the constituent tracks of the PF jet with reclustered radius (m_{trk}). We also compute $m_{\text{jet}}^{\text{trk}}$ with a degraded tracking resolution, $\sigma_\theta = 0.005$. Figure 11 shows the distribution of mass calculated on tracks for 2–4 TeV (11a) and 14–16 TeV jets (11b), with two values of the σ_θ .

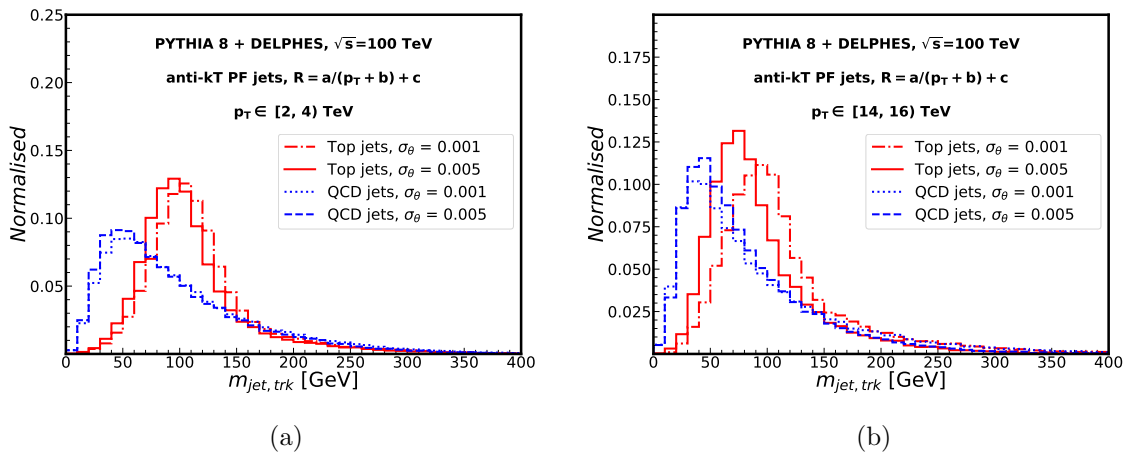


Figure 11: Normalised track-based m_{jet} distribution of (a) 2–4 TeV and (b) 14–16 TeV top jets and QCD jets with varying angular resolution of the tracker.

The mass distribution for tracks assumes lower values because they do not capture the full energy of a jet. Additionally, as we see in Figure 11, $m_{\text{jet}}^{\text{trk}}$, especially for top jets, is very sensitive to the angular resolution. The track-based mass needs to be rescaled with a ratio of the original jet p_T to the track p_T [172] if we want to obtain the correct estimation of the jet mass. In the next section, we perform a similar study and check the detector effects on the jet substructure.

5.4 Effects of finite detector resolution on N-Subjettiness observables

For the purpose of identifying the top jets and QCD jets based on their substructure properties, a popular method is the use of the N-Subjettiness [25] (τ_N) observable, which measures the *prongness* of a jet relative to N subjet directions \hat{n}_j ,

$$\tau_N^{(\beta)} = \frac{1}{\sum_{\alpha \in \text{jet}} p_{T,\alpha} R_0^\beta} \sum_{\alpha \in \text{jet}} p_{T,\alpha} \min_{k=1,\dots,N} (\Delta R_{k,\alpha})^\beta \quad (5.5)$$

where β (which should be greater than zero) is an arbitrary weighting exponent to guarantee infrared safety. For a jet having N subjects, $\tau_N < \tau_{N-1}$ and the ratio τ_N/τ_{N-1} is small.

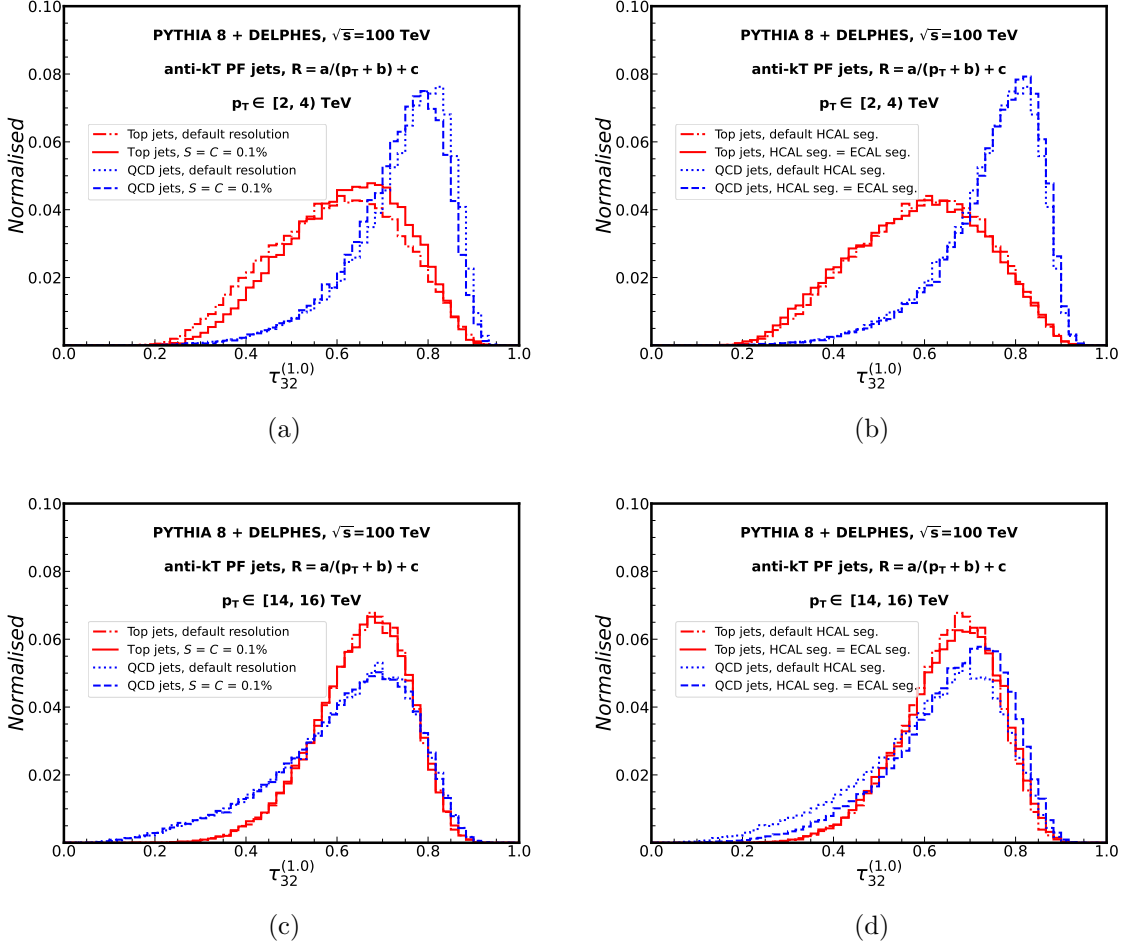


Figure 12: Normalised $\tau_{32}^{(1.0)}$ distribution of 2–4 TeV ((a), (b)) and 14–16 TeV ((c), (d)) top jets and QCD jets using different calorimeter configurations. Subfigures (a), (c) show the change in $\tau_{32}^{(1.0)}$ when the energy resolution is varied. Subfigures (b), (d) show the change in $\tau_{32}^{(1.0)}$ when the angular resolution is varied.

In top quark decays, which yield three distinct subjects, the ratio τ_3/τ_2 is expected to exhibit a peak at lower values, distinguishing it from the QCD background, which peaks at higher values. Figure 12 shows the distributions of $\tau_{32}^{(1.0)} = \tau_3/\tau_2$ for 2–4 TeV and 14–16 TeV jets with modifications to the energy and the angular resolution of the calorimeters.

To begin with, we note that the discrimination between top and QCD jets in terms of $\tau_{32}^{(1)}$ degrades with an increase in the transverse momenta of the jets. Not only is there a greater overlap between the two for 14–16 TeV jets, but the top and the QCD jets follow reverse trends in τ_{32} . In other words, the N-Subjettiness observable breaks down at high transverse momenta, even with the $(\Delta\eta, \Delta\phi) = (0.01, 0.01)$ calorimeter resolution at the FCC-hh. Improving the HCAL resolution corrects the observable to some extent, but is not sufficient to be advantageous as a tagger. Variable τ_{21} also exhibits similar behavior. We now calculate the observable on the tracks.

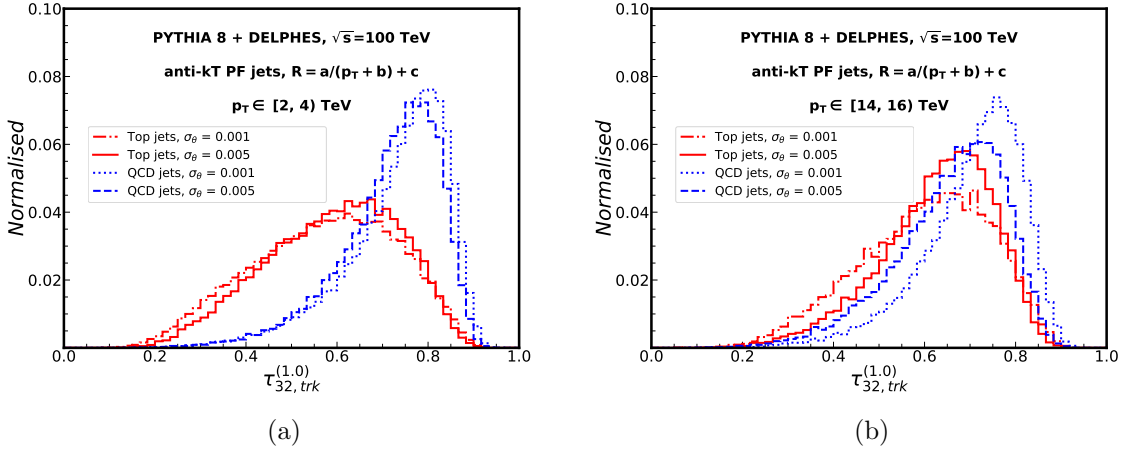


Figure 13: Normalised track-based $\tau_{32}^{(1,0)}$ distribution of (a) 2–4 TeV and (b) 14–16 TeV top jets and QCD jets with varying angular resolution of tracker.

Figure 13 shows that an angular resolution of 0.001 in the tracker is beneficial for the boosted jets. The finer track resolution restores the correct substructure properties of the 14–16 TeV jets. As in the case of jet mass, decreasing σ_θ degrades the N-Subjettines.

From our studies of the detector effects on the jet mass and τ_{32} , we make the key observation that a full and accurate reconstruction of the momentum and the jet substructure at tens of TeV is limited by finite resolution of the calorimeters. Even the particle-flow reconstruction that uses both track and calorimeter information fails to resolve the substructure at high p_T . The tracker volume with the proposed angular resolution of $\sigma_\theta = 0.001$ comes to the rescue. Solely track-based N-Subjettiness captures the *prongness* successfully. However, one must keep in mind that this is the best-case scenario that does not take pile-up into consideration. Further studies with pile-up are required to see if the track-based observables work in that situation.

5.5 Boosted W jets at $\sqrt{s} = 100$ TeV

As discussed in Section 2, the production of a vector-like quark (VLQ) B' at the FCC-hh that can decay into a top quark and a W boson is not only a source of highly boosted top jets but also highly boosted W jets. Figure 3 shows the full range of transverse momenta of such W jets coming from the decay of a B' , reaching up to 14 TeV for a B' of mass $m_{B'} = 20$ TeV. In the previous section, we discussed the challenges that may arise while reconstructing top jets and the possible ways to mitigate them. First, we cluster the PF candidates with a radius R that is p_T dependent. This reduces the contamination by radiative effects. Next, we saw that the track-based jet substructure observable τ_{32} acts as a potent discriminant between the top and the QCD jets, even at high p_T . Similar challenges shall arise while reconstructing the W boson.

To study boosted W jets, we pair-produce W boson from a pair of quarks at $\sqrt{s} = 100$ TeV, where the W boson further decays hadronically to two light quarks. We follow the same simulation procedure as described in Section 4. The W jets are generated in p_T bins of 2–4 TeV, 4–6 TeV, 6–8 TeV, 8–10 TeV, 10–12 TeV, 12–14 TeV, 14–16 TeV. We use the dynamic radius $R(p_T) = a/(p_T + b) + c$ that was optimized for top jets to cluster the particle-flow objects. Figure 14 shows the jet mass distribution of the boosted W jets for four different p_T ranges, with a fixed radius (Figure 14a) and a dynamic radius (Figure 14b).

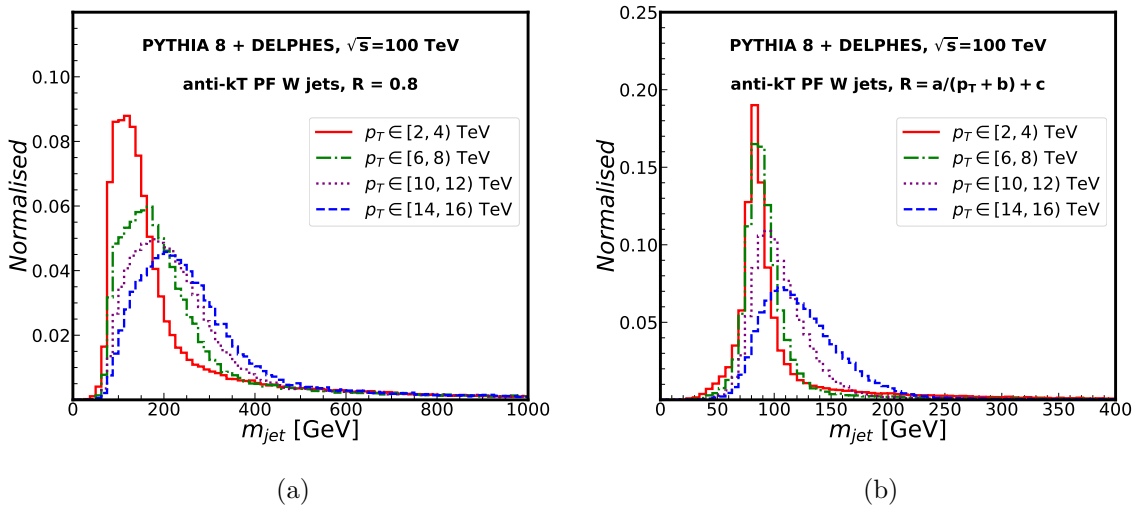


Figure 14: Normalised m_{jet} distribution of W jets (a) before and (b) after reclustering with $R(p_T)$.

As in the case with top and QCD jets, the W jet mass also suffers from radiation at the $\sqrt{s} = 100$ TeV collider though being an electroweak process, the amount is less than that in

the former cases. Using the radius $R(p_T)$, much of the radiative effects could be removed. For $p_T \in [2,4]$ TeV jets, the mass is exactly reconstructed at the W boson mass ($m_W \simeq 80$ GeV). With increasing p_T , the jet mass peak shifts to higher values due to increasing radiative effects and the worsening resolution of the detector.

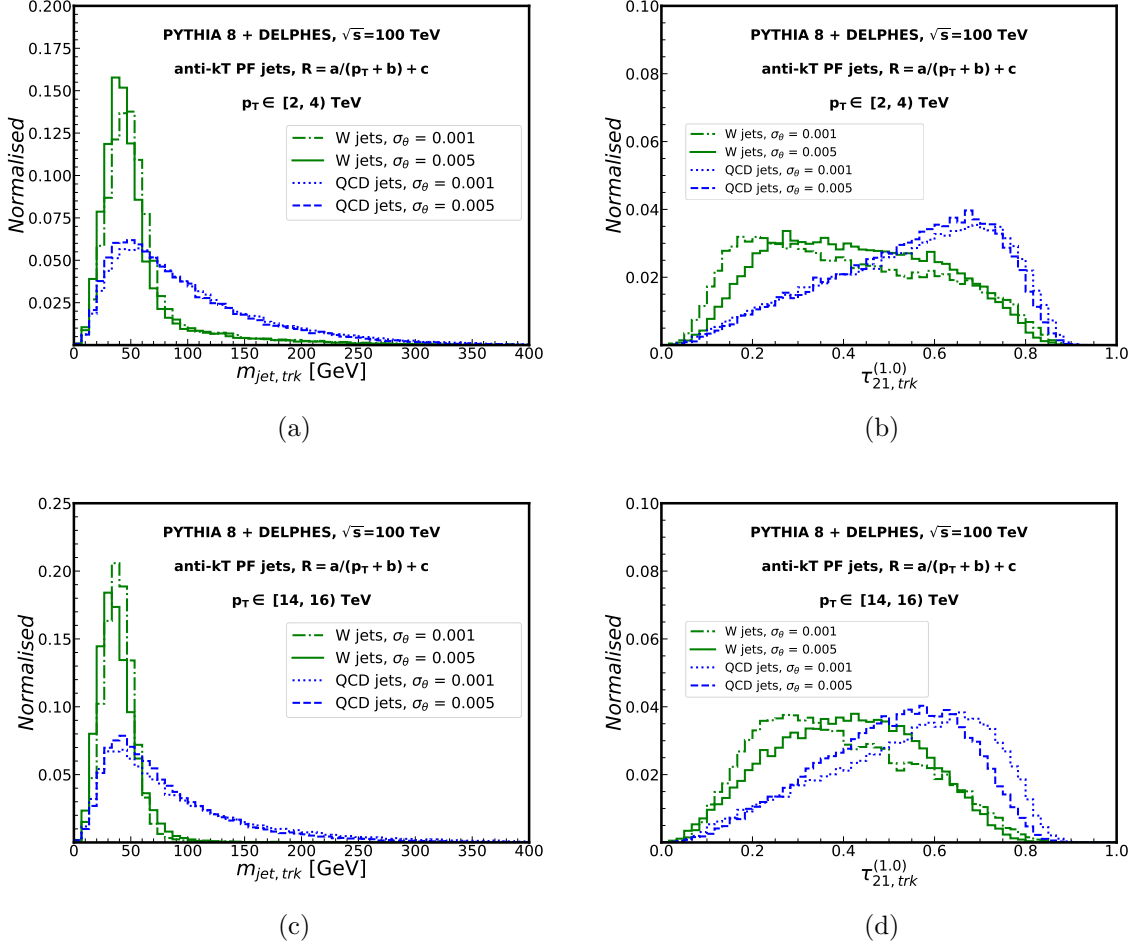


Figure 15: Normalised track-based m_{jet} and $\tau_{21}^{(1.0)}$ distributions of 2–4 TeV ((a) and (b) respectively) and 14–16 TeV ((c) and (d) respectively) top jets and QCD jets with varying angular resolution of the tracker.

Figure 15 shows the distributions of the jet mass and the two-prong N-Subjettiness ratio τ_{21} calculated on tracks for the W jets and the QCD jets from the two extreme ends of the p_T spectrum. Both W and QCD peak at ~ 50 GeV, though QCD features a much longer tail. The track-based τ_{21} shows distinguishing properties between the W and the QCD jets, the former peaking at lower values owing to the two-prong substructure. With the poorer

resolution of tracks, the two tend to overlap with each other.

Using a radius optimized for W jets (using the parton level information of $W \rightarrow q\bar{q}$) could eliminate more of the radiation from the jets. We have used the dynamic radius optimized for top jets while reclustering the W decay products because we primarily wanted to study boosted top signatures. In the next section, we discuss the possibility of making further improvements to the reconstructed jets through jet grooming algorithms.

5.6 Jet grooming techniques

Initial-state radiation and the underlying event can substantially alter the measured jet mass. Jet grooming algorithms are applied to jets to remove contaminating radiation from uncorrelated sources, with the aim of improving the jet mass scale and resolution.

While the reclustering technique using a dynamic p_T dependent jet radius prevented ISR, FSR, and multiparton interactions (MPI) contamination within the jets, we want to see if standard grooming techniques can do better in reducing the residual radiation. We use the soft drop technique [175, 176] on the jets. The original jet with $R = 0.8$ is first reclustered within $R(p_T)$ using the Cambridge/Aachen (C/A) algorithm instead of the anti- k_T algorithm to form a structured tree with angular ordering. Then, the tree is declustered using the following algorithm:

1. Undo the last step of C/A clustering to break the jet j into two subjets j_1 and j_2 .
2. Check if j_1 and j_2 satisfy the condition:

$$\frac{\min(p_{T_1}, p_{T_2})}{p_{T_1} + p_{T_2}} > z_{\text{cut}} \left(\frac{\Delta R_{12}}{R_0} \right)^\beta \quad (5.6)$$

where the two parameters, z_{cut} , the soft drop threshold, and the angular exponent β controls the degree of jet grooming.

3. If the above condition is not satisfied, remove the softer subjet, redefine j to be the harder subjet, and reiterate steps 1 and 2 until criteria 5.6 is satisfied.
4. If the two branchings of jet j pass the condition, j is the final soft dropped jet.

We vary the parameters used for soft drop: $z_{\text{cut}} = 0.05, 0.08, 0.10, 0.20$, and $\beta = 0.2, 0.5, 1.0, 2.0$. Appendix A shows the m_{jet} distributions of top, W , and QCD jets for all possible combinations of the parameters. We calculate the Wasserstein-1 distance [177], a measure of the separation between two distributions, between the m_{jet} distributions of top, QCD, and W jets, and choose the parameters $z_{\text{cut}} = 0.05$, $\beta = 0.5$ that maximize this distance for the

two extreme ends of our p_T range. Figure 16 shows the distribution of the top and the QCD jet mass after using the soft drop algorithm, with $z_{\text{cut}} = 0.05$, $\beta = 0.5$ for $p_T \in [2, 4]$ TeV and $p_T \in [14, 16]$ TeV jets.

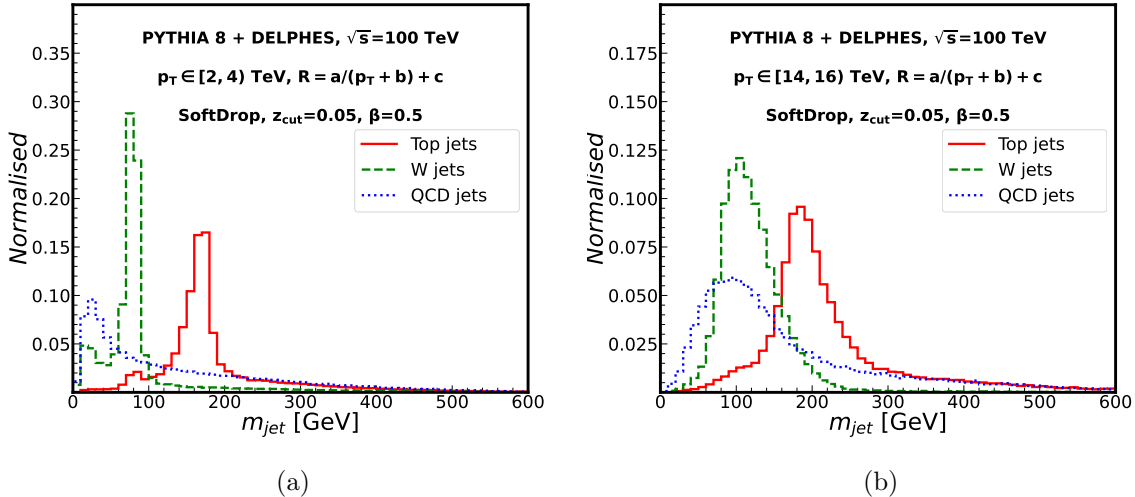


Figure 16: Normalised m_{jet} distribution of (a) 2–4 TeV and (b) 14–16 TeV top jets and QCD jets, after applying softdrop grooming with parameters $z = 0.05$, and $\beta = 0.5$.

The secondary peaks in the m_{jet} distributions of top and W jets appear when the condition in Equation 5.6 removes one of the softer prongs from the multi-pronged jets. This is more evident in 2–4 TeV jets. In 14–16 TeV jets, along with the prongs carrying enough energy to satisfy Equation 5.6, the high boost concentrates the jet constituents with much smaller angular separation.

6 Machine learning techniques for jet tagging

Our goal in the following sections is to perform multi-class classification using these observables as well as jet images to explore how machine learning distinguishes between the three categories of jets in the $\mathcal{O}(1) - \mathcal{O}(10)$ TeV range. The motivation behind designing a multi-class tagger instead of separate binary classifiers is due to its ability to tackle scenarios involving multiple jet types in the final states. For example, in the decay of a vector-like quark (VLQ) B' , both t and W jets are produced, making it essential to simultaneously distinguish between top, W , and QCD jets. Additionally, $t\bar{t}$ jets form a substantial background for BSM processes involving W^+W^- final states, just as W jets can become a major background for

BSM processes with $t\bar{t}$ in the final state. A multi-class tagger effectively addresses these challenges within a single framework.

We first introduce the machine learning (ML) models used in this work for top tagging and W tagging purposes. We generate top jets, QCD jets, and W jets using the process described in Section 4. We have used two kinds of ML algorithms in our work: the image-based convolutional neural network (CNN) that uses low-level inputs in the form of jet images and the variable-based XGBoost that uses high-level, physics-motivated input features such as jet substructure observables. We briefly discuss the architecture of the algorithms below.

6.1 Extreme Gradient Boosted Decision Trees

XGBoost, or eXtreme Gradient Boosting [84], is an efficient, robust and scalable implementation of gradient boosting machines. It is extensively utilized in machine learning due to its impressive speed and performance. XGBoost operates by creating an ensemble of decision trees, where each new tree attempts to correct the errors of the previous ones using a gradient descent algorithm, ultimately minimising the loss function. The key parameters of the XGBoost model include `objective` (loss function), `num_round` (boosting iterations), `learning_rate` (step size), `max_depth` (tree depth), `min_child_weight` (minimum instance weight), and `gamma` (minimum loss reduction). Regularisation parameters like `alpha` (L1 regularisation), `lambda` (L2 regularisation), `subsample` (training instance subsample ratio), `colsample_bytree` (feature subsample ratio) are used to reduce overfitting.

In our work, we use the XGBoost model for three-class classification between top jets, W jets, and QCD jets for the various p_T ranges. We use the multi-class logarithmic loss as the objective function to minimise. We use a `max_depth` of 3 and set the `learning_rate`, `colsample_bytree`, `colsample_bylevel`, `colsample_bynode` is set to 0.1, 0.3, 0.5, 0.3 respectively.

Using these parameters, we build the tree and use the high-level jet observables as input features. The observables m_{jet} and τ_{NN-1}^β have been calculated on four types of candidates: charged particle tracks (Obs_{trk}), particle-flow jets with radius $R(p_T)$ ($Obs_{rec.}$), particle-flow jets with radius $R(p_T)$ that have been groomed using soft drop algorithm (Obs_{SD}). We have divided them into several sets of input features. These are described as follows:

- Set 1: m_{jet} , m_{jet}^{SD} , $m_{\text{jet}}^{\text{trk}}$, N-Subjettiness ratios τ_{NN-1}^β where $N = 2-6$ and $\beta = 0.5, 1.0, 2.0$, calculated on reclustered jets before applying soft drop (τ_{NN-1}^β), after applying soft drop ($\tau_{NN-1,SD}^\beta$), and on tracks ($\tau_{NN-1,trk}^\beta$).
- Set 2: $m_{\text{jet}}^{\text{trk}}$, $\tau_{NN-1,trk}^\beta$ where $N = 2-6$ and $\beta = 0.5, 1.0, 2.0$.

- Set 3: $m_{\text{jet}}, m_{\text{jet}}^{SD}, m_{\text{jet}}^{\text{trk}}, \tau_{NN-1,\text{trk}}^\beta$ where $N = 2-4$ and $\beta = 0.5, 1.0, 2.0$.
- Set 4: $m_{\text{jet}}, \tau_{NN-1}^\beta$ where $N = 2-6$ and $\beta = 0.5, 1.0, 2.0$.
- Set 5: $m_{\text{jet}}^{SD}, \tau_{NN-1,SD}^\beta$ where $N = 2-6$ and $\beta = 0.5, 1.0, 2.0$.

Set 1 contains all the observables from $Obs_{\text{trk}}, Obs_{\text{rec.}}$, and Obs_{SD} . We include higher N-Subjettiness ratios as well as ratios with varying degrees of β parameter to form a comprehensive set of features. Set 2, 4, and 5 are composed of only $Obs_{\text{trk}}, Obs_{\text{rec.}}$, and Obs_{SD} , respectively. Set 3 is a mixed set of track observables (up to 4-Subjettiness) along with two jet mass observables — m_{jet} before and after soft drop.

Using these, we train the XGBoost. The Receiver-Operating-Characteristic (ROC) curve and the Area-Under-the Curve (AUC) are presented in figure 17. AUC is the measure of how well a classifier can identify positives and negatives in data. A perfect classifier shall have $AUC = 1$. Figure 17a and 17b represent how well the classifier can identify top jets against the background of QCD jets and W jets. Figure 17c and 17d represent how well the classifier can identify W jets against the background of QCD jets and top jets. Set 1, being the most expansive set of features, performs the best in all the cases.

Using solely track based features (set 2) does not prove to be very advantageous, especially when identifying boosted W jets. Set 2 is outperformed by sets 3, 4, and 5, especially for W jet identification. In the multi-class tagger, the advantages of track-based features for top vs. QCD discrimination are offset by their inability to fully capture W jet information. One example is the $m_{\text{jet,trk}}$ variable. While it provides useful separation between top and QCD jets, there is significant overlap between $m_{\text{jet,trk}}$ of W jets and QCD jets.

The charged track multiplicity in W jets is low compared to top jets and QCD jets because of its two-prong decay (top decay has three hard prongs, and QCD jets emit soft radiation) and because W boson is less radiative. At high p_T the tracks from the two decay products overlap. The individual tracks carry more energy than tracks from top decay because there are only two partons to share the energy. The collimation makes it harder to resolve the individual tracks. At 14–16 TeV, much of the information is lost due to overlapping hits in the tracker. This causes the track-based mass and other track-based observables to become less correlated with their particle-flow-based counterparts. On the other hand, less correlation leads to better separation from the top and QCD jets because the track-based and particle-flow-based features are more correlated in the latter case.

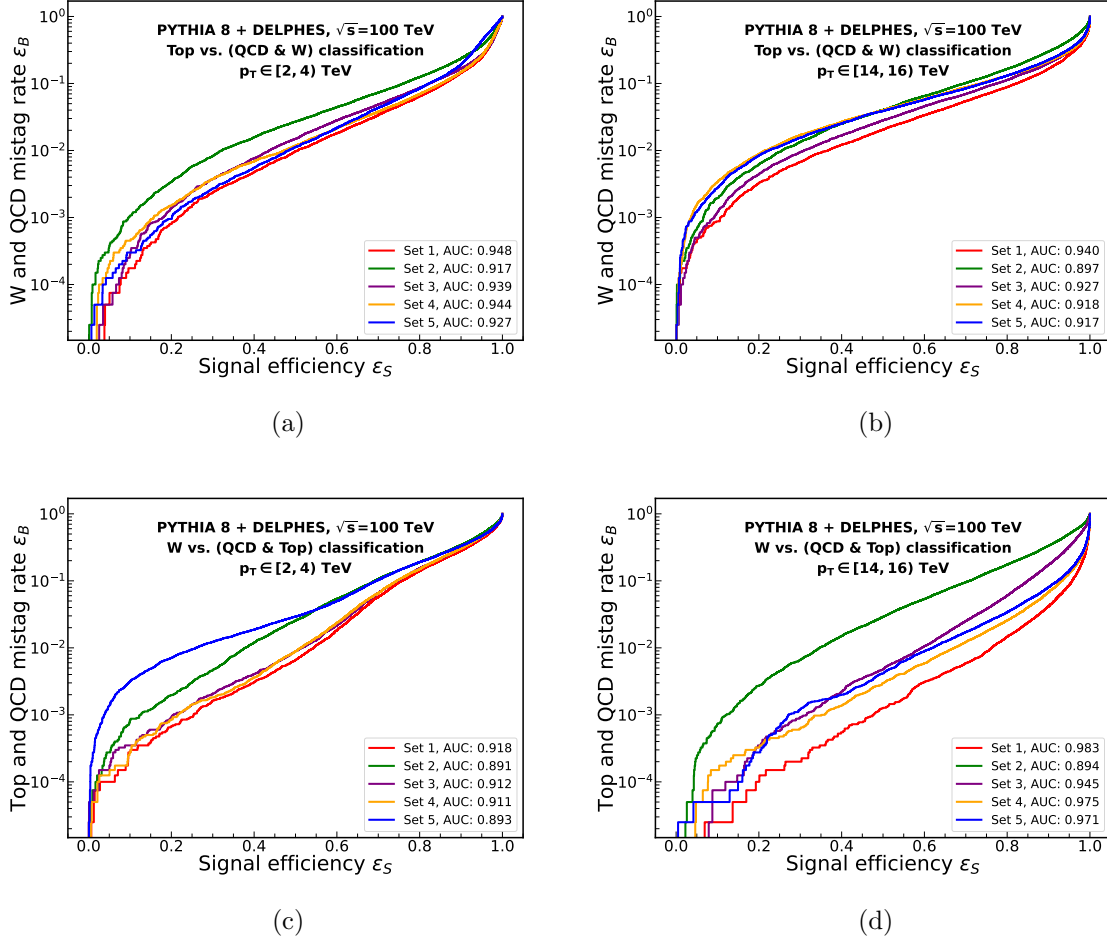


Figure 17: Receiver-Operating-Characteristic (ROC) curve and the Area-Under-the Curve (AUC) for multi-class classification. Figures 17a and 17b show the ROC for top vs. QCD and W classification for 2–4 TeV and 14–16 TeV jets, respectively. Figures 17c and 17d show the ROC for W vs. QCD and top classification for 2–4 TeV and 14–16 TeV jets, respectively.

6.2 Convolutional Neural Networks (CNN)

Convolutional neural networks (CNNs) [85–87] are a powerful deep learning method designed to process visual data. The CNNs accept three-dimensional input images comprising height, width, and depth or channels. The core component of a CNN is the convolutional layer, which utilises two-dimensional kernels or filters to scan the input image, generating a feature map that distills the essential information. This process reduces the spatial dimensions of the data while preserving critical information present in the input image. The network then uses a pooling layer to further down-sample the feature maps by keeping only the most relevant

information. In a typical CNN architecture, multiple convolutional layers and pooling layers are stacked sequentially, allowing the network to learn increasingly complex and abstract feature representations of the input data. The output is then flattened and subsequently fed into a fully connected neural network for the final classification task.

6.2.1 Pre-processing of the images

The p_T, η, ϕ of the constituents of each jet are mapped into a two-dimensional image where each pixel coordinate (x, y) represents a particle's (η, ϕ) , and the pixel intensity is the p_T of the particle. Before mapping, the jet constituents are subject to some pre-processing steps [36]. First, the jet is centered at the p_T weighted centroid of the constituents. This ensures that the hardest subjet is positioned at the center. Then, the constituents are rotated in such a way that the principal axis lies in the vertical direction, and the second hardest subjet is positioned along the positive Y-axis. Lastly, the constituents are reflected such that the third hardest subjet lies in the quadrant. The intensity of the whole image is normalised to 1.

Figure 18 shows the averaged jet images for QCD jets, top jets, and W jets after pre-processing. As the jet constituents were reclustered into a p_T dependent radius, the dimensions of the images are also dependent on p_T . As we go from lower to higher momenta, the three-prong and two-prong features of the core of the top jets and W jets, respectively, shrink and look similar to the QCD jets. The W jets are harder to distinguish from the QCD jets because their two-prong structure appears more similar to that of the QCD jets when highly collimated. However, using the same reclustering radius for all three types of jets leads to some noticeable differences at higher p_T , as the constituents of W jets become less spread out compared to those of QCD and top jets for the same image size.

6.2.2 The network architecture and results

We built the CNN model on two 80 GB NVIDIA A100 GPUs using the `TensorFlow-Keras` framework. Figure 19 shows the layer structure in our model. Filters of shape 2×2 were used for every convolution and pooling operation. To regularise the network and reduce overfitting, a dropout of 0.2 was added after the second Max-Pooling Layer, and a dropout of 0.5 was used before the two-dimensional feature maps were flattened. We have also added early-stopping with patience of 5 epochs. The output, in this case, is categorised into three classes, with a probability of a jet being ‘QCD-like’ (0), ‘top-like’ (1), or ‘W-like’ (2).

With this network, we train the models on $\eta - \phi$ images of particle-flow jets of p_T 2–4 TeV, 4–6 TeV, 6–8 TeV, 8–10 TeV, 10–12 TeV, 12–14 TeV, and 14–16 TeV. The results for the multi-class classification using CNN are represented by the ROC and AUC in Figure 20. Figure 20a shows the ROC for the identification of the top jets, while Figure 20b shows the

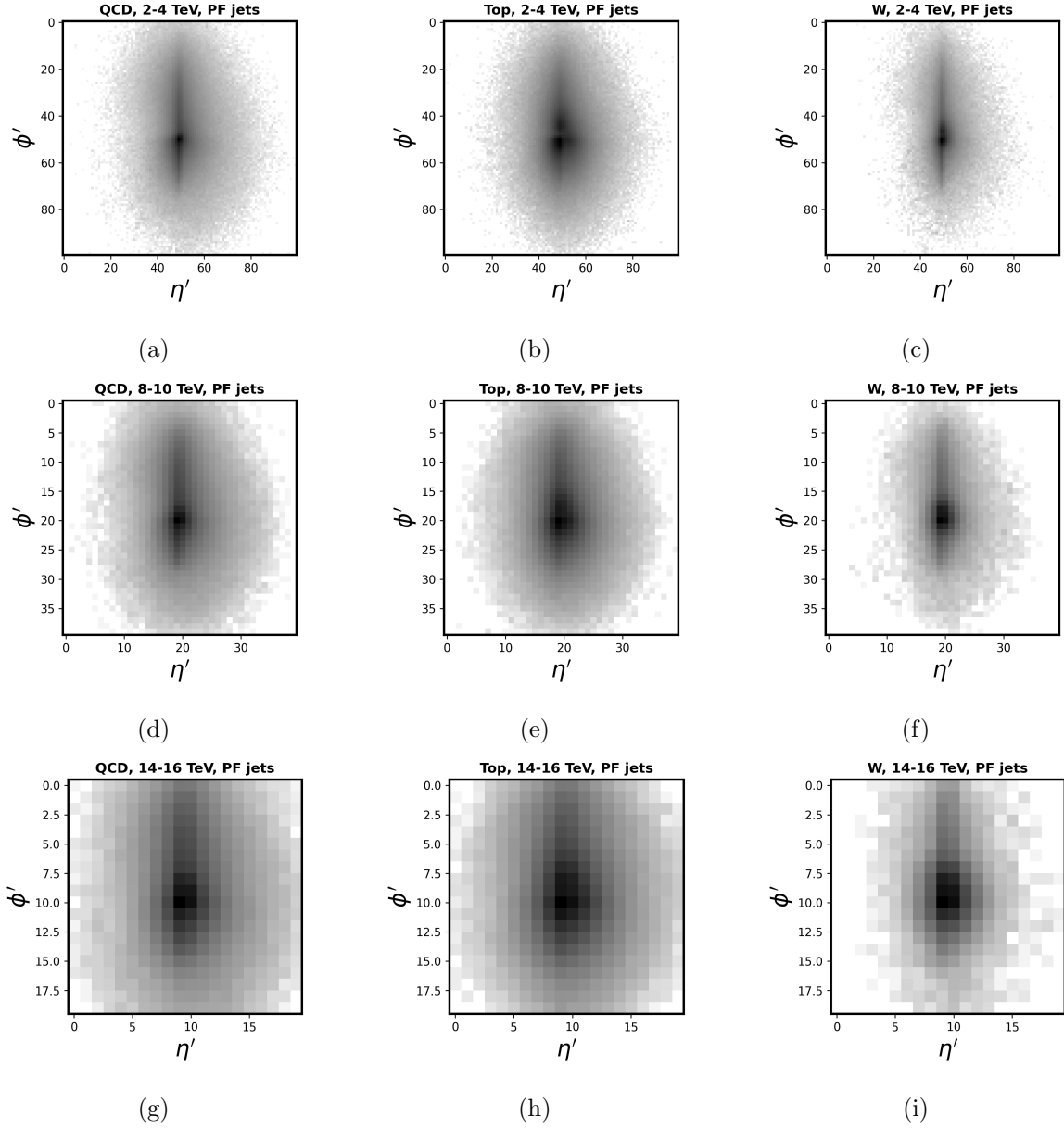


Figure 18: Jet images after averaging over 100,000 events.

ROC for the identification of the W jets. The CNN model identifies top jets better than W jets, as indicated by the respective AUC metrics. At 2–4 TeV, a 60% top tagging efficiency corresponds to a background (including QCD and W) mistagging rate of $\sim 3\%$. The same tagging efficiency for W jets yields a background (QCD and top) mistagging rate of $\sim 6\%$. At 14–16 TeV, a 60% W tagging efficiency results in mistagging rates of $\sim 4\%$ for top jets and 6% for W jets. When the W tagging efficiency exceeds 60%, the background rejection

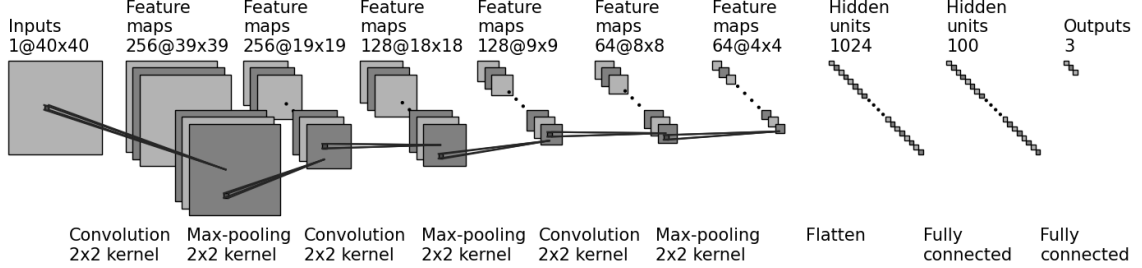


Figure 19: Symbolic representation of the model architecture of CNN used in our analysis. This figure is generated by adapting the code from https://github.com/gwding/draw_convnet.

improves for 14–16 TeV jets compared to 2–4 TeV jets.

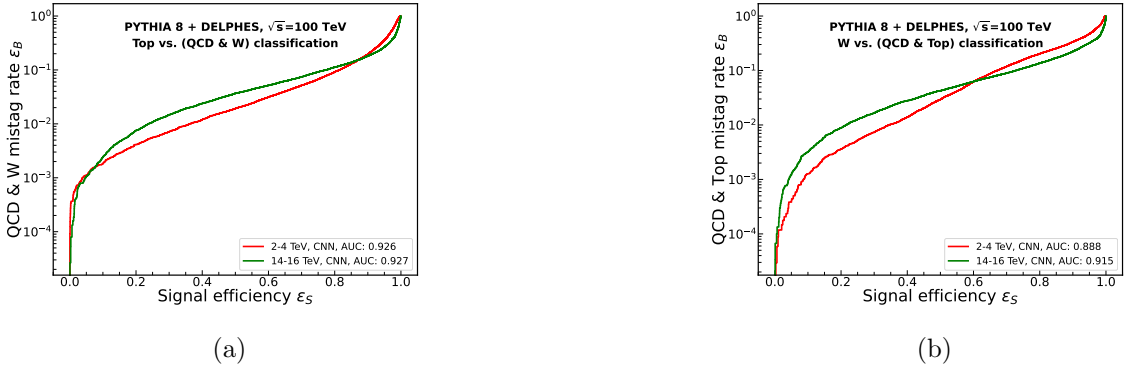


Figure 20: Receiver-Operating-Characteristic (ROC) curve and the Area-Under-the Curve (AUC) for multi-class classification. Figure 20a shows the ROC for top vs. QCD and W classification for 2–4 TeV and 14–16 TeV jets. Figure 20b shows the ROC for W vs. QCD and top classification for 2–4 TeV and 14–16 TeV jets.

We summarise the results for the best performing XGBoost tagger (trained with Obs_{trk} , $Obs_{rec.}$, and Obs_{SD}) and the CNN tagger in Table 3. The feature-based XGBoost tagger outperforms the image-based CNN tagger. Notably, the W jet identification by XGBoost

p_T	CNN results		XGBoost results	
	$\epsilon_S^{top} = \epsilon_S^W = 30\%$			
	ϵ_B^{top}	ϵ_B^W	ϵ_B^{top}	ϵ_B^W
2–4 TeV	.0071	.0073	.0024	.0016
14–16 TeV	.0147	.0165	.0068	.0002
	$\epsilon_S^{top} = \epsilon_S^W = 40\%$			
2–4 TeV	.0119	.0139	.0048	.0031
14–16 TeV	.0238	.0277	.0122	.0006
	$\epsilon_S^{top} = \epsilon_S^W = 60\%$			
2–4 TeV	.0313	.0624	.0180	.0183
14–16 TeV	.0517	.0627	.0335	.0031

Table 3: Background efficiencies of CNN and XGBoost models for fixed signal efficiencies ($\epsilon_S^{top/W}$) of 30%, 40%, and 60%. The mistagging efficiencies for top identification are indicated as ϵ_B^{top} , while the mistagging efficiencies for W identification are indicated as ϵ_B^W .

at high p_T is superior to CNN. Nevertheless, we use both XGBoost and CNN scores in combination to tag the jets in later analyses. We choose a threshold for both scores, which means that if the model output in one of the three classes is greater than the threshold score, the jet gets classified into that class. For example, a cut of 0.7 on the XGBoost score tags 70% of 2–4 TeV top jets, 61% of 2–4 TeV W jets, 65% of 14–16 TeV top jets, and 83% of 14–16 TeV W jets. Across the entire p_T range from 2 TeV to 16 TeV, the background rejection rates vary from 96% to 98%. A similar cut on the CNN score tags 70% of 2–4 TeV top jets, 47% of 2–4 TeV W jets, 55% of 14–16 TeV top jets, and 40% of 14–16 TeV W jets, while the background rejection rates are maintained at 95%–97%.

In this study, the CNN was trained on jet images with the resolution of ECAL. Using track-based images could be a possible way to improve CNN’s performance. Track-based jet images offer higher resolution because the tracking detector’s granularity (0.001 in η - ϕ space) is much finer compared to the calorimeter’s (0.01). However, to maintain the same jet size, the image dimensions increase by a factor of 10, leading to significant computational challenges when used to train the convolutional neural networks (CNNs). Due to hardware limitations, we opted to use calorimeter-based jet images with a more manageable size. A possible future direction would be to explore convolutional neural networks on track-based images and to further optimize the networks.

In the following section, we will apply the developed taggers to explore physics beyond the Standard Model. As previously noted, the example analyses presented herein serve as

illustrations, and the analysis strategy can be further optimized to enhance sensitivity. Our primary objective was to provide a foundation for future investigations rather than achieving the most stringent limits.

7 Analysis of BSM processes with top and W jets in the final state

This section explores the three BSM benchmarks described earlier (Section 2). We begin with the analysis of a neutral gauge boson Z' that decays to two top quarks, then proceed to study the production of a heavy neutral Higgs boson in the W^+W^- decay channel. Lastly, we discuss the associated production of a B' VLQ with a light jet, where the B' decays to a top quark and a W boson.

7.1 Analysis of Z' boson decaying to boosted top jets

With the models trained to efficiently distinguish between boosted top jets, QCD jets, and W jets, we proceed with the reconstruction of the BSM gauge boson, Z' . We have considered the decay $Z' \rightarrow t\bar{t}$ for four benchmarks in our study, with different masses of the Z' boson: $m_{Z'} = 5$ TeV, 10 TeV, 15 TeV, and 20 TeV. At the preselection level, we demand that there must be two jets with a minimum p_T of 2 TeV in each event. We perform reclustering of the jets with radius $R(p_T)$ and apply a softdrop algorithm on the jets. We also consider jets from tracks only. With these jet collections, we construct the observables in Set 1 of Section 6.1 using FASTJET. We also construct jet images from the reclustered jets following the procedure in Section 6.2.1.

Depending on the p_T of the individual jet, we use the XGBoost tagger and the CNN tagger corresponding to the correct p_T range to tag the jet. For example, if, in an event, a Z' boson produces two jets of $p_T = 6.5$ TeV and 3 TeV, the first jet is tested on by the 6-8 TeV ML tagger while the second jet is tested on by the 2-4 TeV ML tagger. The individual taggers return probability scores, which are then used to tag the jet as top jet.

For our analysis, we demand that a jet be tagged as a top jet if both the XGBoost and CNN probability scores of being a top jet are above a defined threshold. We take the two highest p_T jets in each event, and if both the jets are tagged as top jets, we proceed to calculate the invariant mass of the two. Figure 21a shows the invariant mass distribution of the two jets coming from the signal process. The resonance peaks are shifted to lower mass values. This effect is expected and can be corrected by applying jet energy correction factors, which are not used in this study. Instead, we factor in the effect of mass peak shift and use this information to apply proper mass cuts for each benchmark accordingly. We select two

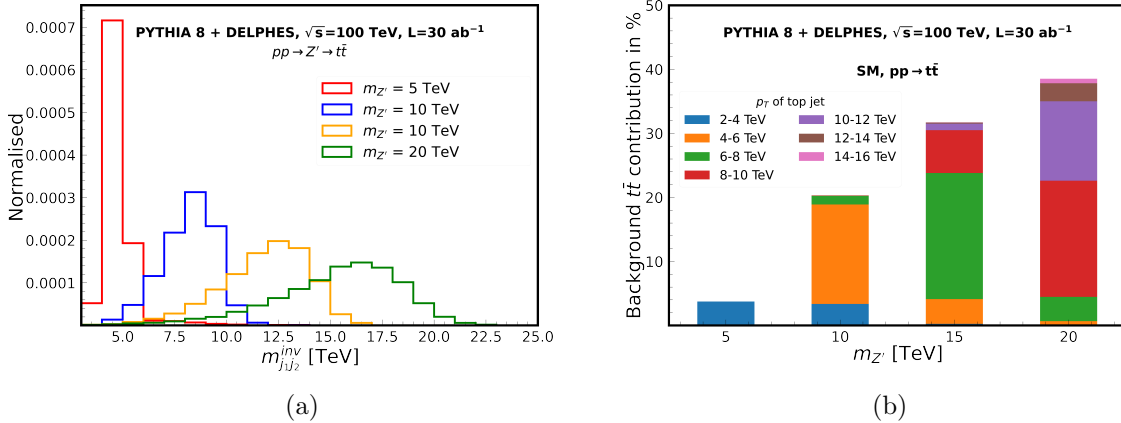


Figure 21: (a) Normalised invariant mass distribution of two hardest jets from $pp \rightarrow Z' \rightarrow t\bar{t}$ process. (b) Contribution of each p_T bin of the dominant $t\bar{t}$ background in % to the four signal benchmarks.

top-tagged jets and require the invariant mass to fall within 4-5 TeV, 8-10 TeV, 12-15 TeV, and 16-20 TeV for the 5 TeV, 10 TeV, 15 TeV, and 20 TeV benchmarks, respectively.

Table 4 shows the background yield (B), and signal efficiency (ϵ_S) for the four benchmarks of Z' boson, at different levels of cuts. We translate the results to model-independent projected upper limits on the Z' boson production and its decay to $t\bar{t}$, $\sigma(pp \rightarrow Z' \rightarrow t\bar{t})_{UL}$,

$$\sigma(pp \rightarrow Z' \rightarrow t\bar{t})_{UL} = \frac{\eta_S \cdot \sqrt{B}}{\epsilon_S \cdot \mathcal{L} \cdot [Br(t \rightarrow bW)]^2 \cdot [Br(W \rightarrow \text{jets})]^2} \quad (7.1)$$

Here η_S represents the standard deviation from the background. In this study, we obtain the projected upper limits at $\eta_S = 2$, representing a 95% confidence interval.

As reported in table 4, after applying the cut on P_{top}^{XGB} for j_1 and j_2 , the QCD background reduces to 0.4% of its original value. The WW reduces to 0.046% of its original value. However, due to the large cross-section of QCD, it still remains ~ 4 times greater than the $t\bar{t}$ background.

For $m_{Z'} = 5$ TeV, the signal efficiency is very low due to the jets failing the $p_T > 2$ TeV criterion. Heavier Z' bosons decay into harder jets, hence we see an increase in the signal efficiency with mass. Jets that are tagged as top jets by one ML model sometimes do not get tagged as top jets by the other ML model. While in 74% of $t\bar{t}$ events (both in the case of background and signal), both top jets get tagged as top jets by CNN and XGBoost, only 46% of QCD events and 43% of WW events that were mistagged as top by XGBoost are also mistagged as top by CNN. This shows that the models correctly learn the features of top

Cuts	Background yield			Signal efficiency
	jj	$t\bar{t}$	W^+W^-	$Z' \rightarrow t\bar{t}$
$m_{Z'} = 5 \text{ TeV}$				
$p_T^{j_1/j_2} > 2 \text{ TeV}, \eta < 2.5$	4.3×10^9	8.5×10^6	5×10^5	18%
$P_{top}^{XGB}(j_1, j_2) > 0.7$	1.7×10^7	4.2×10^6	228	9%
$P_{top}^{CNN}(j_1, j_2) > 0.7$	8.0×10^6	3.1×10^6	99	6%
$4.0 \text{ TeV} < m_{j_1 j_2} < 5.0 \text{ TeV}$	3.6×10^6	9.9×10^5	63	5%
$m_{Z'} = 10 \text{ TeV}$				
$p_T^{j_1/j_2} > 2 \text{ TeV}, \eta < 2.5$	4.3×10^9	8.5×10^6	5×10^5	70%
$P_{top}^{XGB}(j_1, j_2) > 0.7$	1.7×10^7	4.2×10^6	228	32%
$P_{top}^{CNN}(j_1, j_2) > 0.7$	8.0×10^6	3.1×10^6	99	25%
$8.0 \text{ TeV} < m_{j_1 j_2} < 10.0 \text{ TeV}$	1.3×10^5	2.2×10^5	0	16%
$m_{Z'} = 15 \text{ TeV}$				
$p_T^{j_1/j_2} > 2 \text{ TeV}, \eta < 2.5$	4.3×10^9	8.5×10^6	5×10^5	82%
$P_{top}^{XGB}(j_1, j_2) > 0.7$	1.7×10^7	4.2×10^6	228	37%
$P_{top}^{CNN}(j_1, j_2) > 0.7$	8.0×10^6	3.1×10^6	99	29%
$12 \text{ TeV} < m_{j_1 j_2} < 15 \text{ TeV}$	8.8×10^4	2.2×10^4	0	17%
$m_{Z'} = 20 \text{ TeV}$				
$p_T^{j_1/j_2} > 2 \text{ TeV}, \eta < 2.5$	4.3×10^9	8.5×10^6	5×10^5	86%
$P_{top}^{XGB}(j_1, j_2) > 0.7$	1.7×10^7	4.2×10^6	228	38%
$P_{top}^{CNN}(j_1, j_2) > 0.7$	8.0×10^6	3.1×10^6	99	28%
$16 \text{ TeV} < m_{j_1 j_2} < 20 \text{ TeV}$	5100	7999	0	15%

Table 4: Background yield and signal efficiency for the four benchmark mass-points of Z' boson. The $m_{j_1 j_2}$ cuts are different for different values of Z' boson mass.

jets through jet substructure features and jet images. The scores are more correlated for top jets than for QCD. Both signal efficiency and background yield drop after using the cut on the invariant mass. The drop is more for higher resonant masses as the distribution becomes wider.

Figure 21b shows the bin-wise contribution of SM $t\bar{t}$ production, which is one of the major backgrounds, after applying all the cuts. The background to the 15 TeV Z' signal consists mostly of 6-8 TeV jets but also, to some extent, jets with 8-10 TeV p_T . However, the latter shall be suppressed by the lower cross-section. Similarly, 10-12 TeV jets contribute to the background of 20 TeV Z' but are suppressed by the lower cross-section.

Table 5 shows the variation of the signal and background yield, signal efficiency, and

$m_{Z'}$ [TeV]	ML Score	No. of events			Signal Efficiency	$\sigma(pp \rightarrow Z' \rightarrow t\bar{t})_{UL}$ at 95% C.L [fb]
		$pp \rightarrow jj$	$pp \rightarrow t\bar{t}$	$pp \rightarrow W^+W^-$		
5	0.3	2.4×10^7	1.9×10^6	330	0.093	8.0
	0.5	8.5×10^6	1.5×10^6	130	0.075	6.2
	0.7	3.6×10^6	9.9×10^5	63	0.051	6.3
	0.9	0	2.8×10^5	32	0.014	5.7
10	0.3	1.1×10^7	4.0×10^5	190	0.30	1.6
	0.5	2.8×10^6	3.2×10^5	57	0.24	1.1
	0.7	1.3×10^5	2.2×10^5	0	0.16	0.56
	0.9	6091	7.3×10^4	0	0.047	0.88
15	0.3	1.6×10^6	4.8×10^4	119	0.317	0.59
	0.5	4.1×10^5	3.8×10^4	77	0.25	0.39
	0.7	8.8×10^4	2.2×10^4	0	0.17	0.29
	0.9	0	7366	0	0.044	0.28
20	0.3	5.1×10^5	1.1×10^4	15	0.311	0.34
	0.5	9.4×10^4	7294	0.38	0.24	0.20
	0.7	5100	7999	0	0.15	0.11
	0.9	0	1110	0	0.032	0.15

Table 5: Table showing the number of events obtained for background processes, the signal efficiency after applying all cuts, and the upper limit of $pp \rightarrow Z' \rightarrow t\bar{t}$ cross-section at 95% C.L., when the threshold probabilities for XGBoost and CNN taggers are varied from 0.3 to 0.9.

the projected upper limits with the probability threshold of the ML models used for tagging jets as top. Using a higher probability score as the threshold reduces the background, even making it zero, although it comes at a cost of poor signal efficiency. The limits are increasingly stronger as the tagging criteria are tightened. The exception is for the 5 TeV Z' , whose signal efficiency is already low, to begin with, and it drops to 1% with a cut on scores > 0.9 . Even with the background reducing to zero, the low signal efficiency causes the limit to weaken.

7.1.1 Effect of b tagging

Before we proceed to the next analysis of heavy Higgs boson, we would like to mention briefly the effect of b tagging in our analysis. The top jets contain a b jet as one of the three subjets. We have conducted our analysis without employing any b tagging. In the case of top tagging, if the two jets in an event obtained after applying selection cuts were also required to be b-tagged, it would reduce the QCD background further. For FCC-hh, the b tagging efficiency

employed in DELPHES follows the functional form $0.82/(1-p_T/15 \text{ TeV})$ [167] for the jets in our selected phase space ($|\eta| < 2.5$). Table 6 shows the effect of using b tagging as an additional criterion at the selection level.

Effect of b tagging on Background events, with b tagging efficiency = $0.82*(1.0 - p_T/15 \text{ TeV})$		
Selection cuts	$pp \rightarrow jj$	$pp \rightarrow t\bar{t}$
$p_T^{j_1/j_2} > 2 \text{ TeV}, \eta < 2.5$	4.3×10^9	8.5×10^6
$p_T^{j_1/j_2} > 2 \text{ TeV}, \eta < 2.5, \text{btag}(j_1/j_2) = 1$	3.7×10^7	2.5×10^6

Table 6: Effect of b tagging on the two hardest jets at the selection level for QCD and $t\bar{t}$ backgrounds.

The QCD background efficiency reduces to 0.86% of its original value with the use of the b tagging criterion. However, the question remains how the b tagging performance in the actual FCC-hh experiment will be affected in the case of multi-TeV jets. A study in [178] demonstrated that in the multi-TeV regime, the reconstruction of highly boosted B -hadrons becomes challenging owing to their high displacement and high collimation of decay products. In Figure 22, we have shown the displacement of the B^\pm and D^\pm in the radial direction (dT), with increasing p_T of the top jet. The line in black shows the dimension of the inner tracking layer, which consists of pixel sensors of $25\text{--}33.3 \mu\text{m} \times 50\text{--}400 \mu\text{m}$ and extends in the radial direction up to 200 mm [20].

Boosted hadrons coming from a 500 GeV top are well contained within the inner tracking layer. In contrast, for top quarks with $p_T = 2 \text{ TeV}$, 10 TeV, and 14 TeV, approximately 4%, 26%, and 32% of B^\pm decay outside the pixel tracker. A hit multiplicity approach to b tagging was proposed in Ref. [179] to tackle this challenge for boosted b jets. Using the information from the number of hits in each detector layer improved the b tagging in multi-TeV jets. Further studies could explore the effectiveness of this technique in improving b tagging for high- p_T top jets.

7.2 Analysis of neutral heavy Higgs boson decaying to boosted W jets

We consider the production of a heavy Higgs boson that decays to the SM W bosons: $pp \rightarrow H \rightarrow W^+W^-$. We consider the hadronic decay mode of the two W bosons. The final state thus consists of two highly boosted W jets. We consider four different masses of the heavy neutral Higgs to be 5 TeV, 10 TeV, 15 TeV, and 20 TeV. Depending on the mass, the W jets will carry a few TeV of energy. The SM background consists of QCD dijet production and

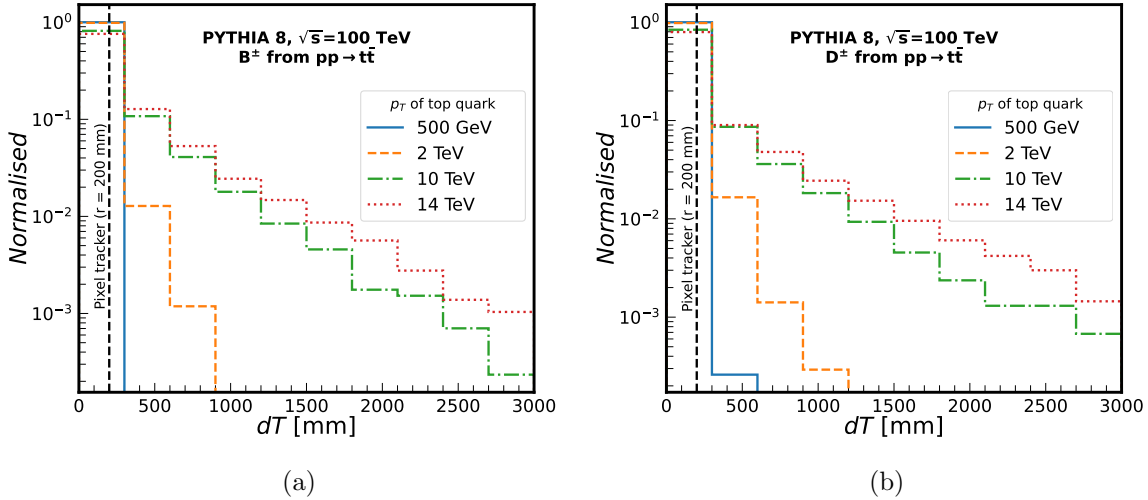


Figure 22: (a) Normalised distribution of displacement (dT) of boosted B^\pm hadron (*left*) and D^\pm hadron (*right*) from the decay of 500 GeV, 2 TeV, 10 TeV, and 14 TeV top quark. The dashed line in black represents the dimension of the inner tracking layer of the FCC-hh detector.

the SM production of WW ¹. Additionally, top jets, which can be misidentified as W jets, are included as part of the background for the $H \rightarrow WW$ process.

Similar to the Z' analysis, we employ multi-class classification using XGBoost and CNN taggers. Both the XGBoost and CNN taggers are trained to classify jets of seven different p_T ranges into three distinct categories. The choice of model is determined by the p_T of the jets. Jet classification is achieved by setting a threshold on the scores produced by the models. Specifically, a jet is tagged as a W jet if its score exceeds the chosen threshold. For each event, we require the presence of two such W jets. Using this criterion, we calculate the signal and background efficiencies. Table 7 summarises the results for all benchmarks with a threshold of 0.7 for both XGBoost and CNN scores. The cuts on the invariant mass of the two jets tagged as W are specific to the signal benchmark.

After all cuts, the QCD background is zero for $m_H = 5$ TeV and $m_H = 10$ TeV, as seen in Table 7. However, for $m_H = 15$ TeV, two QCD Monte Carlo events survived, which, after accounting for cross-section and integrated luminosity, shows up as 132188 events. The QCD cross-section is so high that it is impossible, even for large-scale experimental collaborations, to generate a sufficient number of QCD events comparable to its cross-section and the inte-

¹There are other backgrounds like SM production of $W + \text{jets}$, WZ , ZZ , and tW . We have not included them in this study.

Cuts	Background yield at 30 ab ⁻¹			Signal efficiency
	jj	$t\bar{t}$	W^+W^-	$H \rightarrow W^+W^-$
$m_H = 5 \text{ TeV}$				
$p_T^{j_1/j_2} > 2 \text{ TeV}, \eta < 2.5$	4.3×10^9	8.5×10^6	5×10^5	32%
$P_W^{XGB}(j_1, j_2) > 0.7$	4.5×10^6	1781	1.7×10^5	18%
$P_W^{CNN}(j_1, j_2) > 0.7$	1.4×10^5	0.56	8.0×10^4	5%
$4.0 \text{ TeV} < m_{j_1 j_2} < 5.0 \text{ TeV}$	0	0	4057	3%
$m_H = 10 \text{ TeV}$				
$p_T^{j_1/j_2} > 2 \text{ TeV}, \eta < 2.5$	4.3×10^9	8.5×10^6	5×10^5	74%
$P_W^{XGB}(j_1, j_2) > 0.7$	4.5×10^6	1781	1.7×10^5	52%
$P_W^{CNN}(j_1, j_2) > 0.7$	1.4×10^5	0.56	8.0×10^4	36%
$8.0 \text{ TeV} < m_{j_1 j_2} < 10.0 \text{ TeV}$	0	0	14383	25%
$m_H = 15 \text{ TeV}$				
$p_T^{j_1/j_2} > 2 \text{ TeV}, \eta < 2.5$	4.3×10^9	8.5×10^6	5×10^5	80%
$P_W^{XGB}(j_1, j_2) > 0.7$	4.5×10^6	1781	1.7×10^5	59%
$P_W^{CNN}(j_1, j_2) > 0.7$	1.4×10^5	0.56	8.0×10^4	41%
$12 \text{ TeV} < m_{j_1 j_2} < 15 \text{ TeV}$	132188	0.56	6442	29%
$m_H = 20 \text{ TeV}$				
$p_T^{j_1/j_2} > 2 \text{ TeV}, \eta < 2.5$	4.3×10^9	8.5×10^6	5×10^5	82%
$P_W^{XGB}(j_1, j_2) > 0.7$	4.5×10^6	1781	1.7×10^5	63%
$P_W^{CNN}(j_1, j_2) > 0.7$	1.4×10^5	0.56	8.0×10^4	37%
$16 \text{ TeV} < m_{j_1 j_2} < 20 \text{ TeV}$	7950	0	2926	26%

Table 7: Background yield and signal efficiency for the four benchmark mass-points of the heavy H boson. The cut on $m_{j_1 j_2}$ is different for different resonance masses.

grated luminosity relevant to the physics analysis. As a result, experimental papers on BSM searches always rely on data-driven QCD background, which results in smooth distributions of invariant mass or any other variable of interest, while simulated QCD background often results in spurious spikes in distribution, which is an artefact of insufficient statistics. It's worth noting that eliminating this artefact would require generating an impractically large number of QCD events, far exceeding the scope of this proof-of-concept study.

After both the highest p_T jets are tagged as W , we apply a cut on the invariant mass to select the signal region, following the mass distribution shown in Figure 24a. The dominant background is the QCD because of its large cross-section. The SM WW background is the next most dominant contribution. Figure 24b shows the contribution of various p_T bins to the four benchmarks. Since the SM WW cross-section falls flatly with p_T (see Figure 4), the

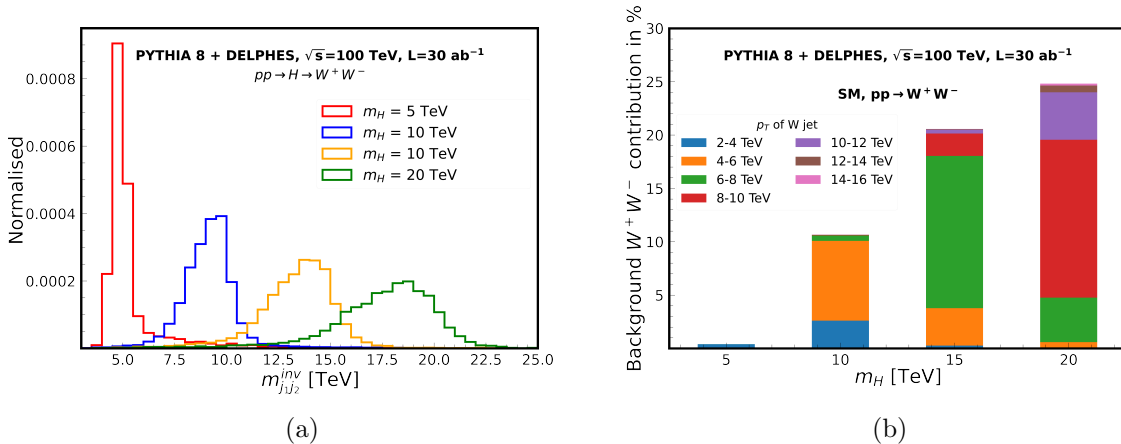


Figure 23: (a) Normalised invariant mass distribution of two hardest jets from $pp \rightarrow H \rightarrow W^+W^-$ process. (b) Contribution of each p_T bin of the dominant W^+W^- background in % to the four signal benchmarks.

number of WW events first increases from $m_H = 5$ TeV to 10 TeV, then decreases with higher masses of H . The $t\bar{t}$ background is greatly reduced by the multi-class taggers and further reduced to zero or less than one event by the invariant mass cut. Using these numbers, we calculate the upper limit on the cross-section $\sigma(pp \rightarrow H \rightarrow W^+W^-)_{UL}$ at 95% C.L. using the formula:

$$\sigma(pp \rightarrow H \rightarrow W^+W^-)_{UL} = \frac{\eta_S \cdot \sqrt{B}}{\epsilon_S \cdot \mathcal{L} \cdot [Br(W \rightarrow \text{jets})]^2} \quad (7.2)$$

Table 8 summarises the background yields and signal efficiency after all cuts, and the upper limit on the cross-section for the process $pp \rightarrow H \rightarrow W^+W^-$ at 95% C.L. for heavy Higgs boson masses of 5 TeV, 10 TeV, 15 TeV, and 20 TeV. Results are shown for varying machine learning (ML) score thresholds ranging from 0.3 to 0.9.

For the background processes, $pp \rightarrow jj$ dominates at lower ML score thresholds but is entirely suppressed at higher thresholds. The $pp \rightarrow W^+W^-$ background decreases as the ML threshold increases, while the $pp \rightarrow t\bar{t}$ background is effectively reduced to zero at all masses and thresholds. Signal efficiency declines with increasing thresholds of ML score, which implies stricter classification criteria.

The upper limit on the cross-section (σ_{UL}) decreases with increasing heavy Higgs mass and tighter classification. For instance, at $m_H = 5$ TeV, the upper limits range from 0.96 fb at a score threshold of 0.3 to 0.78 fb at 0.9. For $m_H = 15$ TeV, the limits range from 0.23 fb

m_H [TeV]	ML Score	No. of events			Signal Efficiency	$\sigma(pp \rightarrow H \rightarrow W^+W^-)_{UL}$ at 95% C.L [fb]
		jj	$t\bar{t}$	W^+W^-		
5	0.3	4.2×10^5	0	2.3×10^4	0.10	0.96
	0.5	0	0	1.1×10^4	0.064	0.24
	0.7	0	0	4057	0.027	0.34
	0.9	0	0	165	0.0024	0.78
10	0.3	6.4×10^5	878	2.8×10^4	0.39	0.30
	0.5	2.0×10^5	9.6	2.2×10^4	0.34	0.20
	0.7	0	0	1.4×10^4	0.25	0.069
	0.9	0	0	4594	0.096	0.10
15	0.3	4.6×10^5	6.8	1.2×10^4	0.43	0.23
	0.5	2.1×10^5	0.56	9512	0.38	0.18
	0.7	1.3×10^5	0.56	6442	0.29	0.18
	0.9	0	0	2035	0.106	0.062
20	0.3	1.4×10^6	0	5062	0.44	0.39
	0.5	1.5×10^5	0	3988	0.38	0.15
	0.7	7950	0	2926	0.26	0.057
	0.9	0	0	632	0.067	0.055

Table 8: Table showing the number of events obtained for background and signal processes, the signal efficiency, and the upper limit of $pp \rightarrow H \rightarrow W^+W^-$ cross-section at 95% C.L., when the threshold probability for XGBoost and CNN taggers is varied from 0.3 to 0.9.

at 0.3 to 0.062 fb at 0.9. At $m_H = 20$ TeV, the lowest upper limit achieved is 0.055 fb at a score threshold of 0.9.

7.3 Analysis of vector-like, heavy B' quark decaying to boosted top jet and W jet

In this subsection, we study the production of a vector-like quark in association with a jet via the process $pp \rightarrow B'j$, and $B' \rightarrow tW$, for $m_{B'} = 5$ TeV and 10 TeV, where both the top quark and the W boson decay hadronically.

The signal topology consists of a top jet and a W jet. The SM background consists of the $pp \rightarrow jj$, $pp \rightarrow t\bar{t}$, and $pp \rightarrow WW$ processes². We demand that the two hardest jets have $p_T > 2$ TeV and $|\eta| < 2.5$. We select the two jets and use the ML taggers to classify them.

²There are other backgrounds like SM production of W + jets, WZ , ZZ , and tW . We have not included them in this study.

Based on the output label with the highest score, we demand that either one of the two jets should be identified as the top jet and the other one should be identified as the W jet. Next, we vary the score threshold for the ‘1’ and ‘2’ classes and tag the jets accordingly.

$m_{B'}$ [TeV]	Threshold score	No. of background events			Signal Efficiency	$\sigma(pp \rightarrow jB' \rightarrow jtW)_{UL}$ at 95% C.L [fb]
		jj	$t\bar{t}$	W^+W^-		
5	0.3	1.2×10^7	6.8×10^4	5476	0.116	4.4
	0.5	3.1×10^6	4.4×10^4	2653	0.088	2.9
	0.7	1.3×10^5	1.4×10^4	1019	0.051	1.1
	0.9	0	181	32	0.010	0.21
10	0.3	5.3×10^6	7736	2436	0.142	2.4
	0.5	3.3×10^6	3805	1330	0.122	2.2
	0.7	1.6×10^6	1556	372	0.081	2.3
	0.9	0	336	9	0.024	0.11

Table 9: Table showing the number of events obtained for background processes, the signal efficiency after all cuts, and the upper limit of $pp \rightarrow jB' \rightarrow jtW$ cross-section at 95% C.L., when the threshold probability for XGBoost and CNN taggers is varied from 0.3 to 0.9.

Table 9 presents the upper limits on the cross-section for the process $pp \rightarrow jB' \rightarrow jtW$ at 95% C.L. for $m_{B'} = 5$ TeV and $m_{B'} = 10$ TeV. The values are computed at different ML score thresholds: 0.3, 0.5, 0.7, and 0.9. The cut on the score is first applied on the XGBoost tagger, followed by the CNN tagger. We apply an invariant mass cut on the signal benchmarks: $4.5 \text{ TeV} < m_{j_1j_2} < 5.5 \text{ TeV}$, and $9 \text{ TeV} < m_{j_1j_2} < 11 \text{ TeV}$ for $m_{B'} = 5$ TeV and 10 TeV respectively.

Higher ML score thresholds result in more stringent upper limits on the cross-section, with lower signal efficiency and yield. The largest yields for the background processes are observed at the lowest threshold (0.3), and they decrease as the threshold increases. For both masses, the upper limit on the cross-section generally decreases as the ML score threshold increases. For example, at $m_{B'} = 5$ TeV, the upper limit on cross-section drops from around 4.4 fb at a threshold of 0.3 to 0.21 fb at 0.9. Similarly, at $m_{B'} = 10$ TeV, the upper limit starts at 2.4 fb for 0.3 and decreases to 0.11 fb for 0.9.

Effect of width

Before we summarise our work, we would like to discuss the effect of the width of the BSM particles on our results. At the 100 TeV collider, particles with masses in the tens of TeV range are expected to have very large widths. This large width makes it difficult to accurately reconstruct the mass of these particles because their decay products are spread

over a wider range, leading to less distinct mass peaks. The decay width (Γ) increases with the mass of the particle, causing the resonance to become broader. So far, we have been using full-width calculations for the signal vs background analysis.

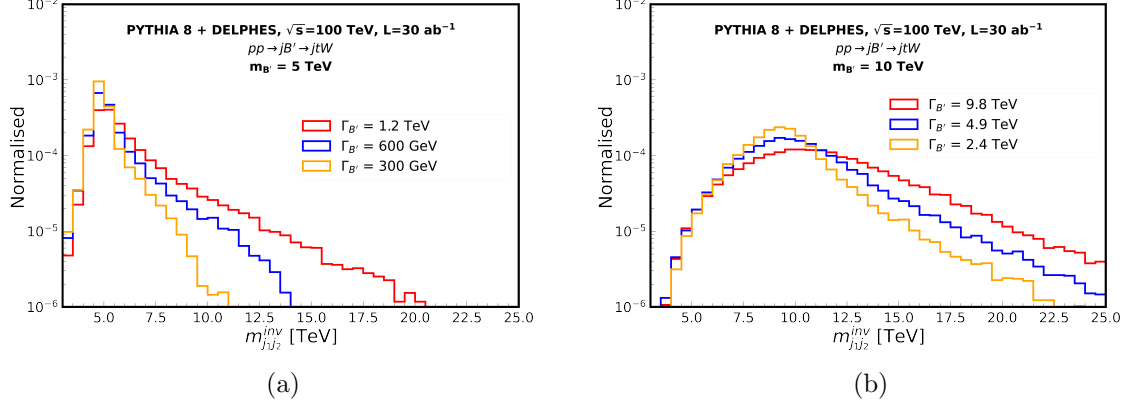


Figure 24: Normalised invariant mass distribution of two hardest jets from $pp \rightarrow jB' \rightarrow jtW$ process for 5 TeV (*left*) and 10 TeV (*right*) B' quark when the width is varied from Γ to $\Gamma/4$.

To demonstrate the effect of width, we show the distributions of $m_{j_1 j_2}^{inv}$ of the signal with the full-width (Γ), half-width ($\Gamma/2$), and quarter-width ($\Gamma/4$) in Figure 24. The distribution peaks more accurately at lower widths. We use the reduced width to obtain signal efficiency and upper limits on cross-section. The results are listed in Table 10. The background yields remain the same.

Using smaller widths, such as half ($\Gamma/2$) or one-fourth ($\Gamma/4$) of the full width, has been shown to improve the results. This is because reducing the width helps reduce the overlap of signal with the background and the spread in the particle’s mass, making it easier to identify and reconstruct the mass of heavy particles.

	ML score			
	0.3	0.5	0.7	0.9
Width: $\Gamma' = \Gamma/2$				
$m_{B'} = 5$ TeV				
Signal efficiency	0.144	0.108	0.061	0.011
$\sigma(pp \rightarrow jB' \rightarrow jtW)_{UL}$ at 95% C.L [fb]	3.5	2.4	0.91	0.195
$m_{B'} = 10$ TeV				
Signal efficiency	0.195	0.167	0.113	0.034
$\sigma(pp \rightarrow jB' \rightarrow jtW)_{UL}$ at 95% C.L [fb]	1.7	1.6	1.6	0.078
Width: $\Gamma' = \Gamma/4$				
$m_{B'} = 5$ TeV				
Signal efficiency	0.163	0.121	0.066	0.010
$\sigma(pp \rightarrow jB' \rightarrow jtW)_{UL}$ at 95% C.L [fb]	3.1	2.1	0.85	0.20
$m_{B'} = 10$ TeV				
Signal efficiency	0.235	0.197	0.132	0.038
$\sigma(pp \rightarrow jB' \rightarrow jtW)_{UL}$ at 95% C.L [fb]	1.4	1.4	1.4	0.071

Table 10: Comparison of signal efficiency, and $\sigma(pp \rightarrow jB' \rightarrow jtW)_{UL}$ at 95% C.L for $m_{B'} = 5$ TeV and $m_{B'} = 10$ TeV with $\Gamma = \Gamma/2$ and $\Gamma = \Gamma/4$.

8 Conclusion

The FCC-hh will provide a unique opportunity to explore the high-energy frontier, enabling direct searches for physics beyond the Standard Model at an unprecedented energy scale of a few tens of TeV. However, this comes with its own set of challenges, like how well the top quark tagging and W boson tagging will work for particles with extremely high transverse momenta. In this paper, we have investigated the identification of boosted W boson jet and boosted top quark jet in the context of three BSM scenarios: heavy neutral gauge boson (Z'), heavy neutral Higgs boson (H), and heavy vector-like quark (B'). Jets emanating from the decay of such high-mass particles are highly energetic up to tens of TeV and, thus, are highly boosted. Very high p_T jets lose energy by radiation, which causes them to mimic jets with lower p_T . Hence, in FCC-hh analyses, it is important to account for the full p_T spectrum of jets.

The kinematic properties, such as jet mass are strongly influenced by the p_T of the jets. For ultra-boosted jets, jet mass and other variables will be significantly modified by the presence of underlying events, particularly initial and final state radiations, proportional to the jet radius. We have demonstrated the importance of using a dynamic jet radius,

dependent on the transverse momentum of jets, to improve the reconstruction of top and W jets. Our results show that this approach can significantly reduce jet contamination and correct various jet properties to some extent. Additionally, we have shown the extent to which improved calorimeter resolution can affect jets with high transverse momentum. Track-based information is more powerful in terms of providing an accurate description of the jets owing to their higher resolution. We perform a brief hypothetical study showing that increasing the angular resolution from 1 mrad to 5 mrad increases the overlap between signal and background distributions of track-based observables, and the effect is more pronounced for $\mathcal{O}(10)$ TeV jets.

Furthermore, we have explored the application of machine learning techniques, including Extreme Gradient Boosted Decision Trees (XGBoost) and convolutional neural networks (CNNs), to distinguish top jets and W jets from QCD jets. Our studies indicate that these techniques can provide high-performance top and W jet tagging, even in the challenging environment of the FCC-hh. The variable-based tagging performs the best when both tower and track-based observables are used as input features. In the case of image-based classification, we have used particle-flow (PF) jet images with ECAL tower resolution.

We have tested the three BSM scenarios with the trained models and calculated the upper limits on cross-sections at 95% C.L. The results depend on the classification threshold. Stricter classification leads to reduced background, however, with also reduced signal efficiency. For an ML score threshold of 0.7, the 95% C.L. upper limits on $\sigma(pp \rightarrow Z' \rightarrow t\bar{t})$ are 6.3 fb, 0.56 fb, 0.29 fb, and 0.11 fb for $m_{Z'} = 5, 10, 15,$ and 20 TeV, respectively. The 95% C.L. upper limits on $\sigma(pp \rightarrow H \rightarrow W^+W^-)$ are 0.34 fb, 0.069 fb, 0.18 fb, and 0.057 fb for $m_H = 5, 10, 15,$ and 20 TeV, respectively. In the case of the VLQ B' , the 95% C.L. upper limits on $\sigma(pp \rightarrow jB' \rightarrow jtW)$ are 1.1 fb and 2.3 fb for $m_{B'} = 5$ TeV and $m_{B'} = 10$ TeV, respectively. Finally, we show that the results also depend on the width of the BSM particle. As the width increases with the mass, reconstructing the particle at the FCC-hh will pose a challenge for multi-TeV resonances.

This study advances our understanding of jets in the exceptionally high-energy regime envisioned for future particle physics experiments. The results presented in this paper demonstrate the feasibility of identifying boosted top and W jets at the FCC-hh and highlight the potential for discovering new physics at a very high mass scale. By developing robust and efficient tagging techniques for hadronically decaying top quarks and W bosons, our work contributes to the ongoing efforts to demonstrate the discovery potential of the FCC-hh. We plan on further optimization of the top/ W jet tagging performance, using more advanced ML techniques in future studies.

9 Acknowledgments

The work of SM is supported by an initiation grant (IITK/PHY/2023282) received from IIT Kanpur. The works of BB, SB, and DC are supported by the Core Research Grants CRG/2021/007579 and CRG/2022/001922 of the Science and Engineering Research Board (SERB), Government of India. BB also acknowledges the MATRICS Grant (MTR/2022/000264) of the Science and Engineering Research Board (SERB), Government of India. DC also acknowledges funding from an initiation grant IITK/PHY/2019413 at IIT Kanpur. CB and BB are grateful to the Center for High Energy Physics, Indian Institute of Science, for the cluster facility.

A Jet after soft drop

We present the distributions of the jet mass (m_{jet}) after applying softdrop algorithm on the reclustered jets. The distributions are shown for two extreme ends of the p_T spectrum, 2–4 TeV jets and 14–16 TeV jets, to highlight the effect of the softdrop with jet p_T . We vary the parameters of softdrop z_{cut} and β defined in Equation 5.6.

Figures 25 and 26 show the m_{jet} distributions of 2–4 TeV jets and 14–16 TeV jets respectively. The z parameter is fixed at 0.05 while β is varied from 0.2 to 2.0. Similar m_{jet} distributions for a fixed $z = 0.08$ are presented in Figures 27 and 28 for 2–4 TeV jets and 14–16 TeV jets respectively. Figures 29 and 30 show the distributions for $z = 0.1$, while Figures 31 and 32 show the distributions for $z = 0.2$.

As z increases, the soft components of the jets are removed more aggressively, hence we see an increase in small peaks at lower m_{jet} values, in top and W jet distributions. Increasing β for a fixed z results in less grooming, since a large β indicates that only wide angle radiations are removed.

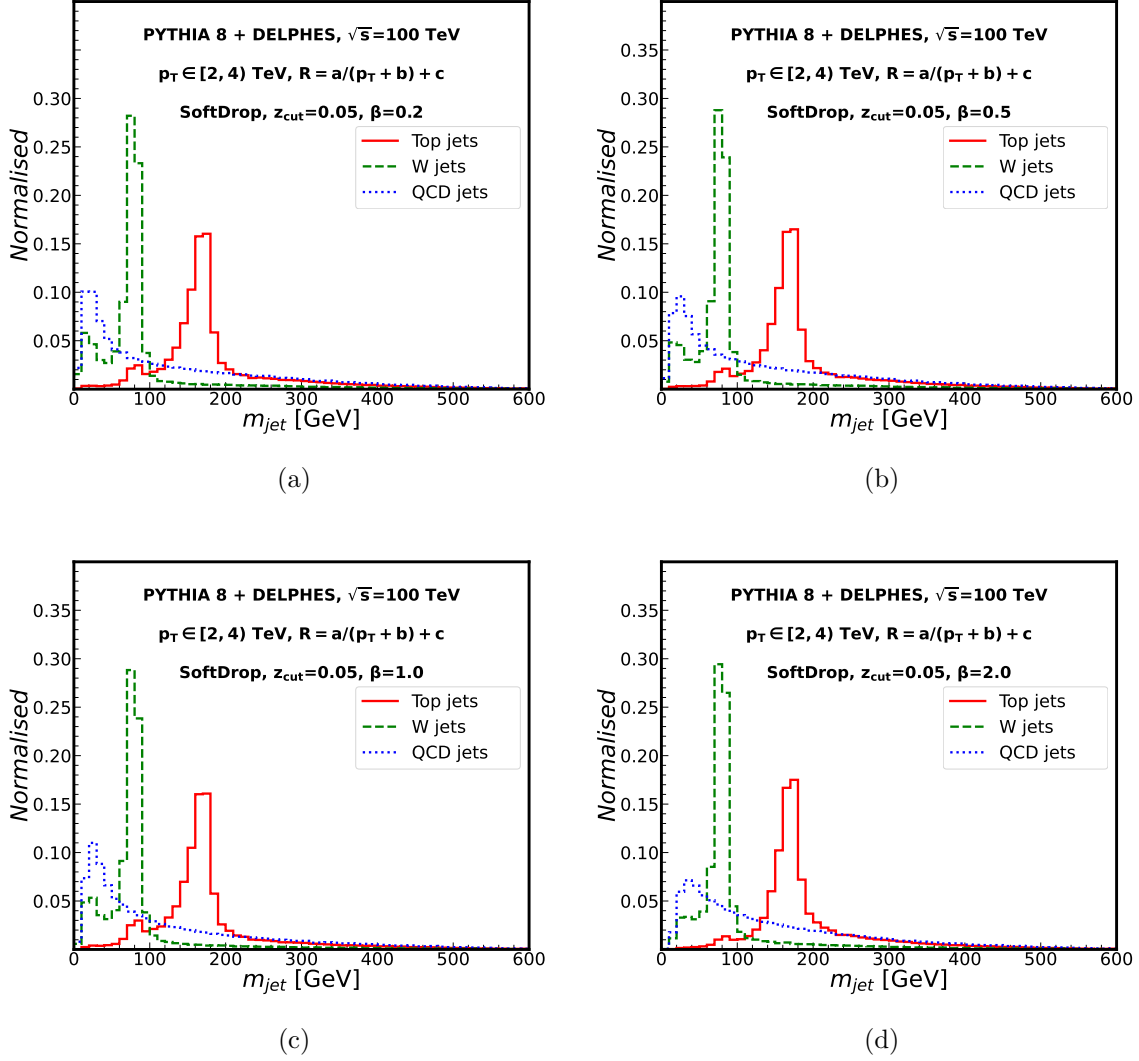


Figure 25: Normalised m_{jet} distribution of 2–4 TeV top jets and QCD jets, after applying softdrop grooming with parameters $z = 0.05$ (*fixed*), and varying $\beta = 0.2, 0.5, 1.0, 2.0$.

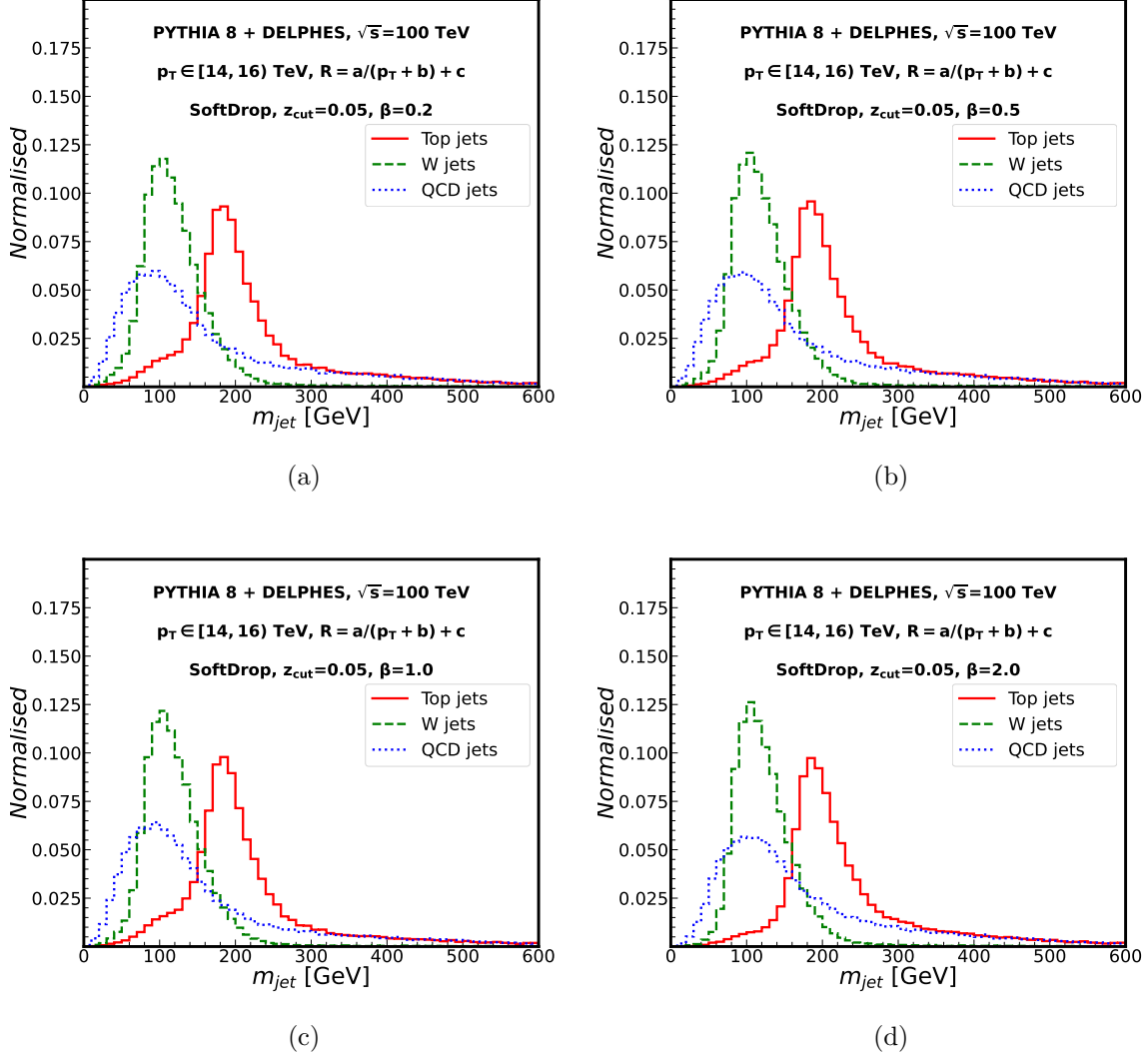


Figure 26: Normalised m_{jet} distribution of 14–16 TeV top jets and QCD jets, after applying softdrop grooming with parameters $z = 0.05$ (*fixed*), and varying $\beta = 0.2, 0.5, 1.0, 2.0$.

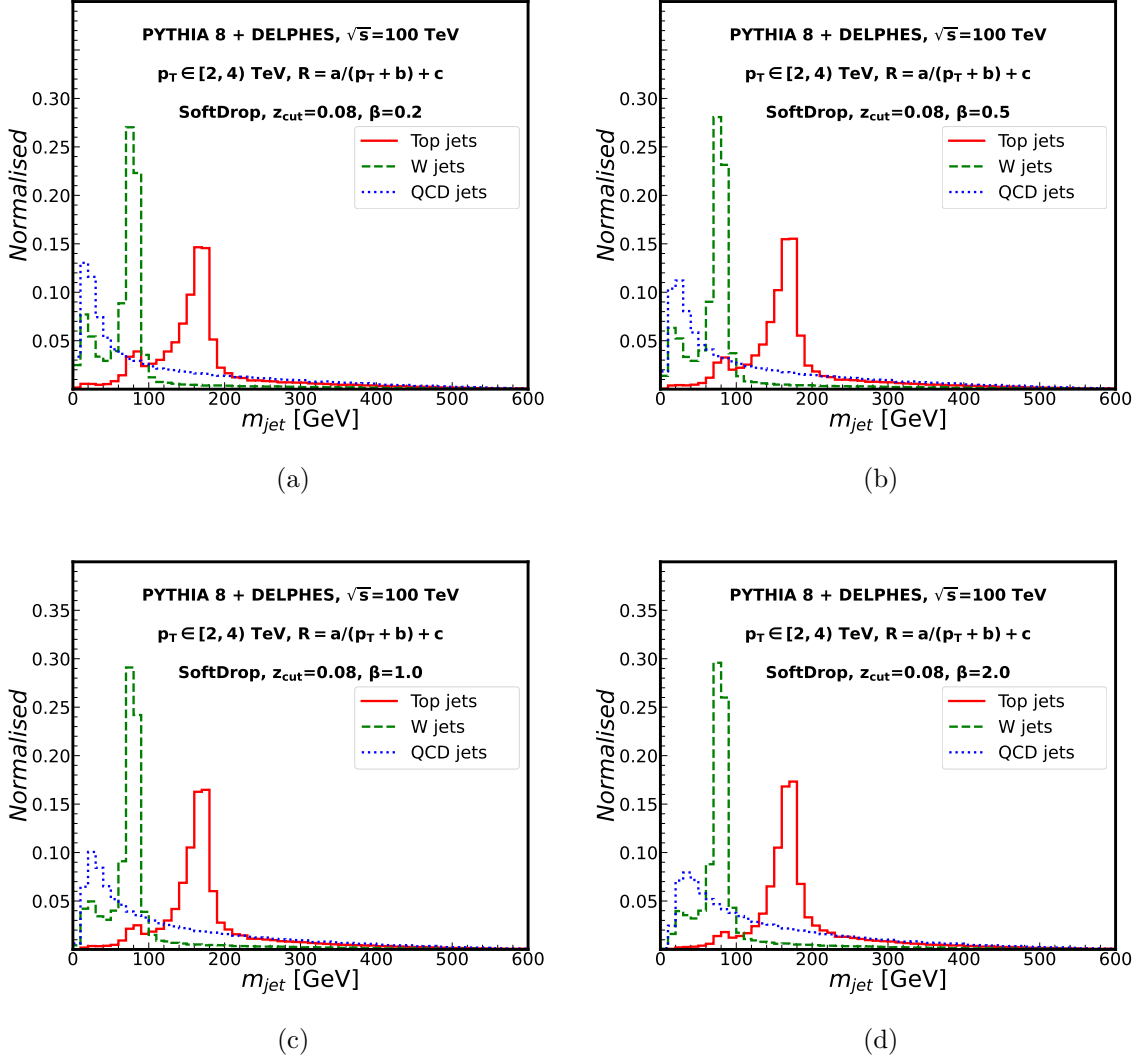


Figure 27: Normalised m_{jet} distribution of 2–4 TeV top jets and QCD jets, after applying softdrop grooming with parameters $z = 0.08$ (*fixed*), and varying $\beta = 0.2, 0.5, 1.0, 2.0$.

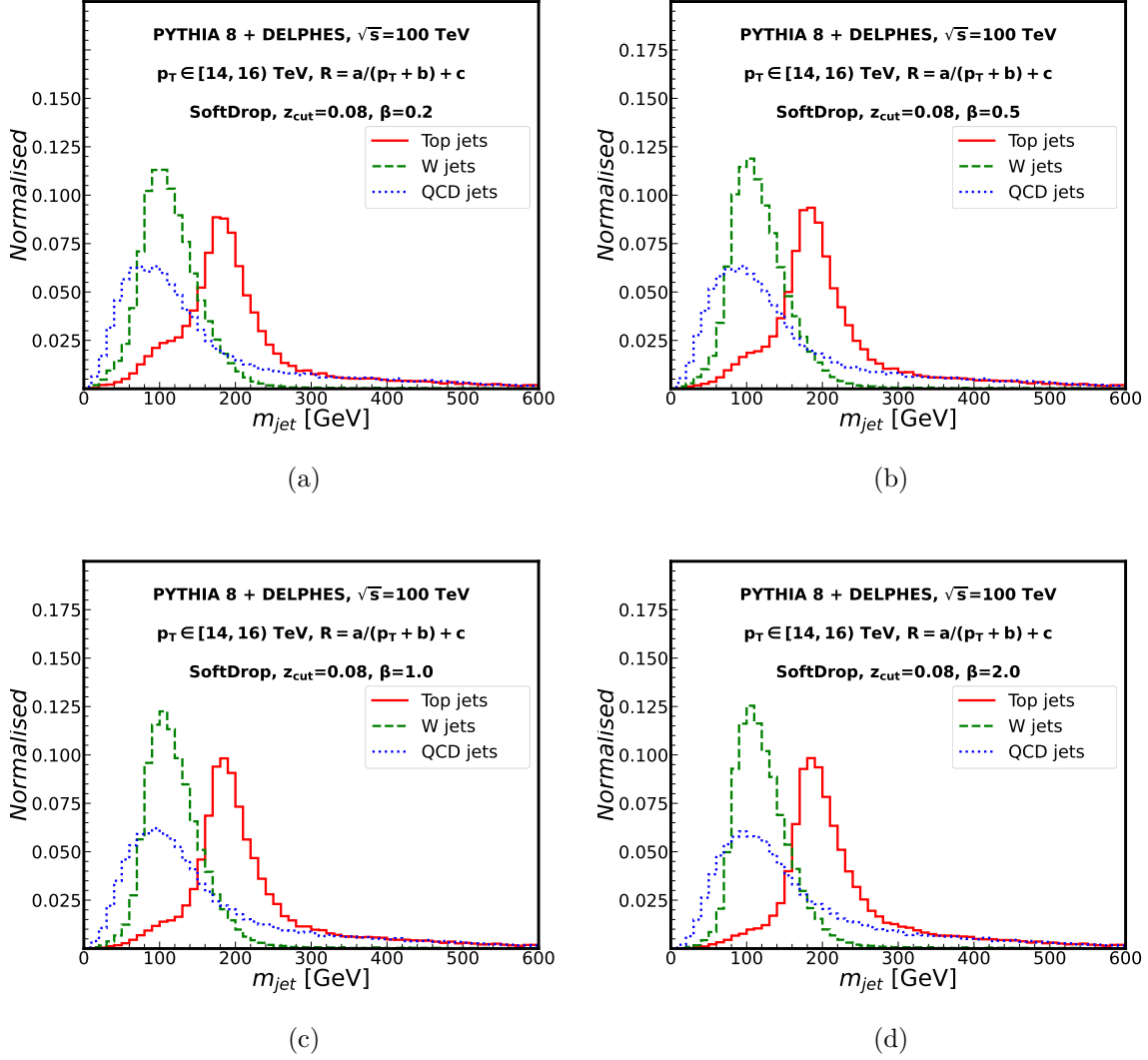


Figure 28: Normalised m_{jet} distribution of 14–16 TeV top jets and QCD jets, after applying softdrop grooming with parameters $z = 0.08$ (*fixed*), and varying $\beta = 0.2, 0.5, 1.0, 2.0$.

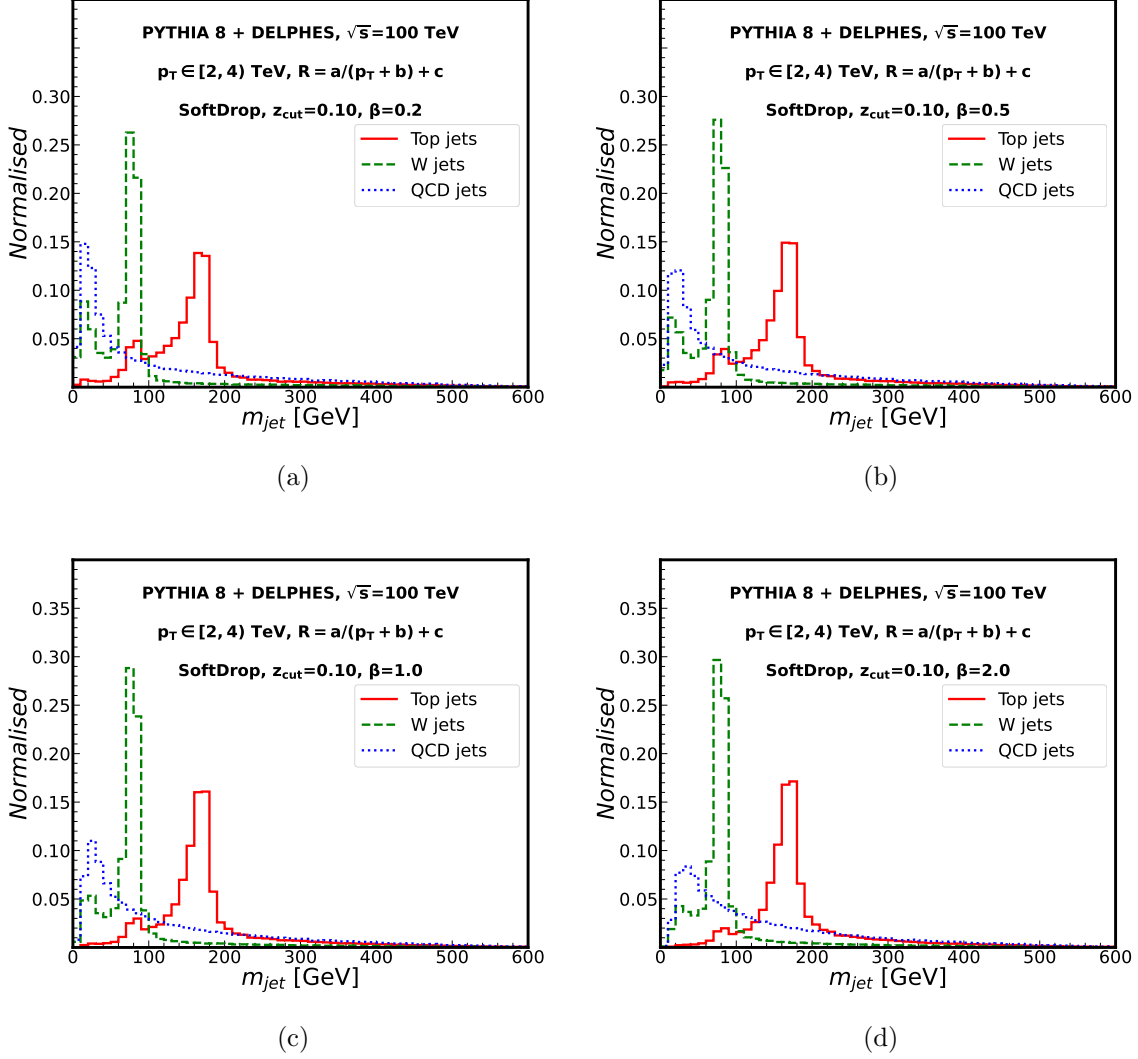


Figure 29: Normalised m_{jet} distribution of 2–4 TeV top jets and QCD jets, after applying softdrop grooming with parameters $z = 0.1$ (*fixed*), and varying $\beta = 0.2, 0.5, 1.0, 2.0$.

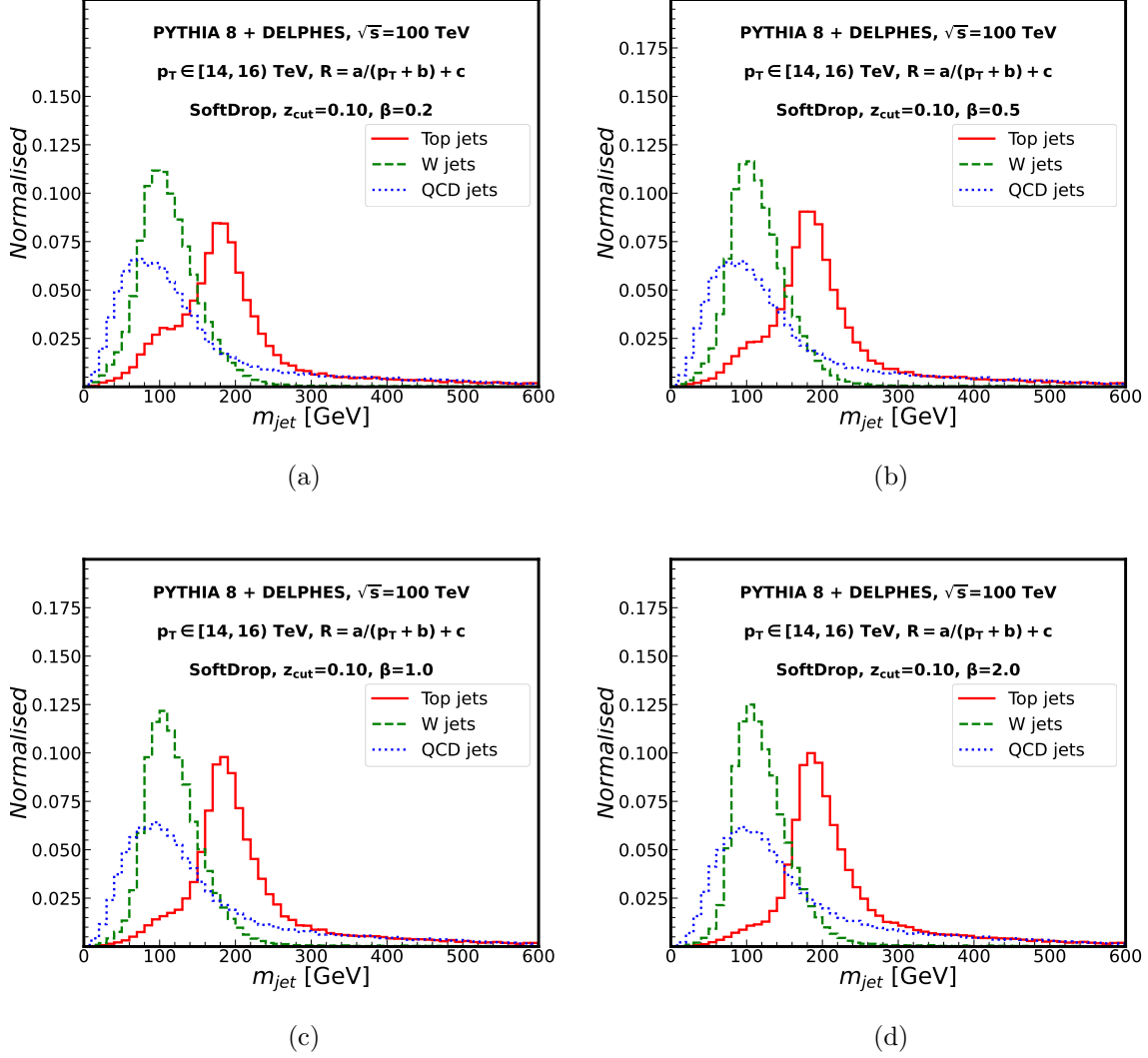


Figure 30: Normalised m_{jet} distribution of 14–16 TeV top jets and QCD jets, after applying softdrop grooming with parameters $z = 0.1$ (*fixed*), and varying $\beta = 0.2, 0.5, 1.0, 2.0$.

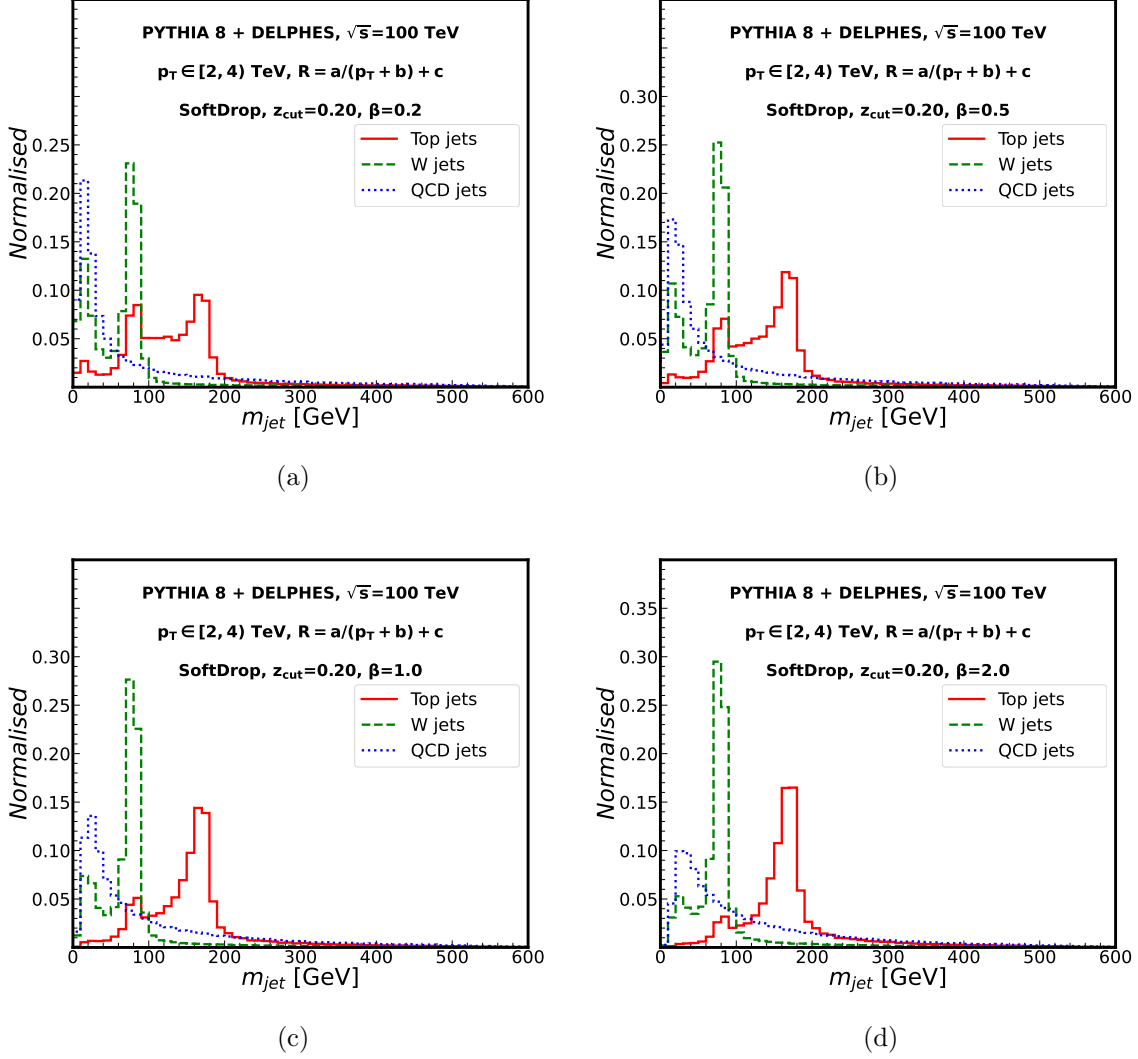


Figure 31: Normalised m_{jet} distribution of 2–4 TeV top jets and QCD jets, after applying softdrop grooming with parameters $z = 0.2$ (*fixed*), and varying $\beta = 0.2, 0.5, 1.0, 2.0$.

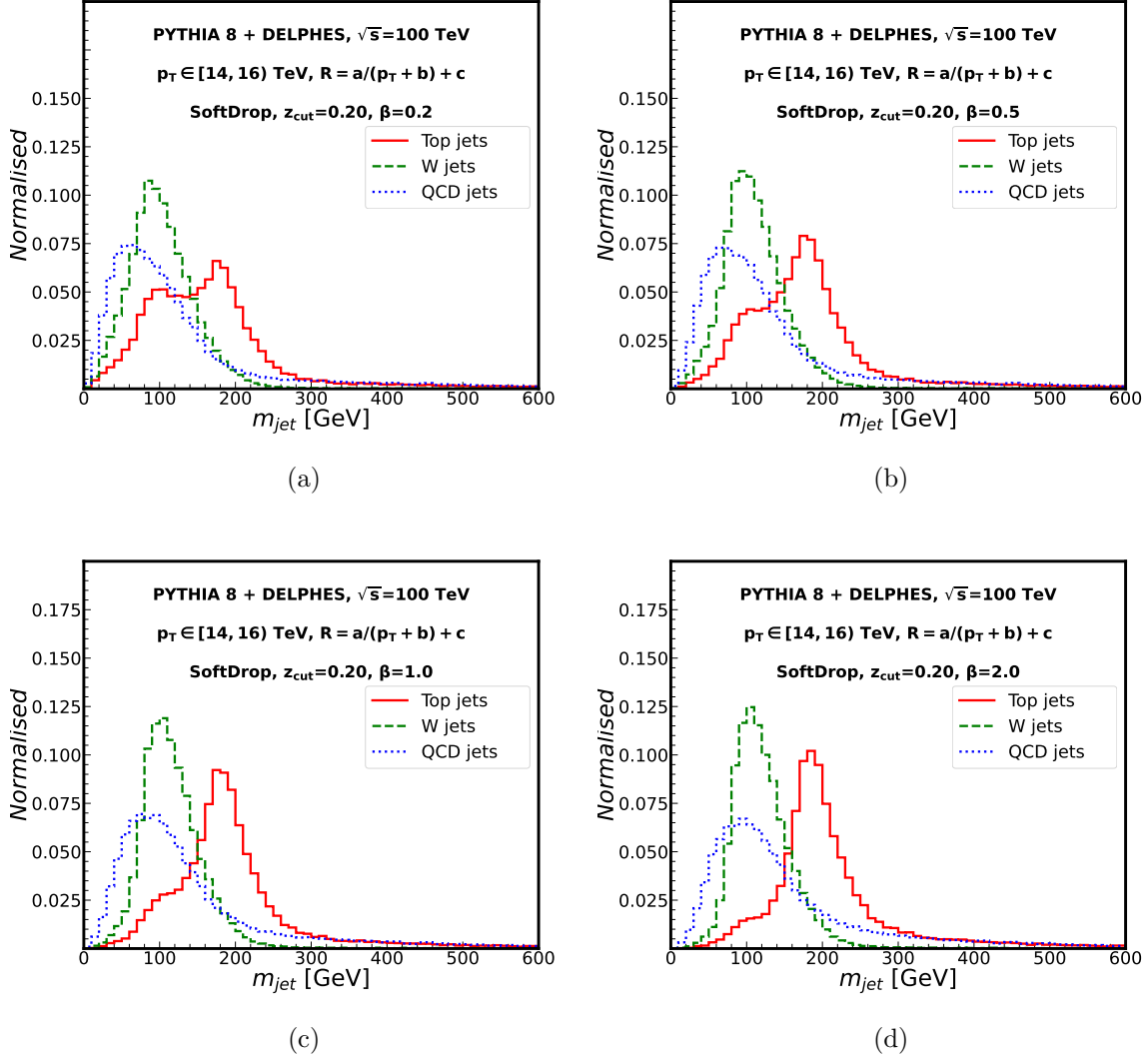


Figure 32: Normalised m_{jet} distribution of 14–16 TeV top jets and QCD jets, after applying softdrop grooming with parameters $z = 0.2$ (*fixed*), and varying $\beta = 0.2, 0.5, 1.0, 2.0$.

References

- [1] ATLAS collaboration, G. Aad et al., *Observation of a new particle in the search for the Standard Model Higgs boson with the ATLAS detector at the LHC*, *Phys. Lett. B* **716** (2012) 1–29, [[1207.7214](#)].
- [2] CMS collaboration, S. Chatrchyan et al., *Observation of a New Boson at a Mass of 125 GeV with the CMS Experiment at the LHC*, *Phys. Lett. B* **716** (2012) 30–61, [[1207.7235](#)].
- [3] G. Heinrich, *Collider Physics at the Precision Frontier*, *Phys. Rept.* **922** (2021) 1–69, [[2009.00516](#)].
- [4] CMS collaboration, A. Tumasyan et al., *Measurement of the Higgs boson width and evidence of its off-shell contributions to ZZ production*, *Nature Phys.* **18** (2022) 1329–1334, [[2202.06923](#)].
- [5] ATLAS COLLABORATION collaboration, *Combined measurement of the higgs boson mass from the $h \rightarrow \gamma\gamma$ and $h \rightarrow zZ^* \rightarrow 4\ell$ decay channels with the atlas detector using $\sqrt{s} = 7, 8,$ and 13 tev pp collision data*, *Phys. Rev. Lett.* **131** (Dec, 2023) 251802.
- [6] ATLAS collaboration, G. Aad et al., *Measurement of the $H \rightarrow \gamma\gamma$ and $H \rightarrow ZZ^* \rightarrow 4\ell$ cross-sections in pp collisions at $\sqrt{s} = 13.6$ TeV with the ATLAS detector*, *Eur. Phys. J. C* **84** (2024) 78, [[2306.11379](#)].
- [7] PARTICLE DATA GROUP collaboration, S. Navas et al., *Review of particle physics*, *Phys. Rev. D* **110** (2024) 030001.
- [8] P. Langacker, *The physics of heavy Z' gauge bosons*, *Rev. Mod. Phys.* **81** (Aug, 2009) 1199–1228.
- [9] L. Basso, A. Belyaev, S. Moretti and C. H. Shepherd-Themistocleous, *Phenomenology of the minimal B-L extension of the Standard model: Z' and neutrinos*, *Phys. Rev. D* **80** (2009) 055030, [[0812.4313](#)].
- [10] S. Amrith, J. M. Butterworth, F. F. Deppisch, W. Liu, A. Varma and D. Yallup, *LHC Constraints on a B – L Gauge Model using Contur*, *JHEP* **05** (2019) 154, [[1811.11452](#)].
- [11] T. D. Lee, *A theory of spontaneous t violation*, *Phys. Rev. D* **8** (Aug, 1973) 1226–1239.
- [12] G. C. Branco, P. M. Ferreira, L. Lavoura, M. N. Rebelo, M. Sher and J. P. Silva, *Theory and phenomenology of two-Higgs-doublet models*, *Phys. Rept.* **516** (2012) 1–102, [[1106.0034](#)].
- [13] D. Chowdhury and O. Eberhardt, *Global fits of the two-loop renormalized Two-Higgs-Doublet model with soft Z_2 breaking*, *JHEP* **11** (2015) 052, [[1503.08216](#)].
- [14] D. Chowdhury and O. Eberhardt, *Update of Global Two-Higgs-Doublet Model Fits*, *JHEP* **05** (2018) 161, [[1711.02095](#)].
- [15] F. Kling, H. Li, A. Pyarelal, H. Song and S. Su, *Exotic Higgs Decays in Type-II 2HDMs at the LHC and Future 100 TeV Hadron Colliders*, *JHEP* **06** (2019) 031, [[1812.01633](#)].
- [16] F. Kling, S. Su and W. Su, *2HDM Neutral Scalars under the LHC*, *JHEP* **06** (2020) 163, [[2004.04172](#)].

- [17] P. Draper, A. Ekstedt and H. E. Haber, *A natural mechanism for approximate Higgs alignment in the 2HDM*, *JHEP* **05** (2021) 235, [[2011.13159](#)].
- [18] L. Wang, J. M. Yang and Y. Zhang, *Two-Higgs-doublet models in light of current experiments: a brief review*, *Commun. Theor. Phys.* **74** (2022) 097202, [[2203.07244](#)].
- [19] M. Mangano, P. Azzi, M. Benedikt, A. Blondel, D. A. Britzger, A. Dainese et al., *FCC Physics Opportunities: Future Circular Collider Conceptual Design Report Volume 1. Future Circular Collider*, Tech. Rep. 6, CERN, Geneva, 2019. [10.1140/epjc/s10052-019-6904-3](#).
- [20] M. Benedikt, M. Capeans Garrido, F. Cerutti, B. Goddard, J. Gutleber, J. M. Jimenez et al., *FCC-hh: The Hadron Collider: Future Circular Collider Conceptual Design Report Volume 3. Future Circular Collider*, tech. rep., CERN, Geneva, 2019. [10.1140/epjst/e2019-900087-0](#).
- [21] A. J. Larkoski, F. Maltoni and M. Selvaggi, *Tracking down hyper-boosted top quarks*, *JHEP* **06** (2015) 032, [[1503.03347](#)].
- [22] J. Bonilla et al., *Jets and Jet Substructure at Future Colliders*, *Front. in Phys.* **10** (2022) 897719, [[2203.07462](#)].
- [23] T. Bandyopadhyay, S. Mukherjee, S. Raychaudhuri and R. Vinze, *Kinematics and Particle Identification at Very High Energy Colliders*, *Springer Proc. Phys.* **304** (2024) 1251–1253.
- [24] C. Yeh, S. Chekanov, A. Kotwal, J. Proudfoot, S. Sen, N. Tran et al., *Studies of granularity of a hadronic calorimeter for tens-of-tev jets at a 100 tev pp collider*, *Journal of Instrumentation* **14** (may, 2019) P05008.
- [25] J. Thaler and K. Van Tilburg, *Identifying Boosted Objects with N-subjettiness*, *JHEP* **03** (2011) 015, [[1011.2268](#)].
- [26] A. J. Larkoski, G. P. Salam and J. Thaler, *Energy Correlation Functions for Jet Substructure*, *JHEP* **06** (2013) 108, [[1305.0007](#)].
- [27] A. J. Larkoski, I. Mould and D. Neill, *Power Counting to Better Jet Observables*, *JHEP* **12** (2014) 009, [[1409.6298](#)].
- [28] A. J. Larkoski, I. Mould and D. Neill, *Building a Better Boosted Top Tagger*, *Phys. Rev. D* **91** (2015) 034035, [[1411.0665](#)].
- [29] A. J. Larkoski, I. Mould and D. Neill, *Analytic Boosted Boson Discrimination*, *JHEP* **05** (2016) 117, [[1507.03018](#)].
- [30] I. Mould, L. Necib and J. Thaler, *New Angles on Energy Correlation Functions*, *JHEP* **12** (2016) 153, [[1609.07483](#)].
- [31] J. Erdmann, S. Guindon, K. Kroeninger, B. Lemmer, O. Nackenhorst, A. Quadt et al., *A likelihood-based reconstruction algorithm for top-quark pairs and the KLFitter framework*, *Nucl. Instrum. Meth. A* **748** (2014) 18–25, [[1312.5595](#)].
- [32] L. G. Almeida, M. Backović, M. Cliche, S. J. Lee and M. Perelstein, *Playing Tag with ANN: Boosted Top Identification with Pattern Recognition*, *JHEP* **07** (2015) 086, [[1501.05968](#)].

- [33] G. Kasieczka, T. Plehn, M. Russell and T. Schell, *Deep-learning Top Taggers or The End of QCD?*, *JHEP* **05** (2017) 006, [[1701.08784](#)].
- [34] M. Erdmann, B. Fischer and M. Rieger, *Jet-parton assignment in $t\bar{t}H$ events using deep learning*, *JINST* **12** (2017) P08020, [[1706.01117](#)].
- [35] A. Butter, G. Kasieczka, T. Plehn and M. Russell, *Deep-learned Top Tagging with a Lorentz Layer*, *SciPost Phys.* **5** (2018) 028, [[1707.08966](#)].
- [36] S. Macaluso and D. Shih, *Pulling Out All the Tops with Computer Vision and Deep Learning*, *JHEP* **10** (2018) 121, [[1803.00107](#)].
- [37] L. Moore, K. Nordström, S. Varma and M. Fairbairn, *Reports of My Demise Are Greatly Exaggerated: N -subjettiness Taggers Take On Jet Images*, *SciPost Phys.* **7** (2019) 036, [[1807.04769](#)].
- [38] H. Qu and L. Gouskos, *ParticleNet: Jet Tagging via Particle Clouds*, *Phys. Rev. D* **101** (2020) 056019, [[1902.08570](#)].
- [39] A. Butter et al., *The Machine Learning landscape of top taggers*, *SciPost Phys.* **7** (2019) 014, [[1902.09914](#)].
- [40] T. S. Roy and A. H. Vijay, *A robust anomaly finder based on autoencoders*, [1903.02032](#).
- [41] S. Diefenbacher, H. Frost, G. Kasieczka, T. Plehn and J. M. Thompson, *CapsNets Continuing the Convolutional Quest*, *SciPost Phys.* **8** (2020) 023, [[1906.11265](#)].
- [42] A. Chakraborty, S. H. Lim, M. M. Nojiri and M. Takeuchi, *Neural Network-based Top Tagger with Two-Point Energy Correlations and Geometry of Soft Emissions*, *JHEP* **07** (2020) 111, [[2003.11787](#)].
- [43] S. Bhattacharya, M. Guchait and A. H. Vijay, *Boosted top quark tagging and polarization measurement using machine learning*, *Phys. Rev. D* **105** (2022) 042005, [[2010.11778](#)].
- [44] A. Shmakov, M. J. Fenton, T.-W. Ho, S.-C. Hsu, D. Whiteson and P. Baldi, *SPANet: Generalized permutationless set assignment for particle physics using symmetry preserving attention*, *SciPost Phys.* **12** (2022) 178, [[2106.03898](#)].
- [45] S. H. Lim and M. M. Nojiri, *Morphology for jet classification*, *Phys. Rev. D* **105** (2022) 014004, [[2010.13469](#)].
- [46] F. A. Dreyer and H. Qu, *Jet tagging in the Lund plane with graph networks*, *JHEP* **03** (2021) 052, [[2012.08526](#)].
- [47] J. A. Aguilar-Saavedra, *Pulling the Higgs and top needles from the jet stack with feature extended supervised tagging*, *Eur. Phys. J. C* **81** (2021) 734, [[2102.01667](#)].
- [48] M. Andrews et al., *End-to-end jet classification of boosted top quarks with the CMS open data*, *EPJ Web Conf.* **251** (2021) 04030, [[2104.14659](#)].
- [49] H. Qu, C. Li and S. Qian, *Particle Transformer for Jet Tagging*, [2202.03772](#).

- [50] F. A. Dreyer, R. Grabarczyk and P. F. Monni, *Leveraging universality of jet taggers through transfer learning*, *Eur. Phys. J. C* **82** (2022) 564, [[2203.06210](#)].
- [51] I. Ahmed, A. Zada, M. Waqas and M. U. Ashraf, *Application of deep learning in top pair and single top quark production at the LHC*, [2203.12871](#).
- [52] J. M. Munoz, I. Batatia and C. Ortner, *BIP: Boost Invariant Polynomials for Efficient Jet Tagging*, [2207.08272](#).
- [53] S. K. Choi, J. Li, C. Zhang and R. Zhang, *Automatic detection of boosted Higgs boson and top quark jets in an event image*, *Phys. Rev. D* **108** (2023) 116002, [[2302.13460](#)].
- [54] M. He and D. Wang, *Quark/gluon discrimination and top tagging with dual attention transformer*, *Eur. Phys. J. C* **83** (2023) 1116, [[2307.04723](#)].
- [55] A. Bogatskiy, T. Hoffman, D. W. Miller, J. T. Offermann and X. Liu, *Explainable Equivariant Neural Networks for Particle Physics: PELICAN*, [2307.16506](#).
- [56] W. Shen, D. Wang and J. M. Yang, *Hierarchical high-point Energy Flow Network for jet tagging*, *JHEP* **09** (2023) 135, [[2308.08300](#)].
- [57] B. Işıldak, A. Hayreter, M. Hüdaverdi, F. Ilgin, S. Salva, E. Şimşek et al., *Investigating the Violation of Charge-parity Symmetry Through Top-quark ChromoElectric Dipole Moments by Using Machine Learning Techniques*, *Acta Phys. Polon. B* **54** (2023) 5–A4, [[2306.11683](#)].
- [58] R. Sahu and K. Ghosh, *ML-Based Top Taggers: Performance, Uncertainty and Impact of Tower & Tracker Data Integration*, [2309.01568](#).
- [59] P. Baroň, J. Kvita, R. Přívara, J. Tomeček and R. Vodák, *Application of Machine Learning Based Top Quark and W Jet Tagging to Hadronic Four-Top Final States Induced by SM as well as BSM Processes*, in *16th International Workshop on Top Quark Physics*, 10, 2023. [2310.13009](#).
- [60] A. Bogatskiy, T. Hoffman and J. T. Offermann, *19 Parameters Is All You Need: Tiny Neural Networks for Particle Physics*, in *37th Conference on Neural Information Processing Systems*, 10, 2023. [2310.16121](#).
- [61] R. Liu, A. Gandrakota, J. Ngadiuba, M. Spiropulu and J.-R. Vlimant, *Efficient and Robust Jet Tagging at the LHC with Knowledge Distillation*, in *37th Conference on Neural Information Processing Systems*, 11, 2023. [2311.14160](#).
- [62] J. Batson and Y. Kahn, *Scaling Laws in Jet Classification*, [2312.02264](#).
- [63] A. Furuichi, S. H. Lim and M. M. Nojiri, *Jet Classification Using High-Level Features from Anatomy of Top Jets*, [2312.11760](#).
- [64] V. S. Ngairangbam and M. Spannowsky, *Interpretable deep learning models for the inference and classification of LHC data*, [2312.12330](#).
- [65] ATLAS collaboration, G. Aad et al., *Search for $t\bar{t}$ resonances in fully hadronic final states in pp collisions at $\sqrt{s} = 13$ TeV with the ATLAS detector*, *JHEP* **10** (2020) 061, [[2005.05138](#)].

- [66] ATLAS collaboration, *Boosted hadronic vector boson and top quark tagging with ATLAS using Run 2 data*, tech. rep., CERN, Geneva, 2020.
- [67] ATLAS collaboration, *Constituent-Based Top-Quark Tagging with the ATLAS Detector*, tech. rep., CERN, Geneva, 2022.
- [68] CMS collaboration, S. Chatrchyan et al., *Search for Anomalous $t\bar{t}$ Production in the Highly-Boosted All-Hadronic Final State*, *JHEP* **09** (2012) 029, [[1204.2488](#)].
- [69] CMS collaboration, A. M. Sirunyan et al., *Search for $t\bar{t}$ resonances in highly boosted lepton+jets and fully hadronic final states in proton-proton collisions at $\sqrt{s} = 13$ TeV*, *JHEP* **07** (2017) 001, [[1704.03366](#)].
- [70] CMS collaboration, A. M. Sirunyan et al., *Search for top squark production in fully-hadronic final states in proton-proton collisions at $\sqrt{s} = 13$ TeV*, *Phys. Rev. D* **104** (2021) 052001, [[2103.01290](#)].
- [71] P. Keicher, *Machine Learning in Top Physics in the ATLAS and CMS Collaborations*, in *15th International Workshop on Top Quark Physics*, 1, 2023. [2301.09534](#).
- [72] B. Bhattacharjee, C. Bose, A. Chakraborty and R. Sengupta, *Boosted top tagging and its interpretation using Shapley values*, *Eur. Phys. J. Plus* **139** (2024) 1131, [[2212.11606](#)].
- [73] C. Bose, A. Chakraborty, S. Chowdhury and S. Dutta, *Interplay of traditional methods and machine learning algorithms for tagging boosted objects*, *Eur. Phys. J. ST* **233** (2024) 2531–2558, [[2408.01138](#)].
- [74] R. Baruah, A. Choudhury, K. Ghosh, S. Mondal and R. Sahu, *Probing sub-TeV Higgsinos aided by a ML-based top tagger in the context of Trilinear RPV SUSY*, [2412.11862](#).
- [75] R. K. Barman and S. Biswas, *Top-philic machine learning*, *Eur. Phys. J. ST* **233** (2024) 2497–2530, [[2407.00183](#)].
- [76] K. Fraser, *Probing Undiscovered Particles with Theory and Data-Driven Tools*. PhD thesis, Harvard U. (main), Harvard U., 4, 2024.
- [77] S. Mondal and L. Mastrolorenzo, *Machine learning in high energy physics: a review of heavy-flavor jet tagging at the LHC*, *Eur. Phys. J. ST* **233** (2024) 2657–2686, [[2404.01071](#)].
- [78] S. Chowdhury, A. Chakraborty and S. Dutta, *Boosted Top Tagging through Flavour-violating interactions at the LHC*, [2310.10763](#).
- [79] A. Choudhury, A. Mondal, S. Mondal and S. Sarkar, *Improving sensitivity of trilinear R-parity violating SUSY searches using machine learning at the LHC*, *Phys. Rev. D* **109** (2024) 035001, [[2308.02697](#)].
- [80] A. Chakraborty, A. De, R. M. Godbole and M. Guchait, *Tagging a boosted top quark with a τ final state*, *Phys. Rev. D* **108** (2023) 035011, [[2304.12846](#)].
- [81] A. Chakraborty, S. Dasmahapatra, H. Day-Hall, B. Ford, S. Jain and S. Moretti, *Fat b-jet analyses using old and new clustering algorithms in new Higgs boson searches at the LHC*, *Eur. Phys. J. C* **83** (2023) 347, [[2303.05189](#)].

- [82] E. Alvarez, M. Szewc, A. Szynekman, S. A. Tanco and T. Tarutina, *Exploring unsupervised top tagging using Bayesian inference*, *SciPost Phys. Core* **6** (2023) 046, [[2212.13583](#)].
- [83] D. Alvestad, N. Fomin, J. Kersten, S. Maeland and I. Strümke, *Beyond Cuts in Small Signal Scenarios – Enhanced Sneutrino Detectability Using Machine Learning*, [2108.03125](#).
- [84] T. Chen and C. Guestrin, *Xgboost: A scalable tree boosting system*, *CoRR* **abs/1603.02754** (2016) , [[1603.02754](#)].
- [85] K. Fukushima, *Neocognitron: A self-organizing neural network model for a mechanism of pattern recognition unaffected by shift in position*, *Biological Cybernetics* **36** (1980) 193–202.
- [86] K. Fukushima, *Artificial vision by multi-layered neural networks: Neocognitron and its advances*, *Neural Networks* **37** (2013) 103–119.
- [87] Y. Lecun, L. Bottou, Y. Bengio and P. Haffner, *Gradient-based learning applied to document recognition*, *Proceedings of the IEEE* **86** (1998) 2278–2324.
- [88] B. Auerbach, S. Chekanov, J. Love, J. Proudfoot and A. V. Kotwal, *Sensitivity to new high-mass states decaying to $t\bar{t}$ at a 100 tev collider*, *Phys. Rev. D* **91** (Feb, 2015) 034014.
- [89] C. Helsens, D. Jamin, M. L. Mangano, T. G. Rizzo and M. Selvaggi, *Heavy resonances at energy-frontier hadron colliders*, *Eur. Phys. J. C* **79** (2019) 569, [[1902.11217](#)].
- [90] B. Bhattacharjee, N. Khan and A. Patra, *Anatomy of Heavy Gauge Bosons in a Left-Right Supersymmetric Model*, *Phys. Rev. D* **100** (2019) 075010, [[1811.11743](#)].
- [91] Z. Lu, J. Qin, H. Li, Z.-L. Han, F. Huang, C.-Y. Li et al., *Phenomenological study of heavy neutral gauge boson in the left-right symmetric model at future muon collider*, [2408.15471](#).
- [92] S. Bhattacharyya and A. Datta, *Phenomenology of an E6 inspired extension of the Standard Model: Higgs sector*, *Phys. Rev. D* **105** (2022) 075021, [[2109.08524](#)].
- [93] Q.-H. Cao and D.-M. Zhang, *Collider Phenomenology of the 3-3-1 Model*, [1611.09337](#).
- [94] L. Di Luzio, J. Fuentes-Martin, A. Greljo, M. Nardecchia and S. Renner, *Maximal Flavour Violation: a Cabibbo mechanism for leptiquarks*, *JHEP* **11** (2018) 081, [[1808.00942](#)].
- [95] N. Greiner, K. Kong, J.-C. Park, S. C. Park and J.-C. Winter, *Model-Independent Production of a Top-Philic Resonance at the LHC*, *JHEP* **04** (2015) 029, [[1410.6099](#)].
- [96] J. H. Kim, K. Kong, S. J. Lee and G. Mohlabeng, *Probing TeV scale Top-Philic Resonances with Boosted Top-Tagging at the High Luminosity LHC*, *Phys. Rev. D* **94** (2016) 035023, [[1604.07421](#)].
- [97] ATLAS collaboration, M. Aaboud et al., *Search for heavy particles decaying into top-quark pairs using lepton-plus-jets events in proton–proton collisions at $\sqrt{s} = 13$ TeV with the ATLAS detector*, *Eur. Phys. J. C* **78** (2018) 565, [[1804.10823](#)].
- [98] ATLAS collaboration, M. Aaboud et al., *Search for heavy particles decaying into a top-quark pair in the fully hadronic final state in pp collisions at $\sqrt{s} = 13$ TeV with the ATLAS detector*, *Phys. Rev. D* **99** (2019) 092004, [[1902.10077](#)].

- [99] ATLAS collaboration, G. Aad et al., *Search for $t\bar{t}$ resonances in fully hadronic final states in pp collisions at $\sqrt{s} = 13$ TeV with the ATLAS detector*, *JHEP* **10** (2020) 061, [[2005.05138](#)].
- [100] ATLAS collaboration, G. Aad et al., *Search for top-philic heavy resonances in pp collisions at $\sqrt{s} = 13$ TeV with the ATLAS detector*, *Eur. Phys. J. C* **84** (2024) 157, [[2304.01678](#)].
- [101] H. E. Haber and L. Stephenson Haskins, *Supersymmetric theory and models.*, in *Theoretical Advanced Study Institute in Elementary Particle Physics: Anticipating the Next Discoveries in Particle Physics*, pp. 355–499, WSP, 2018. [1712.05926](#). DOI.
- [102] R. K. Barman, B. Bhattacharjee, A. Choudhury, D. Chowdhury, J. Lahiri and S. Ray, *Current status of MSSM Higgs sector with LHC 13 TeV data*, *Eur. Phys. J. Plus* **134** (2019) 150, [[1608.02573](#)].
- [103] H. Bahl, S. Liebler and T. Stefaniak, *MSSM Higgs benchmark scenarios for Run 2 and beyond: the low $\tan\beta$ region*, *Eur. Phys. J. C* **79** (2019) 279, [[1901.05933](#)].
- [104] R. K. Barman, B. Bhattacharjee, I. Chakraborty, A. Choudhury and N. Khan, *Electroweakino searches at the HL-LHC in the baryon number violating MSSM*, *Phys. Rev. D* **103** (2021) 015003, [[2003.10920](#)].
- [105] A. Adhikary, R. K. Barman, B. Bhattacharjee, A. De, R. M. Godbole and S. Kulkarni, *Long-lived NLSP in the NMSSM*, *Phys. Rev. D* **108** (2023) 035020, [[2207.00600](#)].
- [106] R. K. Barman, G. Belanger, B. Bhattacharjee, R. Godbole, G. Mendiratta and D. Sengupta, *Invisible decay of the Higgs boson in the context of a thermal and nonthermal relic in MSSM*, *Phys. Rev. D* **95** (2017) 095018, [[1703.03838](#)].
- [107] S. P. Martin, *A Supersymmetry primer*, *Adv. Ser. Direct. High Energy Phys.* **18** (1998) 1–98, [[hep-ph/9709356](#)].
- [108] S. Bhattacharyya, *Heavy Higgs boson searches at the LHC in light of a left-right symmetric model*, *Phys. Rev. D* **109** (2024) 015034, [[2307.04169](#)].
- [109] T. Appelquist, H.-C. Cheng and B. A. Dobrescu, *Bounds on universal extra dimensions*, *Phys. Rev. D* **64** (2001) 035002, [[hep-ph/0012100](#)].
- [110] H.-C. Cheng, *Introduction to Extra Dimensions*, in *Theoretical Advanced Study Institute in Elementary Particle Physics: Physics of the Large and the Small*, pp. 125–162, 2011. [1003.1162](#). DOI.
- [111] Q. Shafi, *E_6 as a unifying gauge symmetry*, *Physics Letters B* **79** (1978) 301–303.
- [112] T. Fukuyama, *$SO(10)$ GUT in Four and Five Dimensions: A Review*, *Int. J. Mod. Phys. A* **28** (2013) 1330008, [[1212.3407](#)].
- [113] V. Keus, S. F. King and S. Moretti, *Three-Higgs-doublet models: symmetries, potentials and Higgs boson masses*, *JHEP* **01** (2014) 052, [[1310.8253](#)].
- [114] I. P. Ivanov, *Building and testing models with extended Higgs sectors*, *Prog. Part. Nucl. Phys.* **95** (2017) 160–208, [[1702.03776](#)].

- [115] J. Shao, I. P. Ivanov and M. Korhonen, *Symmetries for the 4HDM: II. Extensions by rephasing groups*, *J. Phys. A* **57** (2024) 385401, [[2404.10349](#)].
- [116] M. P. Bento, J. C. Romão and J. a. P. Silva, *Unitarity bounds for all symmetry-constrained 3HDMs*, *JHEP* **08** (2022) 273, [[2204.13130](#)].
- [117] R. Boto, J. C. Romão and J. a. P. Silva, *Current bounds on the type-Z Z3 three-Higgs-doublet model*, *Phys. Rev. D* **104** (2021) 095006, [[2106.11977](#)].
- [118] S. Carrolo, J. C. Romão, J. a. P. Silva and F. Vazão, *Symmetry and decoupling in multi-Higgs boson models*, *Phys. Rev. D* **103** (2021) 075026, [[2102.11303](#)].
- [119] H. Georgi and M. Machacek, *Doubly charged higgs bosons*, *Nuclear Physics B* **262** (1985) 463–477.
- [120] M. S. Chanowitz and M. Golden, *Higgs boson triplets with $M_w = M_z \cos\theta_w$* , *Physics Letters B* **165** (1985) 105–108.
- [121] H. E. Logan and M. B. Reimer, *Characterizing a benchmark scenario for heavy Higgs boson searches in the Georgi-Machacek model*, *Phys. Rev. D* **96** (2017) 095029, [[1709.01883](#)].
- [122] G. Bélanger, J. Dutta, R. M. Godbole, S. Kraml, M. Mitra, R. Padhan et al., *Revisiting the decoupling limit of the Georgi-Machacek model with a scalar singlet*, *JHEP* **10** (2024) 058, [[2405.18332](#)].
- [123] Z. Baire and A. Ahriche, *More constraints on the Georgi-Machacek model*, *Phys. Rev. D* **108** (2023) 055028, [[2207.00142](#)].
- [124] D. Chowdhury, P. Mondal and S. Samanta, *Next-to-Leading Order Unitarity Fits in the Extended Georgi-Machacek Model*, [[2404.18996](#)].
- [125] A. Kundu, P. Mondal and P. B. Pal, *Custodial symmetry, the Georgi-Machacek model, and other scalar extensions*, *Phys. Rev. D* **105** (2022) 115026, [[2111.14195](#)].
- [126] CMS collaboration, A. M. Sirunyan et al., *Search for a heavy Higgs boson decaying to a pair of W bosons in proton-proton collisions at $\sqrt{s} = 13$ TeV*, *JHEP* **03** (2020) 034, [[1912.01594](#)].
- [127] CMS collaboration, A. Tumasyan et al., *Search for a heavy Higgs boson decaying into two lighter Higgs bosons in the $\tau\tau bb$ final state at 13 TeV*, *JHEP* **11** (2021) 057, [[2106.10361](#)].
- [128] CMS collaboration, A. Tumasyan et al., *Search for a massive scalar resonance decaying to a light scalar and a Higgs boson in the four b quarks final state with boosted topology*, *Phys. Lett. B* **842** (2023) 137392, [[2204.12413](#)].
- [129] CMS collaboration, A. M. Sirunyan et al., *Search for charged Higgs bosons decaying into a top and a bottom quark in the all-jet final state of pp collisions at $\sqrt{s} = 13$ TeV*, *JHEP* **07** (2020) 126, [[2001.07763](#)].
- [130] CMS collaboration, A. Tumasyan et al., *Search for a charged Higgs boson decaying into a heavy neutral Higgs boson and a W boson in proton-proton collisions at $\sqrt{s} = 13$ TeV*, *JHEP* **09** (2023) 032, [[2207.01046](#)].

- [131] ATLAS collaboration, G. Aad et al., *Search for heavy neutral Higgs bosons decaying into a top quark pair in 140 fb^{-1} of proton-proton collision data at $\sqrt{s} = 13 \text{ TeV}$ with the ATLAS detector*, *JHEP* **08** (2024) 013, [[2404.18986](#)].
- [132] ATLAS collaboration, G. Aad et al., *Search for the decay of the Higgs boson to a Z boson and a light pseudoscalar particle decaying to two photons*, *Phys. Lett. B* **850** (2024) 138536, [[2312.01942](#)].
- [133] ATLAS collaboration, G. Aad et al., *Search for heavy Higgs bosons with flavour-violating couplings in multi-lepton plus b-jets final states in pp collisions at 13 TeV with the ATLAS detector*, *JHEP* **12** (2023) 081, [[2307.14759](#)].
- [134] ATLAS collaboration, G. Aad et al., *Search for charged Higgs bosons decaying into a top quark and a bottom quark at $\sqrt{s} = 13 \text{ TeV}$ with the ATLAS detector*, *JHEP* **06** (2021) 145, [[2102.10076](#)].
- [135] ATLAS collaboration, G. Aad et al., *Search for a heavy charged Higgs boson decaying into a W boson and a Higgs boson in final states with leptons and b-jets in $\sqrt{s} = 13 \text{ TeV}$ pp collisions with the ATLAS detector*, [2411.03969](#).
- [136] J. a. M. Alves, G. C. Branco, A. L. Cherchiglia, C. C. Nishi, J. T. Penedo, P. M. F. Pereira et al., *Vector-like singlet quarks: A roadmap*, *Phys. Rept.* **1057** (2024) 1–69, [[2304.10561](#)].
- [137] Y.-J. Zhang, Y.-T. Zhu, L. Han, Y.-P. Bi and T.-G. Liu, *Searching for the vector-like X-quark at the future electron-proton colliders*, *Eur. Phys. J. C* **84** (2024) 1184.
- [138] Y.-B. Liu, B. Hu and C.-Z. Li, *Single production of vectorlike quarks with charge 5/3 at the 14 TeV LHC*, *Nucl. Phys. B* **1007** (2024) 116667, [[2402.01248](#)].
- [139] R. Benbrik et al., *Signatures of vector-like top partners decaying into new neutral scalar or pseudoscalar bosons*, *JHEP* **05** (2020) 028, [[1907.05929](#)].
- [140] A. Azatov, D. Chowdhury, D. Ghosh and T. S. Ray, *Same sign di-lepton candles of the composite gluons*, *JHEP* **08** (2015) 140, [[1505.01506](#)].
- [141] A. Banerjee, V. Ellajosyula and L. Panizzi, *Heavy vector-like quarks decaying to exotic scalars: a case study with triplets*, *JHEP* **01** (2024) 187, [[2311.17877](#)].
- [142] A. Banerjee, E. Bergeaas Kuutmann, V. Ellajosyula, R. Enberg, G. Ferretti and L. Panizzi, *Vector-like quarks: status and new directions at the LHC*, [2406.09193](#).
- [143] A. Banerjee et al., *Phenomenological aspects of composite Higgs scenarios: exotic scalars and vector-like quarks*, [2203.07270](#).
- [144] CMS collaboration, A. Hayrapetyan et al., *Review of searches for vector-like quarks, vector-like leptons, and heavy neutral leptons in proton-proton collisions at $\sqrt{s} = 13 \text{ TeV}$ at the CMS experiment*, [2405.17605](#).
- [145] ATLAS COLLABORATION collaboration, *Search for singly produced vectorlike top partners in multilepton final states with 139 fb^{-1} of pp collision data at $\sqrt{s} = 13 \text{ TeV}$ with the atlas detector*, *Phys. Rev. D* **109** (Jun, 2024) 112012.

- [146] ATLAS COLLABORATION collaboration, *Search for single production of a vectorlike t quark decaying into a higgs boson and top quark with fully hadronic final states using the atlas detector*, *Phys. Rev. D* **105** (May, 2022) 092012.
- [147] *Search for pair-production of vector-like quarks in pp collision events at $s=13$ tev with at least one leptonically decaying z boson and a third-generation quark with the atlas detector*, *Physics Letters B* **843** (2023) 138019.
- [148] ATLAS COLLABORATION collaboration, *Search for singly produced vectorlike top partners in multilepton final states with 139 fb^{-1} of pp collision data at $\sqrt{s} = 13 \text{ TeV}$ with the atlas detector*, *Phys. Rev. D* **109** (Jun, 2024) 112012.
- [149] CMS collaboration, A. Tumasyan et al., *Search for single production of a vector-like T quark decaying to a top quark and a Z boson in the final state with jets and missing transverse momentum at $\sqrt{s} = 13 \text{ TeV}$* , *JHEP* **05** (2022) 093, [2201.02227].
- [150] CMS collaboration, A. Tumasyan et al., *Search for a W' boson decaying to a vector-like quark and a top or bottom quark in the all-jets final state at $\sqrt{s} = 13 \text{ TeV}$* , *JHEP* **09** (2022) 088, [2202.12988].
- [151] CMS collaboration, A. Tumasyan et al., *Search for pair production of vector-like quarks in leptonic final states in proton-proton collisions at $\sqrt{s} = 13 \text{ TeV}$* , *JHEP* **07** (2023) 020, [2209.07327].
- [152] CMS collaboration, A. Tumasyan et al., *Search for a vector-like quark $T' \rightarrow tH$ via the diphoton decay mode of the Higgs boson in proton-proton collisions at $\sqrt{s} = 13 \text{ TeV}$* , *JHEP* **09** (2023) 057, [2302.12802].
- [153] M. Buchkremer, G. Cacciapaglia, A. Deandrea and L. Panizzi, *Model Independent Framework for Searches of Top Partners*, *Nucl. Phys. B* **876** (2013) 376–417, [1305.4172].
- [154] J.-Z. Han, J. Yang, S. Xu and H.-K. Wang, *Search for single production of vector-like b quark via bz channel at the hl -lhc*, *Nuclear Physics B* **975** (2022) 115672.
- [155] B. Yang, Z. Li, X. Jia, S. Moretti and L. Shang, *Search for single vector-like B quark production in hadronic final states at the LHC*, *Eur. Phys. J. C* **84** (2024) 1124, [2405.13452].
- [156] CMS collaboration, A. M. Sirunyan et al., *Search for single production of vector-like quarks decaying to a top quark and a W boson in proton-proton collisions at $\sqrt{s} = 13 \text{ TeV}$* , *Eur. Phys. J. C* **79** (2019) 90, [1809.08597].
- [157] ATLAS collaboration, G. Aad et al., *Optimisation of large-radius jet reconstruction for the ATLAS detector in 13 TeV proton–proton collisions*, *Eur. Phys. J. C* **81** (2021) 334, [2009.04986].
- [158] ATLAS collaboration, G. Aad et al., *Search for single production of a vectorlike T quark decaying into a Higgs boson and top quark with fully hadronic final states using the ATLAS detector*, *Phys. Rev. D* **105** (2022) 092012, [2201.07045].
- [159] ATLAS collaboration, G. Aad et al., *Search for pair-production of vector-like quarks in pp collision events at $s=13 \text{ TeV}$ with at least one leptonically decaying Z boson and a*

- third-generation quark with the ATLAS detector, *Phys. Lett. B* **843** (2023) 138019, [2210.15413].
- [160] ATLAS collaboration, G. Aad et al., *Search for singly produced vectorlike top partners in multilepton final states with 139 fb⁻¹ of pp collision data at s=13 TeV with the ATLAS detector*, *Phys. Rev. D* **109** (2024) 112012, [2307.07584].
- [161] ATLAS collaboration, G. Aad et al., *Search for new particles in final states with a boosted top quark and missing transverse momentum in proton-proton collisions at $\sqrt{s} = 13$ TeV with the ATLAS detector*, *JHEP* **05** (2024) 263, [2402.16561].
- [162] Mathieu Buchkremer, Giacomo Cacciapaglia, Aldo Deandrea, Luca Panizzi, “VLQ Model.” http://feynrules.irmp.ucl.ac.be/wiki/VLQ_bsingletv1, 2014.
- [163] J. Alwall, M. Herquet, F. Maltoni, O. Mattelaer and T. Stelzer, *MadGraph 5 : Going Beyond*, *JHEP* **06** (2011) 128, [1106.0522].
- [164] T. Sjostrand, S. Mrenna and P. Z. Skands, *A Brief Introduction to PYTHIA 8.1*, *Comput. Phys. Commun.* **178** (2008) 852–867, [0710.3820].
- [165] NNPDF collaboration, R. D. Ball et al., *Parton distributions for the LHC Run II*, *JHEP* **04** (2015) 040, [1410.8849].
- [166] DELPHES 3 collaboration, J. de Favereau, C. Delaere, P. Demin, A. Giammanco, V. Lemaître, A. Mertens et al., *DELPHES 3, A modular framework for fast simulation of a generic collider experiment*, *JHEP* **02** (2014) 057, [1307.6346].
- [167] M. Selvaggi, *A Delphes parameterisation of the FCC-hh detector*, tech. rep., CERN, Geneva, 2020.
- [168] M. Cacciari and G. P. Salam, *Dispelling the N³ myth for the k_t jet-finder*, *Phys. Lett. B* **641** (2006) 57–61, [hep-ph/0512210].
- [169] M. Cacciari, G. P. Salam and G. Soyez, *FastJet User Manual*, *Eur. Phys. J. C* **72** (2012) 1896, [1111.6097].
- [170] S. Ellis, J. Huston, K. Hatakeyama, P. Loch and M. Tönnesmann, *Jets in hadron-hadron collisions*, *Progress in Particle and Nuclear Physics* **60** (Apr., 2008) 484–551.
- [171] G. P. Salam, *Towards jetography*, *The European Physical Journal C* **67** (May, 2010) 637–686.
- [172] A. J. Larkoski, F. Maltoni and M. Selvaggi, *Tracking down hyper-boosted top quarks*, *JHEP* **06** (2015) 032, [1503.03347].
- [173] B. Mukhopadhyaya, T. Samui and R. K. Singh, *Dynamic radius jet clustering algorithm*, *JHEP* **04** (2023) 019, [2301.13074].
- [174] S. Jain, *Revisiting new and old jet clustering algorithms for beyond the standard model Higgs searches in the final states with b-jets*. PhD thesis, University of Southampton, Southampton U., Southampton U., 2023.
- [175] A. J. Larkoski, S. Marzani, G. Soyez and J. Thaler, *Soft Drop*, *JHEP* **05** (2014) 146, [1402.2657].

- [176] A. J. Larkoski and J. Thaler, *Aspects of jets at 100 TeV*, *Phys. Rev. D* **90** (2014) 034010, [[1406.7011](#)].
- [177] M. Arjovsky, S. Chintala and L. Bottou, *Wasserstein generative adversarial networks*, in *International conference on machine learning*, pp. 214–223, PMLR, 2017.
- [178] E. Perez Codina and P. G. Roloff, *Initial Study of the Reconstruction of Boosted B-hadrons and τ -leptons at FCC-hh*, tech. rep., CERN, Geneva, 2018.
- [179] E. Perez Codina and P. G. Roloff, *Hit multiplicity approach to b-tagging in FCC-hh*, tech. rep., CERN, Geneva, 2018.